MARINE PHYSICAL LABORATORY

SCRIPPS INSTITUTION OF OCEANOGRAPHY -

San Diego, California 92152

OBSERVATIONS OF SEAFLOOR AMBIENT NOISE WITH AN OCEAN BOTTOM SEISMOMETER ARRAY

ADA 220159

by / **Anthony Edward Schreiner**

SIO REFERENCE 89-27

MPL-U-84/89
December 1989

Approved for public release; distribution unlimited.

REPORT DOCUMENTATION PAGE

Form Approved
OMB No. 0704-0188

1a. REPORT SECURITY CLASSIFICATION	1b. RESTRICTIVE MARKINGS
UNCLASSIFIED	

2a. SECURITY CLASSIFICATION AUTHORITY	3. DISTRIBUTION / AVAILABILITY OF REPORT
2b. DECLASSIFICATION / DOWNGRADING SCHEDULE	Approved for public release; distribution unlimited.

4. PERFORMING ORGANIZATION REPORT NUMBER(S)	5. MONITORING ORGANIZATION REPORT NUMBER(S)
SIO Reference 89-27 [MPL-U-84/89]	

6a. NAME OF PERFORMING ORGANIZATION	6b. OFFICE SYMBOL (If applicable)	7a. NAME OF MONITORING ORGANIZATION
University of California, San Diego	MPL	Office of Naval Research Department of the Navy

6c. ADDRESS (City, State, and ZIP Code)	7b. ADDRESS (City, State, and ZIP Code)
Marine Physical Laboratory Scripps Institution of Oceanography San Diego, California 92152	800 North Quincy Street Arlington, VA 22217-5000

8a. NAME OF FUNDING / SPONSORING ORGANIZATION	8b. OFFICE SYMBOL (If applicable)	9. PROCUREMENT INSTRUMENT IDENTIFICATION NUMBER
Office of Naval Research	ONR	N00014-87-K-0010

8c. ADDRESS (City, State, and ZIP Code)	10. SOURCE OF FUNDING NUMBERS			
	PROGRAM ELEMENT NO.	PROJECT NO.	TASK NO.	WORK UNIT ACCESSION NO.
800 North Quincy Street Arlington, VA 22217-5000				

11. TITLE (Include Security Classification)
OBSERVATIONS OF SEAFLOOR AMBIENT NOISE WITH AN OCEAN BOTTOM SEISMOMETER ARRAY

12. PERSONAL AUTHOR(S)
Anthony Edward Schreiner

13a. TYPE OF REPORT	13b. TIME COVERED	14. DATE OF REPORT (Year, Month, Day)	15. PAGE COUNT
summary	FROM _____ TO _____	December 1989	138

16. SUPPLEMENTARY NOTATION

17.	COSATI CODES		18. SUBJECT TERMS (Continue on reverse if necessary and identify by block number)
FIELD	GROUP	SUB-GROUP	ocean bottom seismometers, ambient noise, arrays

19. ABSTRACT (Continue on reverse if necessary and identify by block number)

In 1987 an array of ocean bottom seismometers (OBS) was deployed in the deep ocean off southern California for the purpose of recording ocean bottom ambient noise. By lowering the instruments with a wire, it was possible for the first time to create an array which allowed coherent processing of short wavelength energy in the frequency range 0.05 to 30 Hz.

The array consisted of 9 working instruments in place for 30 days, allowing for the recording of ambient noise during several changes in the surface environment. Sea surface conditions were determined from the U.S. Navy's Global Spectral Ocean Wave Model (GSOWM). Noise levels at the ocean floor have been correlated with the swell height and wind speed predicted by the GSOWM. However, the theoretical transfer function between surface wave height and pressure fluctuations on the bottom did not predict the recorded pressure signal to a high degree of accuracy.

The array achieved a uniform sampling of distances between sensors, and a good estimate of spatial coherence has been made up to 156 m. A characteristic pattern of coherence length dependence on frequency is observed throughout the deployment. Spatial coherence is related to the wavelength and beam width of the energy from a partially coherent source. Through modeling of seismic energy it has been possible to estimate the range to the source of the noise energy. The coherence field is consistent with a wave field propagating horizontally through the sedimentary layer from a source at the edge of the sedimentary basin, suggesting that the conversion of acoustic energy in the water to seismic energy in the ocean floor occurs at the rough boundary at the edge of the sedimentary basin.

The wavenumber decomposition or beamforming of the ambient noise presented some difficulties. Higher mode and thus faster seismic waves were predominant, and therefore the array did not have a sufficiently large aperture. Nevertheless, the results of beamforming are consistent with the results of the modeling of the spatial coherence.

20. DISTRIBUTION / AVAILABILITY OF ABSTRACT	21. ABSTRACT SECURITY CLASSIFICATION
☐ UNCLASSIFIED/UNLIMITED ■ SAME AS RPT. ☐ DTIC USERS	UNCLASSIFIED

22a. NAME OF RESPONSIBLE INDIVIDUAL	22b. TELEPHONE (Include Area Code)	22c. OFFICE SYMBOL
Leroy M. Dorman, Professor of Geophysics	(619) 534-2406	MPL

DD Form 1473, JUN 86   Previous editions are obsolete.   SECURITY CLASSIFICATION OF THIS PAGE

OBSERVATIONS OF SEAFLOOR AMBIENT NOISE WITH AN OCEAN BOTTOM SEISMOMETER ARRAY

Anthony Edward Schreiner

SIO REFERENCE 89-27

Approved for public release; distribution unlimited.

UNIVERSITY OF CALIFORNIA

SAN DIEGO

Observations of seafloor ambient noise with

an ocean bottom seismometer array

A dissertation submitted in partial satisfaction of the

requirements for the degree Doctor of Philosophy

in Earth Sciences

by

Anthony Edward Schreiner

Committee in charge:

Professor LeRoy M. Dorman, Chair
Professor Charles S. Cox
Professor John A. Hildebrand
Professor Walter H. Munk
Professor Murray Rosenblatt

1989

Table of Contents

List of Tables and Figures

Chapter II

Chapter III

Chapter IV

Chapter V

Chapter VI

Acknowledgements

I have many people to thank for their contributions to this work. The principal investigators, LeRoy Dorman and John Hildebrand are, of course due credit for bringing this experiment to reality and for making it a success. I thank them especially for the opportunity to work with them and their guidance.

The successful deployment of the sensor array was ensured by several other people. Fred Spiess and the Deep Tow group consisting of Tony Bogeman, Vince Pavlicek, Bob Elder, Bob Lawhead, and Gary Austin were of vital importance. Special thanks also to fellow students and shipmates, Phil Hammer, Dalia Lahav, and Mark Stevenson, and also to Tony Aja, David Willoughby, and Allan Sauter. The cooperation of Dale Bibee and Bill Everard of NORDA is also appreciated.

The data analysis phase was assisted by programs kindly provided by Guy Masters and Alan Chave.

Most important to me was the contribution of Gesa Kirsch throughout the duration of this project. If this dissertation is readable, it largely due to her suggestions. But beyond that, her companionship, even at a distance of 2000 miles (3200 kilometers), was the key to surviving this difficult time as the project came to fruition.

This work was supported by the Office of Naval Research.

ABSTRACT OF THE DISSERTATION

Observations of seafloor ambient noise with

an ocean bottom seismometer array

by

Anthony Edward Schreiner

Doctor of Philosophy in Earth Sciences

University of California, San Diego, 1989

Professor LeRoy M. Dorman, Chair

In 1987 an array of ocean bottom seismometers (OBS) was deployed in the deep ocean off southern California for the purpose of recording ocean bottom ambient noise. By lowering the instruments with a wire, it was possible for the first time to create an array which allowed coherent processing of short wavelength energy in the frequency range 0.05 to 30 Hz.

The array consisted of 9 working instruments in place for 30 days, allowing for the recording of ambient noise during several changes in the surface environment. Sea surface conditions were determined from the U.S. Navy's Global Spectral Ocean Wave Model (GSOWM). Noise levels at the ocean floor have been correlated with the swell height and wind speed predicted by the GSOWM. However, the theoretical transfer function between surface wave height and pressure fluctuations on the bottom did not predict the recorded pressure signal to a high degree of accuracy.

The array achieved a uniform sampling of distances between sensors, and a good estimate of spatial coherence has been made up to 156 m. A characteristic pattern of coherence length dependence on frequency is observed throughout the deployment. Spatial coherence is related to the wavelength and beam width of the energy from a partially coherent source. Through modeling of seismic energy it has been possible to estimate the range to the source of

the noise energy. The coherence field is consistent with a wave field propagating horizontally through the sedimentary layer from a source at the edge of the sedimentary basin, suggesting that the conversion of acoustic energy in the water to seismic energy in the ocean floor occurs at the rough boundary at the edge of the sedimentary basin.

The wavenumber decomposition or beamforming of the ambient noise presented some difficulties. Higher mode and thus faster seismic waves were predominant, and therefore the array did not have a sufficiently large aperture. Nevertheless, the results of beamforming are consistent with the results of the modeling of the spatial coherence.

CHAPTER 1

HISTORICAL INTRODUCTION

Measurement of seismic energy is limited at low levels by ambient noise. The seismic noise level varies with frequency and is strongest in the measurement band between 1 and 10 seconds period. Energy in this band is known as microseisms and has a long history of study. It was noted near the turn of the century that a strong background signal existed below 1 Hz [*Wiechert*, 1904]. Over forty years ago it was realized that the signal was related to storm activity [*Deacon*, 1947]. There are a large number of references on the subject (*Iyer* [1964] provides a good, though by now outdated, reference list), mostly consisting of qualitative observations.

Miche [1944] evaluated the hydrodynamical equations governing standing waves to second order and identified a pressure term which did not have an explicit depth dependence. *Longuet-Higgins* [1950] recognized this pressure fluctuation as a possible source of the microseisms. Further development by *Hasselman* [1963] led to the theory of microseisms in its presently accepted form. When sets of ocean swell interact with each other, there is quadratic pressure term which can propagate to the deep ocean floor. The effect is strongest for components traveling in nearly opposite directions. Their interaction generates an acoustic signal which propagates to the ocean floor and excites seismic waves if the wavenumber is equal to that of a resonant mode in the solid ocean floor. The nonlinear interaction generates an excitation whose frequency is double that of the ocean swell.

Haubrich et al. [1963] gave quantitative observational support for the 2:1 ratio between the frequency of the microseism peak and the ocean swell at a nearby site. Using a three-component seismometer they were able to estimate the direction of the source. They concluded that reflection of storm swell off the local coast line was resulting in oppositely directed propagating waves which in turn generated seismic energy.

In the 1960's, treaties limiting the testing of nuclear weapons relied in part on seismic measurements as a means of monitoring compliance. This spurred the development of the World Wide Standardized Seismic Network (WWSSN) and an effort to increase the sensitivity of seismic detection. Project VELA Uniform was sponsored by the Defense Advanced Research Projects Agency (DARPA) and combined seismic and space based methods. One of the important methodologies was to use sensor arrays to enhance coherent over incoherent signals. The most ambitious array was the Large Aperture Seismic Array (LASA) in Montana which covered an area 200 km on a side with 525 seismic stations.

Another useful capability of seismometer arrays is that the propagation velocity and source direction of seismic energy can be measured directly. *Haubrich and McCamy* [1969] used LASA to determine the direction and distance of the seismic energy source at the microseism frequency. With the array they were able to distinguish surface wave modes and body waves. They demonstrated that the fundamental Rayleigh mode and the body waves are generated at the coast and in the vicinity of storms at sea.

During this same time period, the first deployments of seismographs on the ocean floor were taking place. Columbia University deployed an ocean bottom seismometer (OBS) for short periods in the Atlantic in 1964 and then continuously between 1966 and 1972 at the base of the continental slope of Cape Mendocino, California. It had been expected that the ocean environment would be quieter than land sites. *Schneider et al.* [1964] discovered that there was no improvement in signal to noise ratio for ocean bottom seismometers, signal and noise are both enhanced on the ocean floor. Noise levels at frequencies between 0.1 and 1 Hz are greater at ocean bottom sites than on land. *Latham and Sutton* [1966] concluded that results were consistent with the hypothesis that low frequency noise propagates as a Rayleigh wave in the oceanic crust. There were two consequences from these results. First, there was little effort in the following decade at making teleseismic measurements from oceanic stations. Second, OBS technological advancement emphasized measurement at frequencies above the microseism

band.

There have been more measurements of ambient noise in shallow water environments than in deep water, both for reasons of expense and of direct application to the military. There is strong evidence that in shallow seas various forms of ambient noise propagate as interface waves along the bottom [*Rauch*, 1980; *Kibblewhite and Ewans*, 1986] In sufficiently shallow water, the pressure fluctuation due to the passage of surface wave can excite the bottom directly.

Experiments based on OBS's in deep water have now become fairly routine. Recent improvements in sensors have made possible the measurement of increasingly lower frequencies. *Webb et al.* [1986] have made pressure measurements down to 0.005 Hz. Their data show clearly what some call the "noise notch" between 0.02 and 0.1 Hz. This frequency band of low noise level has created a new interest in making teleseismic measurements on the ocean floor and has spurred further research into the study of deep ocean ambient noise.

Measurement of microseisms on land have suggested that they propagate largely as low order surface waves. Low order modes have the property that their amplitudes decay away from the surface to which they are bound. In contrast, body waves of interest for global seismology have no such dependence. *Sax and Hartenberger* [1964, 1965] have demonstrated that increases in signal to noise ratio (SNR) can be made by placing the sensor at depth in a borehole.

To test the analogy for the oceanic environment, two different ocean borehole seismic systems were commissioned: the Marine Seismic System (MSS) [*Adair et al.*, 1986, 1987] and the Ocean Sub-bottom Seismometer (OSS) [*Duennebier et al.*, 1987]. These have each been deployed successfully on two occasions contemporaneously with OBS. There have been three important observations regarding microseisms from these deployments. First, overall signal levels are lower in the borehole than on the ocean floor. This is because the ocean floor is typically covered with sediments of low rigidity. Conservation of energy requires that seismic amplitudes increase when propagating through a low rigidity medium [*Duennebier et al.*, 1987],

in contrast to the borehole seismometers which were clamped to crystalline basement. Second, after making the aforementioned amplitude correction, the amplitude of the microseism peak near 0.16 Hz is similar for ocean bottom and ocean sub-bottom locations. This suggested to *Adair et al.* [1987] that at these frequencies, oceanic noise is predominantly crustal Rayleigh waves with little contribution from Stoneley waves which are trapped near the water-sediment interface. Third, at higher frequencies, the noise level is considerably higher at the ocean floor, especially on the horizontal components. *Duennebier et al.* [1987] interpreted the higher levels as trapped energy in the sedimentary wave guide.

Very recently, there have been significant improvements in seismic recording systems. The WWSSN instruments were analog and therefore had limited dynamic range. As a consequence they were configured as separate sensors for the long period and short period bands on either side of the microseism peak. Modern digital systems are capable of recording from 0.001 to 10 Hz with greatly increased dynamic range with a single sensor. There is an effort to enhance the WWSSN with other networks using these new instruments. Hardware improvements notwithstanding, the global seismic network is still largely limited by that fact that seismic stations are on land. The majority of the Earth's surface which is covered by ocean remains unsampled and therefore global models are biased. There is an initiative to find ocean sites for these broad band instruments [*Purdy and Dziewonski*, 1988]. However the state of understanding of ocean floor ambient noise is still limited. Specifically, there is little agreement whether the noise propagates in the ocean crust as Rayleigh waves over large distances or Stoneley/Scholte waves over short distances. This question has an important bearing on how sensors should be placed at oceanic sites. If short wavelength Stoneley waves predominate, emplacement of the sensors in a borehole below the skin depth of the interface waves would result in a significant signal to noise ratio improvement. Oceanic Rayleigh waves on the other hand have wavelengths on the order of kilometers, and it is not practical to put a sensor far enough away from the boundary to have a useful effect.

One of the reasons that there is still much room for progress in the subject of ocean ambient seismic noise is that to date, most measurements have been made with individual sensors or multiple sensors with inexact locations. On land, important progress was made when seismic array data were examined. Arrays of sensors allowing coherent processing of signals have until recently been impossible because of operational difficulties. Such an array deployment was undertaken in 1987 and the following chapters describe the operation of the array and some results from the data analysis.

Chapter 2 describes the ocean bottom seismometer array and the new technology that made its deployment possible. Wire deployments of the instrument packages made possible the deployment of the sensors with unprecedented precision. This in turn permitted an extremely tight array which enabled coherent processing of the recorded signals in the frequency band of 0.1 to 10 Hz.

In chapter 3, the tools of analysis — the frequency and wavenumber spectra — are described. The methods by which these are computed may introduce bias into the results. Two alternative methods were used for both the frequency and the wavenumber spectra.

The subsequent chapters report on the analysis of the data. Chapter 4 focuses on measurements made by the individual instruments while chapters 5 and 6 discusses the results from the array as a whole. In chapter 4, I relate changes in ambient noise level with time to changes in the surface conditions such as local wind speed, local swell height and distant swell height. I draw some conclusions about how each of these factors affect the noise level at the array site.

In chapter 5, I present the analysis of the spatial coherence measurements. The variation of coherence with frequency and sensor separation places constraints on the mode of propagation of the seismic energy. The sedimentary wave guide will be seen to have a dominant effect on the seismic noise field.

Chapter 6 describes the results from wavenumber analysis of the array data. Direct estimates of the seismic velocity of the ambient noise, through the wavenumber spectrum, have a large scatter but give a picture of the mode structure which is consistent with that observed through the coherence model.

CHAPTER 2
EXPERIMENT DETAILS

INTRODUCTION

Deployment of the OBS array took place in April and May of 1987. The array was situated near Deep Sea Drilling Project (DSDP) Hole 469 at a depth of 3.8 km (Figure 2.1). The area is a 400 m thick sedimentary basin with minimal topography in the immediate vicinity [*Yeats, Haq et al.*, 1981].

Groups from Scripps Institution of Oceanography (SIO) and the Naval Ocean Research and Development Activity (NORDA) participated in the experiment which was code-named "CIRCUS". A total of thirteen OBS were available: six from SIO, six from NORDA, and an additional one from Oregon State University through NORDA. The instruments were deployed from the *R/V Melville* in the period of April 10 through April 22. They remained on the bottom for a month and were recovered on two separate trips with the *M/V Jamie G* and the *R/V Sproull.*

At two times during the array deployment, mid-water "Swallow" floats were deployed from the *USNS Narragansett* for periods of 24 hours in a related experiment. One of the aims of this experiment was to characterize the difference in noise level between the ocean bottom and at several depths in the water column [*D'Spain and Hodgkiss*, 1988].

OBS ARRAY DESIGN

The OBS array was designed to enable wavenumber decomposition of the ambient noise field in the spatial frequency range of extremely slowly traveling interface waves. The array therefore had a small aperture of 150 m and a wavenumber Nyquist frequency of $50\,\text{km}^{-1}$. The wavenumber resolution of an array depends on the aperture, or greatest separation between sensors. The Nyquist frequency in contrast, depends on the minimum spacing between sensors.

7

These two conflicting criteria must be satisfied with a limited number of sensors.

A convenient way of analyzing array performance is through the co-array. This is the autocorrelation of array element positions and is the set of points generated by all the vector offsets between each pair of sensor positions in the array [*Haubrich*, 1968]. The frequency response of an array is given by

$$R(\mathbf{k}) = \sum_{i,j=1}^{N} e^{2\pi i (\mathbf{k} \cdot \mathbf{x}_i - \mathbf{k} \cdot \mathbf{x}_j)}. \qquad 3.1$$

When rewritten in terms of the co-array, this takes the form

$$R(\mathbf{k}) = 1 + \sum_{m=1}^{M} \cos(2\pi \mathbf{k} \cdot \mathbf{x}_m). \qquad 3.2$$

The sum is over all the nonzero co-array points.

An important class of arrays are those with a uniform co-array. Since the separation between sensors is constant in this case, the response may be written (for a linear array)

$$R(k) = 1 + \sum_{m=1}^{M} \cos(2\pi k m \Delta x) \qquad 3.3$$

which takes the form of a Fourier series. A given function can be approximated better by a greater number of terms in a Fourier series, so it is desirable to maximize the number of points in the co-array. It is not necessary to have a uniform array to generate a uniform co-array, and in fact, equivalent co-arrays can be generated with fewer sensors with unequal spacing. Figure 2.2 shows a simple example for a linear array [*LaCoss et al.*, 1968].

The maximum possible number of co-array points given N sensors, is $M = N(N-1)$. This maximum is achieved for a minimally redundant array, one in which none of the vector offsets are duplicated. The cost of using a minimally redundant array is that the stability of the wavenumber spectral estimate is reduced [*LaCoss et al.*, 1969]. It is possible, however, to make up for the lost stability by increasing the stability of temporal spectral estimate used in generating the wavenumber estimate. Figure 2.3 shows the minimum redundancy design for the array used in the CIRCUS experiment along with its co-array.

ARRAY DEPLOYMENT

A compact array was desired because of the high wavenumber of the signals under observation. Small arrays are also advantageous because the inhomogeneity of the medium is reduced. The deployment of such a compact array represented a significant technical effort. The small dimension of the array required a placement accuracy of 1 to 2 meters. Such an accuracy in position can not be achieved by the conventional method of deploying the instruments by free-fall through nearly 4 km of water. The solution was to use technology from the "Deep Tow" system of the Marine Physical Laboratory (MPL) at Scripps, a system which combines wire-lowered-vehicles and transponder guidance [*Spiess and Lonsdale* 1982].

The deployment of the CIRCUS array made use of two newly developed tow vehicles, the "Thruster" and the "Rock-scan" sonar. The Thruster has a propulsion system which permits partial maneuverability independent of the ship. The CIRCUS expedition was one of the first field tests of this vehicle. Because of several breakdowns, we were not able to use it for every OBS deployment. The backup vehicle, Rock-scan sonar provided no propulsion system but included upward- and downward-looking sonar and a transponder.

A release hook was developed which could be opened on command from the ship lab. The OBS capsules were attached via this hook to a 25 m length of rope suspended from the tow fish. Figure 2.4 depicts the elements of the system (not to scale). The rope served as a shock absorber during the lowering of the OBS and the tow vehicle into the water. The OBS were most conveniently put in the water with the side crane while the tow fish was deployed and lowered through the stern A-frame. Once the tow fish was in the water with the OBS hanging beneath it the system could be lowered at a speed of 30 meters per minute. In 3800 m of water the trip to the bottom took about 3 hours.

The feature that makes the Deep Tow system an effective tool for the emplacement of instruments on the bottom is the creation of a fixed reference system with an array of acoustic transponders. Acoustic pings are exchanged between either the ship or the tow fish and the

transponders which are moored to the ocean bottom. The transponders are interrogated at three frequencies: 10, 10.5 and 11 kHz and reply at single frequency of 12 kHz. The round trip acoustic travel times are displayed on a chart recorder in the ship lab. Three fixed transponders were used for the present experiment. The desired sensor positions were marked on the chart as a distance from each of the transponders. The hook was released when the proper combination of distances was achieved.

Figure 2.5 shows the geometry of the whole system with all distances drawn to scale. Note that the size of the array is on the order of the length of the ship, and that the ship and the array are separated from each other by 50 times that length. For the tow fish without propulsion capability the position of the bottom of the wire can only be controlled by positioning the ship. The *R/V Melville* is propelled by cycloids and can be maneuvered very precisely in any direction. However, the connection to the package at the end of the wire is flexible so maneuvers at the surface take 20 minutes to propagate down to the bottom. Given enough time and several passes, good positioning could be achieved. Typically it required 2 to 3 hours of maneuvering in addition to the 6 hours round trip from the surface. With the Thruster unit, the bottom time was reduced to under an hour.

The tow fish, transponder and ship positions were recalculated using an iterative least squares method [*Lowenstein*, 1969]. One source of error which has not been estimated is the amount of lateral drift by the OBS capsule after its release from the hook. They were typically allowed to fall freely for the last 50 m to ensure that the sensor package would not be dragged along the bottom.

SENSOR PACKAGE

The 12 SIO and NORDA seismographs are of the same design with only minor differences. The OBS design has been in use at Scripps since 1981 [*Moore et al.*, 1981]. Their operation is controlled by a microprocessor for maximum flexibility of the recording parameters.

The sensors are a triaxial arrangement of seismometers and a pressure sensor. The seismometers are Mark Products model L-4C-3D with a resonant frequency of 1 Hz. Two different types of pressure transducers were used, an Ocean and Atmospheric Systems model E-2DP crystal hydrophone and a differential pressure sensor of a design by *Cox et al.* [1984]. The differential hydrophone has much better performance at frequencies below 1 Hz. They were used on 5 of the OBS in this experiment.

The sensor output is fed through a variable gain preamp with a 54 dB range. The amplification level is determined by a long term average of the ambient noise independently for each channel. This site turned out to be remarkably quiet, and the gain was usually at its maximum setting. The signal is further conditioned by a pre-whitening filter and anti-alias filters with a cut-off frequency of 30 Hz. Figure 2.6 shows the transfer function for the seismometer channels and figure 2.7 for the two kinds of hydrophones.

A 12-bit A/D operating at 128 samples per second converts the signal to digital form. The data are buffered and written to the tape recorder after the end of the recording window so that the mechanical movement of the tape recorder does not affect the signal. The buffer memory has a capacity of 128 kbyte, or 227 seconds for four channels at 128 Hz. There is a capacity for event triggering that was disabled for this experiment to avoid using up recording capacity. The data are written to tape on four serial tracks with 8 additional words after every 64 for time keeping and error detection. The normal recorders have a capacity of 5 Mbyte per channel of data or roughly 6 hours of continuous data. Five of the capsules were deployed with a data recorder with a storage capacity of 20 Mbyte per channel.

DATA QUALITY

The deployed positions of the sensors are compared to the desired positions in Figure 2.3. The realized positions were within 5 m of the planned positions with two exceptions. The OSU instrument was of a different configuration and did not fit onto the hook. It was deployed by free-fall and was sited just to the west of the array center. The outlying instrument was also

deployed by free-fall. An impending shooting schedule did not leave enough time for a wire deployment. As it turned out, having a sensor at the larger distance proved quite useful.

Of the 13 instruments deployed, 9 returned usable data. These are marked by the filled triangles. Of the remaining, one capsule failed to resurface. and the three others suffered tape recorder problems. One of the four failed instruments was the OSU instrument and three were SIO/NORDA instruments which were set up with the experimental high capacity data recorders. Furthermore, of the remaining 3 Cox-Webb sensors, the preamps on 2 of them were incorrectly biased and yielded poor quality pressure data.

The actual co-array for the functioning sensors (Figure 2.8) is somewhat irregular compared to the desired co-array, but mildly so. The wavenumber response (Figure 2.9) has higher side lobe energy than the ideal one and a skewed central peak. The position of the outlying OBS 1 was not included in the calculation of these displays. Incorporating that one would have the effect extending the co-array to the NE and SW and would narrow the central peak of the response in that same direction.

It is reasonable to ask whether we might have have done as well with a random array deployed inexpensively from the sea surface. The extreme small size of the array means that a fluctuation in the ship position of one ship length would result in an sensor position as far away as OBS 1. A random array of this sort would almost certainly have a much lower aliasing frequency and would not be capable of resolving Stoneley wave velocities.. The large effort required to deploy instruments precisely was worthwhile.

Figure 2.10 shows the data coverage for the good instruments. The suffix (L) after the OBS name indicates the use of a low frequency Cox-Webb hydrophone. OBS 5 and 6 were also fitted with high capacity recorders and failed early. We suspect that the recorders placed a high power burden on the system.

The 4-track OBS FM tapes are read by a computer in the lab and stored on 9-track digital tape. Some of the records could not be processed because of synchronization errors on

the tape. Of the functioning instruments 81% of the records are actually available for analysis. All in all, about 51% of the possible data was actually recovered. Though one could hope for a better proportion, this leaves a substantial data set of 144 records recorded by up to 9 instruments on 4 components.

Aside from the quality of the individual time series, array analysis requires precise relative timing control. The clock on each of the OBS operates independently and is subject to drift. The one month deployment was a relatively long one for these instruments so the timing problem was serious. The clock error at recovery can be measured against a reference time, and a linear interpolation of the correction can be made for all recording times. This was done and found to be inadequate. The data set was scanned for transients appearing on all or most of the instruments and a time correction was made to align them. Linear interpolation of the time correction between these infrequent occurrences of transients was more satisfactory. To use a source in the medium for this purpose requires an assumption about the propagation velocity of the signal. These waveforms did not appear to be dispersed so we assumed that these signals traveled at the velocity of sound in water and thus traversed the 150 m extent of the array in 0.1 s. Lacking knowledge of the source direction we assumed that the propagation across the array was instantaneous. This is acceptable if the array is to resolve velocities well below 1500 m s^{-1}.
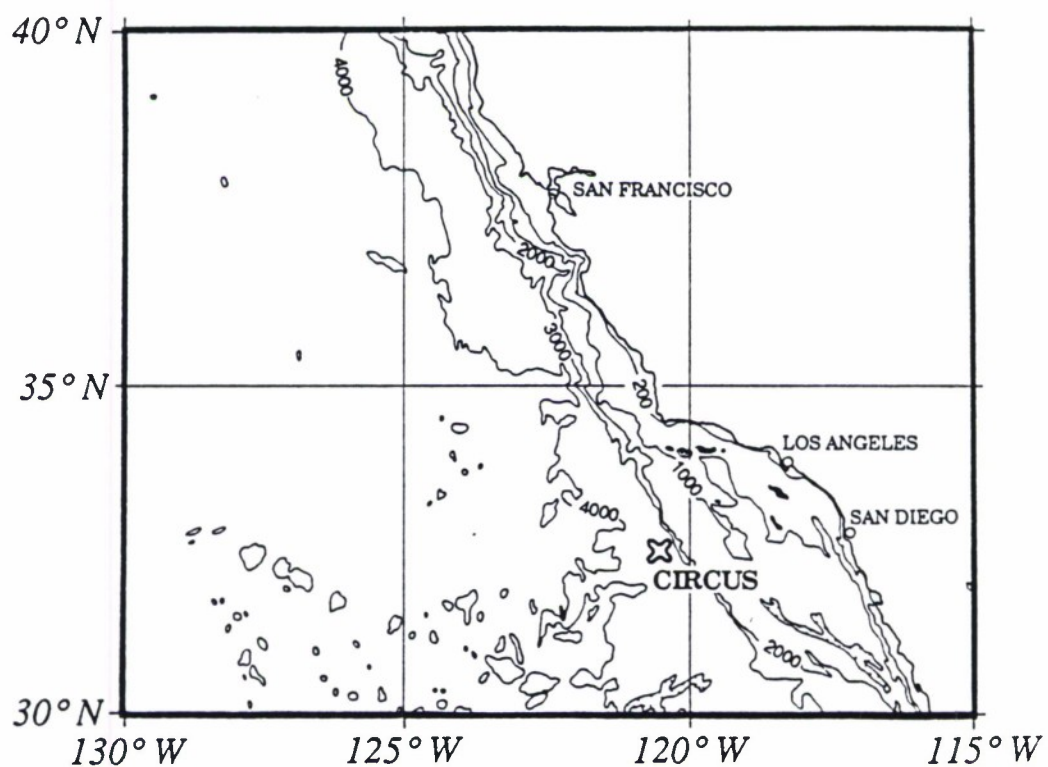
Figure 2.1. Map of the CIRCUS array site. The array position is 32° 37' N, 120° 34' W at a depth of 3800 m. The isobath units are meters.

15

Redundant Linear Array

Sensor Positions   +   +   +   +   +   +   +

```
                              +
                           +  +  +
Repetitions             +  +  +  +  +
                     +  +  +  +  +  +  +
                  +  +  +  +  +  +  +  +  +
               +  +  +  +  +  +  +  +  +  +  +
            +  +  +  +  +  +  +  +  +  +  +  +  +
Lag        -6 -5 -4 -3 -2 -1  0  1  2  3  4  5  6
```

Nonredundant Linear Array

Sensor Positions   +   +   + ,   +

Repetitions

```
                              +
                              +
                              +
            +  +  +  +  +  +  +  +  +  +  +  +  +
Lag        -6 -5 -4 -3 -2 -1  0  1  2  3  4  5  6
```
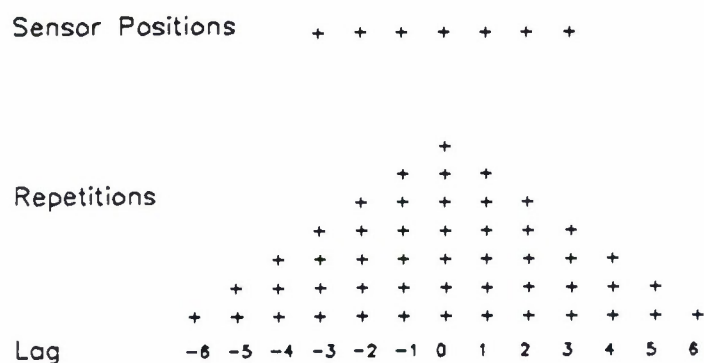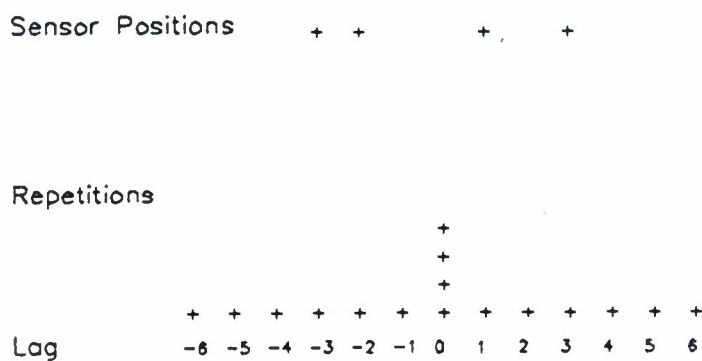
Figure 2.2. Comparison of co-arrays for redundant and nonredundant linear array designs. Even though fewer sensors are used in the nonredundant design, the same lag space coverage is achieved. However the redundant design provides repeated lags.
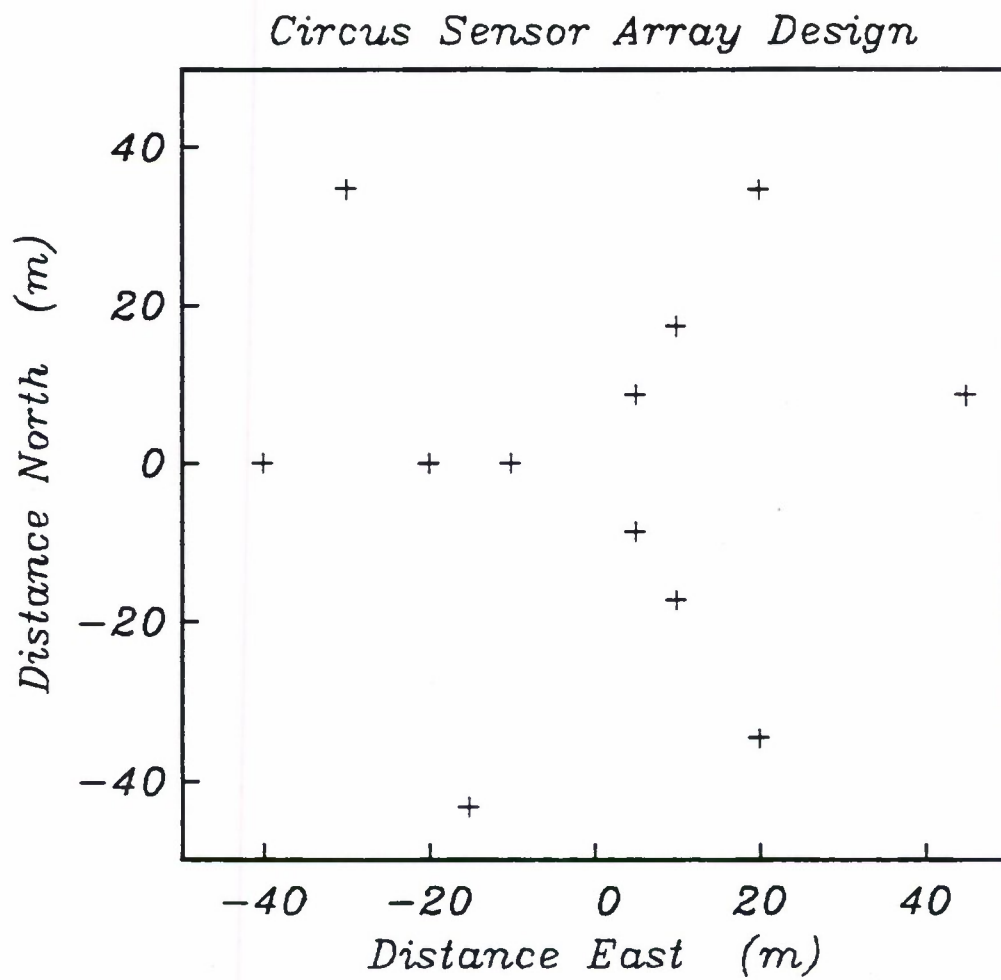
Figure 2.3. Minimally redundant design of the CIRCUS array with 12 sensors.
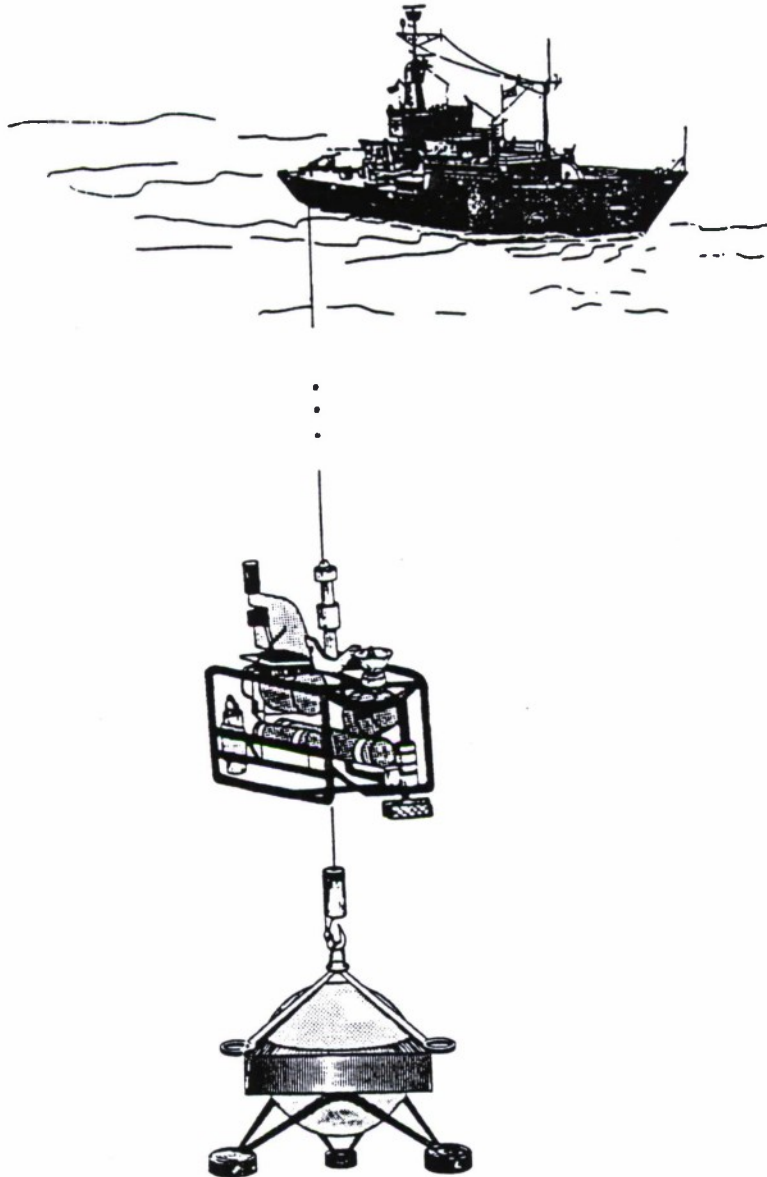
Figure 2.4. Elements of the deployment system (not to scale). The ocean bottom seismometer capsule is attached to an electrically operated release hook and suspended beneath the "Thruster" tow fish. The Thruster is lowered from the ship with 0.680" wire.

Deployment
Geometry
(water depth = 3.8 km)
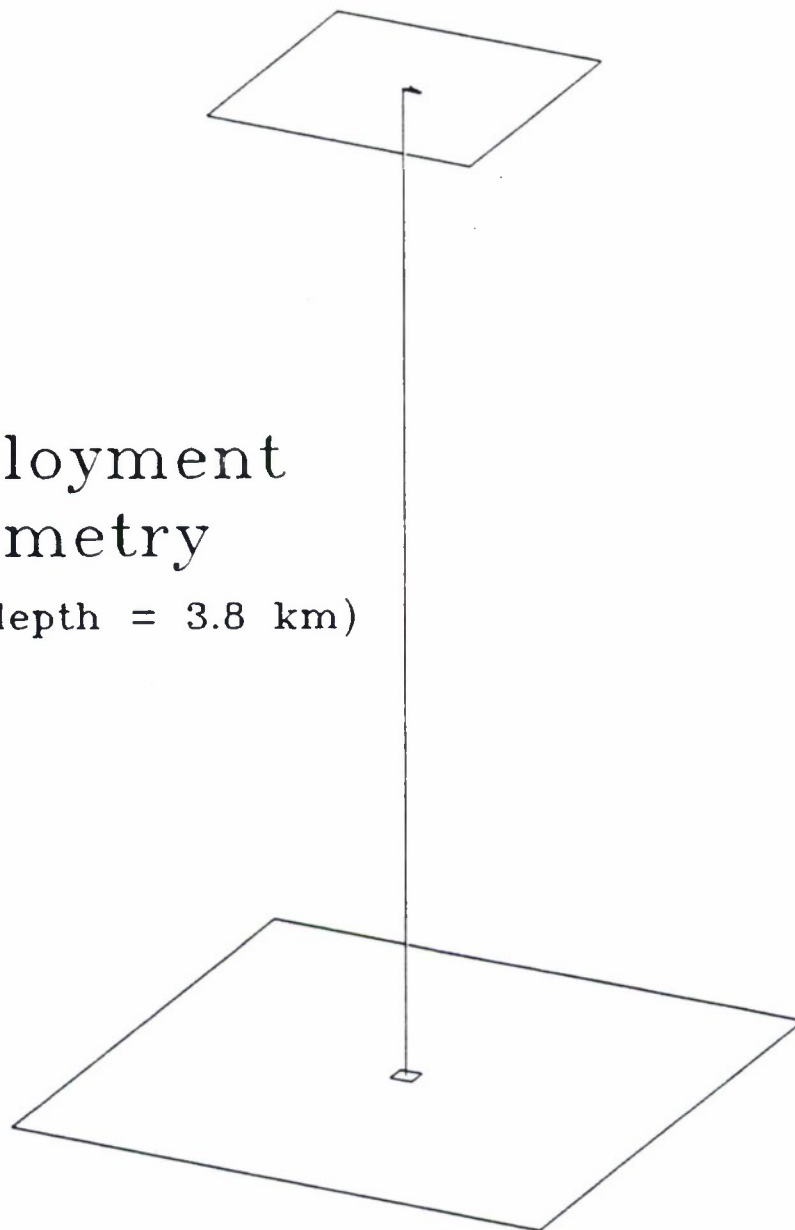
Figure 2.5. Deployment geometry to scale. The surface ship is 70 m in length, the array has an aperture of 80 m. The array is at a distance of 3800 m below the ship.

Seismometer Channel Response
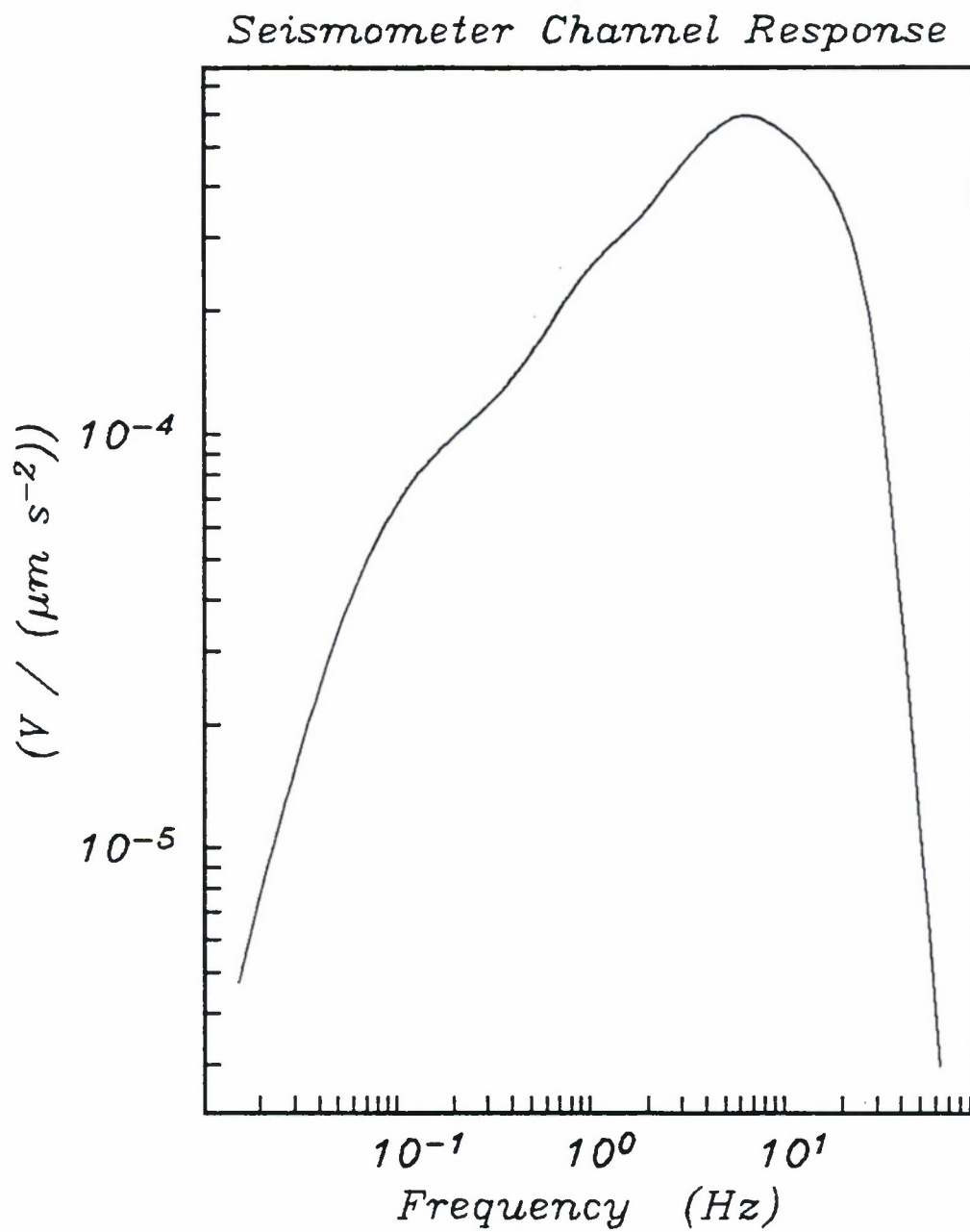
Figure 2.6. Response of the seismometer channel to ground acceleration. An anti-aliasing filter cuts of the energy above 30 Hz.
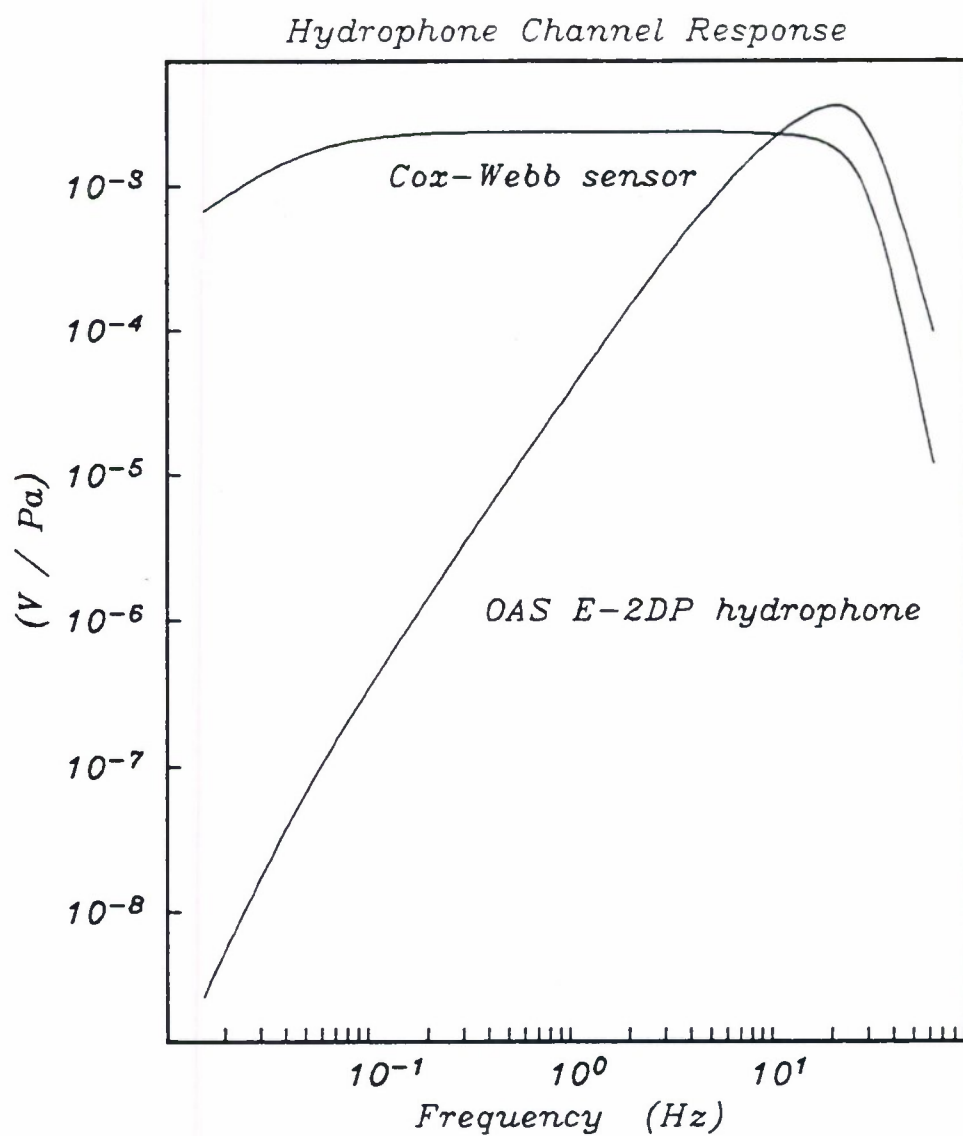
Figure 2.7. Response of the hydrophone channel to pressure for both the commercial crystal hydrophone and the Cox-Webb differential pressure sensor.
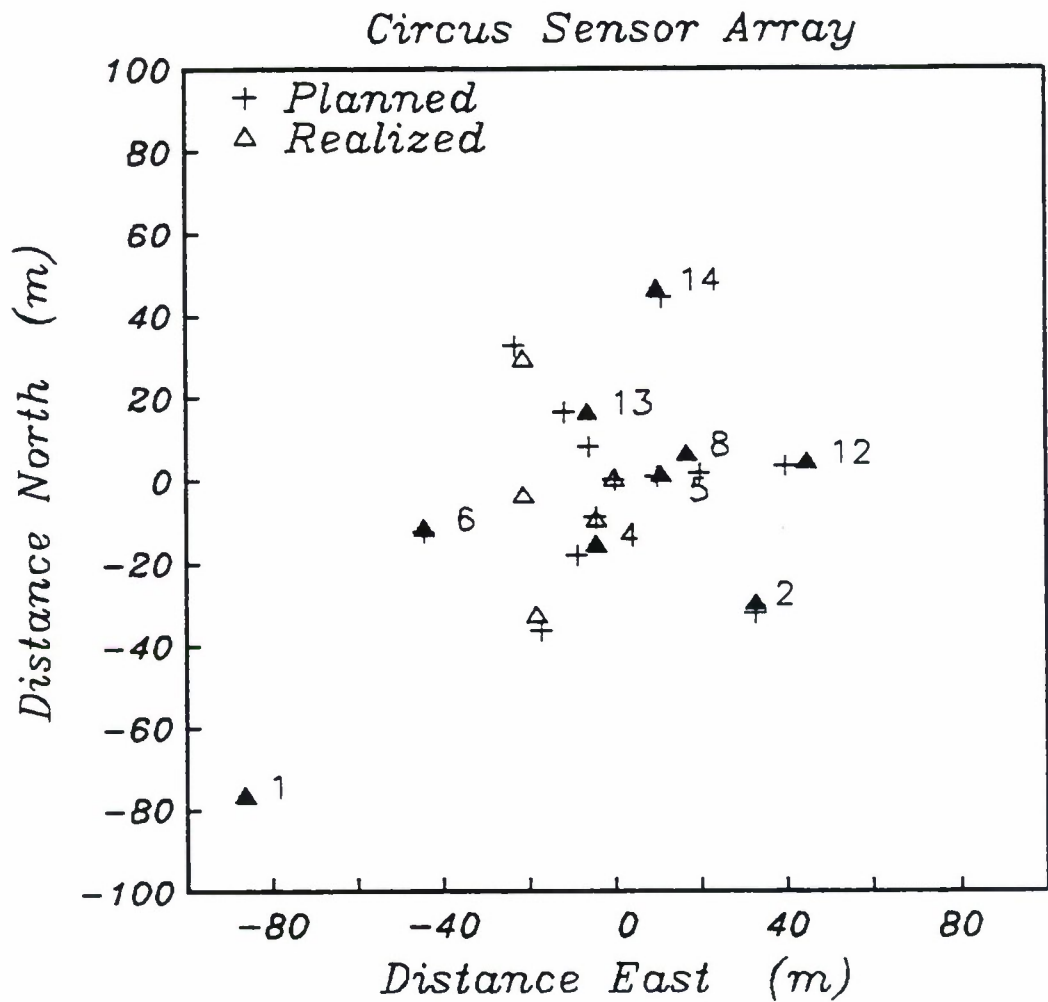
Figure 2.8. Actual array configuration. The crosses indicate the 12 element design and the triangles indicate the estimated positions of the OBS capsules. In most cases, the realized position was within 3 m of the target. In two cases the realized position does not correspond to any target position. The filled triangles indicate the OBS's that returned data.
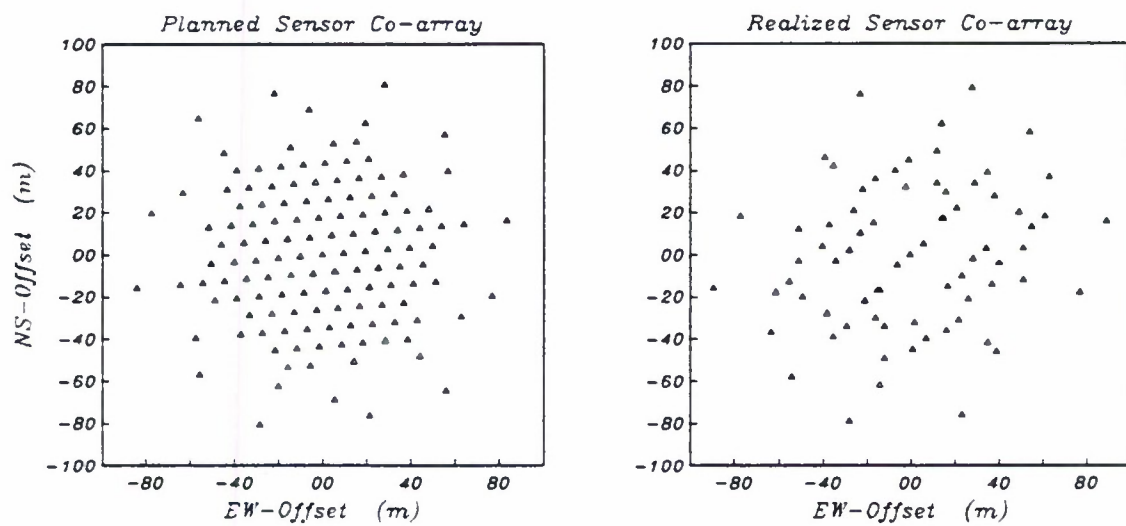
Figure 2.9. Comparison of the co-array pattern for the designed array and the actual array. The extent of the actual array is about the same as planned, but the distribution of co-array lags is more uneven.

23
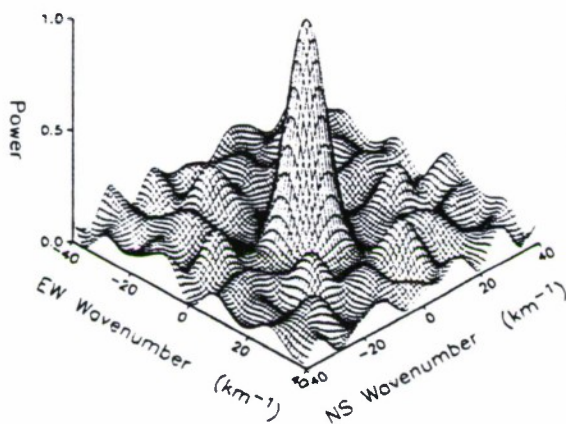
Planned Array Response   Realized Array Response
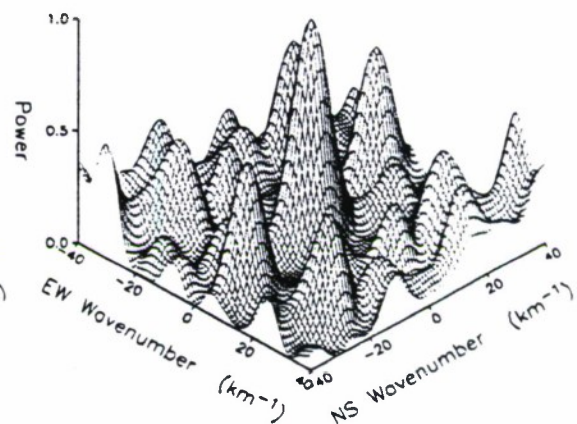
Figure 2.10. Wavenumber response for the planned array with 12 elements and the actual array with 9 working sensors. The planned array response has sidelobes of 0.2 times the peak power. The realized array has sidelobes of up to 0.5 times the peak power.
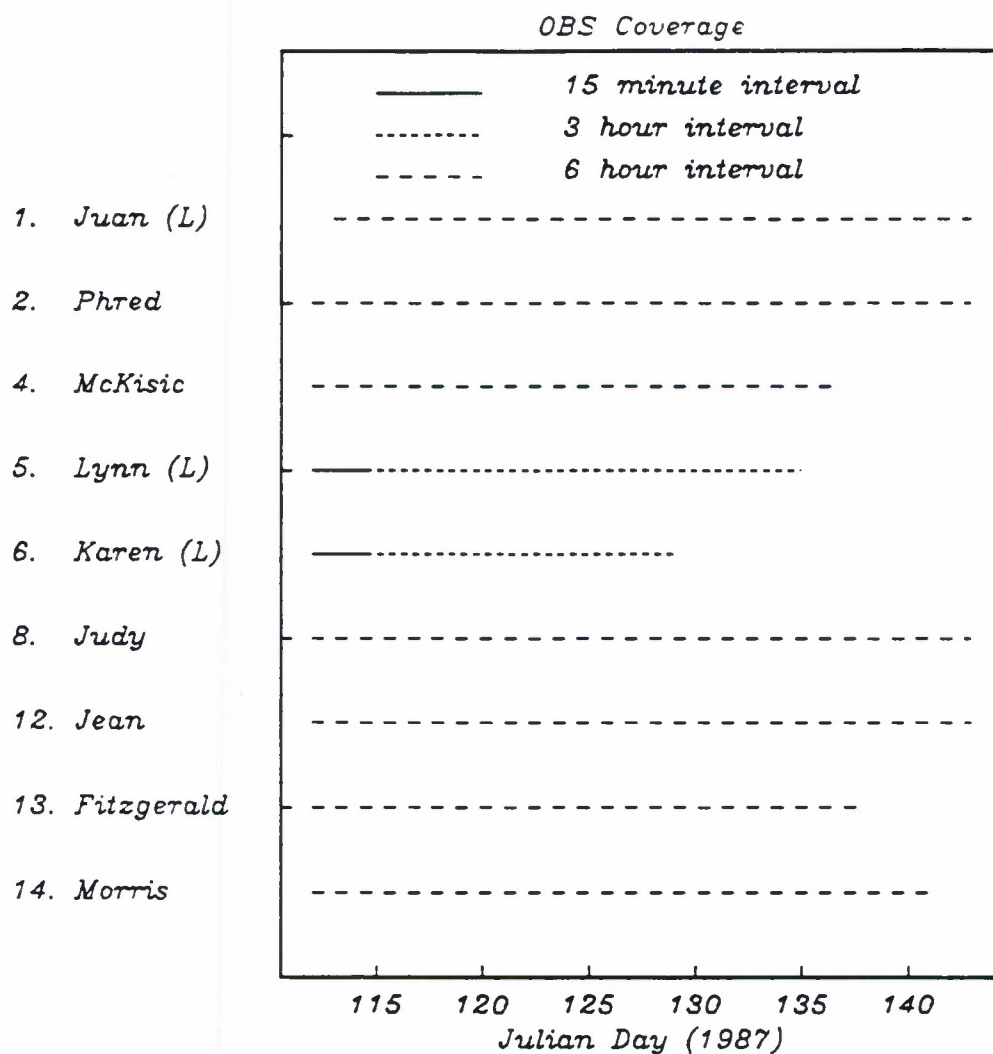
Figure 2.11. Data coverage in time. All instruments were scheduled to begin recording at day 112 00:00 (CUT). OBS 1 was put in place 24 hours late. OBS 5 and OBS 6 recorded at 15 minute intervals until day 114 06:00 then reverted to a 3 hour recording interval. All the other instruments recorded at 6 hour intervals. The capsule names marked with (L) were configured with the long period pressure sensors.

CHAPTER 3

DATA ANALYSIS METHODS

The CIRCUS array deployment collected a large volume of time series data. Ambient noise is essentially a random process; *Haubrich* [1965] showed that microseisms are stationary over a period of hours and approximately normally distributed. The present data have not been tested explicitly for these properties, but they are assumed to have similar statistical behavior. Second order statistical parameters such as spectra are appropriate for data of this type. The fundamental tools for examining the data collected in this study are the auto-spectrum and the cross-spectrum.

POWER SPECTRA

The spectral power density, being a statistical quantity of a random variable, requires an expectation

$$P(f) = E[|y(f)|^2] \tag{3.1}$$

where $y(f)$ is the Fourier transform of the data. The expectation operation is usually performed by some kind of averaging, of which a variety of methods have been developed. The different methods vary in their effectiveness and the type of data for which they are suitable. In this study, spectra have been computed with two methods: the segment-averaged Fourier transform [*Welch*, 1967] and the multiple window Fourier transform [*Thomson*, 1982]. The algorithms are well known, particularly for the first method. They will be described here to emphasize the difference in results that may be achieved using either one.

In the first method, the time series is divided into many (20 or more) segments which may or may not partially overlap. Each segment is tapered with a suitable function (e.g. a Kaiser-Bessel window) to reduce bias, and then a fast Fourier transform (FFT) is performed on the segment. The transformed segments are then averaged together to yield the spectral esti-

25

mate. If the time series x is sampled at intervals of ΔT, then let $x_n = x(n\Delta T)$. The segment averaged estimate of the power spectrum is

$$P(f) = \frac{1}{N}\sum_{n=1}^{N} y_n(f)y_n^*(f),\qquad(3.2)$$

where the time series is divided into N segments and y_n is the weighted Fourier transform of the n-th segment

$$y_n(f) = y_n(k/M\Delta T) = \frac{1}{M\Delta T}\sum_{m=0}^{M-1} w_m x_{m+L(n-1)}e^{-2\pi ikm/M},\qquad(3.3)$$

where M is the length of the segment, L is the increment between each segment, w is the window function, and the superscript '*' denotes complex conjugation. The averaging of segments is done to make the estimate consistent and to reduce the variance. There are two drawbacks to the method: one is that the resolution possible by performing the Fourier transform on segments of length M is much poorer than would be possible by transforming the original series of length $(N-1)L+M$. The other is that averaging increases the bias of the estimate. The segment averaging method is most effective when the time series is long enough so that even when split into segments, the resolution is acceptable. The bandwidth of the estimate is proportional to the reciprocal of the section length T. The total length of the series is $[(N-1)L/M+1]T$. The quantity $(1/T)\cdot[(N-1)L/M+1]T = (N-1)L/M+1$ may be called the time bandwidth product, and reduces to N when $L=M$. The time bandwidth product is a measure of the trade-off between the desired frequency resolution and the amount of averaging required for a stable estimate. Confidence intervals may be assigned to the spectral estimate by assuming that the data are normally distributed. The error distribution is then given by a χ_ν^2 variable with $\nu=2N$ degrees of freedom where N is the number of segments used. Figure 3.1 shows some examples of the trade-off of variance and resolution for some spectra computed from the CIRCUS data.

The multiple window method (also referred to as the multiple taper method) is to be preferred when the time series is not long enough to be divided into enough segments. The method is considerably more complicated and expensive of computing resources. It is based on the observation by *Slepian and Pollack* [1961] and *Slepian*, [1978] that for a given bandwidth

$(-W,W)$, of all possible time limited functions of unit energy, the prolate spheroidal wavefunctions minimize the energy outside the frequency bandwidth. The discrete prolate spheroidal wavefunctions (DPSW) are a natural consequence of mapping a continuous stationary process onto a finite sample using the Dirichlet kernel, $K_D(f_0,f) = \dfrac{\sin N\pi(f_0-f)}{\sin\pi(f_0-f)}$. The DPSW, $U_k(N,W;f_0)$ are solutions of the eigenvalue problem

$$\int_{-W}^{W} K_D(f_0,f) U_k(N,W;f_0) = \lambda_k(N,W) U_k(N,W;f_0). \tag{3.4}$$

The eigenvalues λ_k are real, distinct, and limited between 0 and 1. The first $2NW$ eigenvalues are nearly equal to 1 and then they decay towards 0. The Fourier transforms of the DPSW are called the discrete prolate spheroidal sequences (DPSS) and are computed from a discrete eigenvalue problem analogous to Equation (3.4). *Slepian* [1978] showed that the estimate using the zero-order DPSS, v_0

$$y_k(f_0) = A\sum_{n=0}^{N} v_{0_n} x_n e^{-2\pi i f_0 n} \tag{3.5}$$

is the spectral estimate with the minimum spectral leakage for any choice of window.

Thomson's [1982] contribution was to average together estimates using several low order sequences. The first step is to select a frequency bandwidth $(-W,W)$ or equivalently a time bandwidth NW, where N is the length of the data sequence. The time bandwidth NW controls variance and the resolution of the spectral estimate and also the number of prolate spheroidal sequences that will be used to compute the estimate. The data are multiplied with each DPSS in turn and then Fourier transformed yielding K eigenspectra, y_k. The spectral estimate is given by an average of the eigenspectra. An unweighted average is not suitable because the higher order sequences have poorer bias properties. Instead, a weighted average is used

$$S(f) = \frac{A}{K} \frac{\sum_{k=0}^{K-1} \lambda_k d_k^2 |y_k(f)|^2}{\sum_{k=0}^{K-1} d_k^2(f)}, \tag{3.6}$$

where the weight coefficients are

.

$$d_k(f) = \frac{\sqrt{\lambda_k} S(f)}{\lambda_k S(f) + B_k(f)} \tag{3.7}$$

and are computed adaptively from the data by an iterative solution of

$$\sum_{k=0}^{K-1} \frac{\lambda_k (\hat{S}_k(f) - \lambda_k \frac{A}{K} \hat{S}_k(f))}{\lambda_k \hat{S}_k(f) - B_k(f))^2} = 0, \tag{3.8}$$

where $\hat{S}_k$ is the current solution of the iteration, B_k is an estimate of the broad band bias, and A is a constant used to normalize for the case of white noise. This algorithm is a modification of *Thomson*'s [1982] by *Chave* [1988]; the latter's notation is used here. The equivalent degrees of freedom may be given by

$$v(f) = 2 \sum_{k=0}^{K-1} \lambda_k d_k^2(f) \tag{3.9}$$

which yields a maximum of $2K$ in the absence of broad band bias. *Thomson* [1982] also noted that this formulation is equally suitable for line spectra as well as for continous spectra. A regression estimate for the amplitude of a line component is

$$\mu(f) = \frac{\sum_{k=0}^{K-1} U_k(N,W;0) y_k(f)}{\sum_{k=0}^{K-1} U_k^2(N,W;0)}. \tag{3.10}$$

An F-test may be performed on this value to determine if a line is significant. This feature will be used briefly in this study in the observation of ship signals.

The uncertainty in the estimate can be determined by a jack-knife procedure [*Efron*, 1982]. The spectral estimate is recomputed with each successive sequence omitted in turn. The difference between the various estimates is accumulated and then converted into a 95% significance bound. The resolution and the variance of the estimates are dependent on the bandwidth chosen. Figure 3.2 shows estimates of the noise spectrum made by the multiple window method for time bandwidths of 2, 4, and 6. Subsequent analyses have used a time bandwidth of 4, which constitutes a compromise between stability, resolution, and computational effort.

By comparing Figures 3.1 and 3.2, it can be seen if high resolution is not critical, the segment averaging method can yield better variance. In this study, when low frequencies are of interest, the multiple window method will be used, but when stability of the estimate is desired, as in beamforming, the segment averaging method with a high time bandwidth product will be used.

The cross-spectrum between two time series

$$S_{ij}(f) = E[y^{(i)}(f)y^{(j)*}(f)], \tag{3.11}$$

can be computed directly from their individual spectra, whether by the segment-averaged method or the multiple window method. The segment averaged method requires accumulating the conjugate product of the Fourier transforms for the two series

$$S_{ij}(f) = \frac{1}{N}\sum_{n=1}^{N} y_n^{(i)}(f)y_n^{(j)*}(f), \tag{3.12}$$

The cross-spectrum must be computed individually for each segment and then averaged, rather than in the reverse order. Otherwise, the number of independent quantities is reduced to one (c.f. *Claerbout*, 1976). For the multiple window method, the cross-spectra are computed from the weights and eigenspectra determined from the individual series

$$S_{ij}(f) = \sum_{k=0}^{K} e_k^{(i)}(f)e_k^{(j)}(f)y_k^{(i)*}(f)y_k^{(j)}(f) \tag{3.13}$$

where,

$$e_k^{(m)} = d_k^{(m)} / \sum_{j=1}^{K} d_j^{(m)2}.$$

Complex cross-spectra are usefully represented in polar form: magnitude and phase. The normalized magnitude is the coherence, which is the correlation coefficient at each frequency between two samples from and any jointly stationary processes [*Priestley*, 1981]. It indicates the degree to which the processes are linearly independent. The cross-phase is a measure of the propagation delay of a signal measured at two sites.

Uncertainty estimates can be made for the coherence. For the segment-averaged method, the error involves a complicated combination of hypergeometric functions [*Priestley*,

1981]. Often the statistic is reduced to a threshold determining whether the coherence estimate is significantly different from zero, in which case the threshold $T \approx 3/N$, where N is the number of degrees of freedom in the estimate. For the multiple window method, it is again possible to form a jack-knife estimate of the error by making estimates of the cross-spectra from different combinations of the eigenspectra.

For the general multi-channel case, the spectral matrix is given by

$$S(f) = E[y(f)y^H(f)] \tag{3.14}$$

where the elements of the complex vector y are the spectral estimates at frequency f for each channel, and the superscript H means conjugate transpose of the complex vector. For the segment averaging method, it takes the form

$$S(f) = \frac{1}{N} \sum_{i=1}^{N} y_i(f) y_i^H(f), \tag{3.15}$$

where y_i is a vector of the transform of the i-th windowed data segment. For the multiple window method,

$$S(f) = \frac{1}{K} \sum_{k=1}^{K} E_k(f) y_k(f) y_k^H(f) E_k(f), \tag{3.16}$$

where E_k is a $K \times K$ matrix with the weights of the k-th estimate on the diagonal, and y_k is a vector of the k-th eigenspectra. The coherences can be derived from the spectral matrix by

$$K_{ij}^2(f) = \frac{S_{ij}(f) S_{ij}^*(f)}{S_{ii}(f) S_{jj}(f)}, \tag{3.17}$$

where S_{ij} is the i,j-th element of the spectral matrix. The spectral matrix is an estimate of the spatial covariance sampled at each of the sensor separations and as such is also a fundamental quantity for the computation of wavenumber spectra, as will be seen next.

BEAMFORMING

As the power spectrum in time yields a useful statistic, so does the power spectrum in the space dimensions. The operation of forming the wavenumber spectrum, often called beamforming, is a spatial decomposition of the measured wavefield used to determine the bearing of

noise-generating sources and the velocity or slowness of the energy propagating from them. This can be seen by writing the two-dimensional spatial Fourier transform

$$x(\mathbf{x},t) = \frac{1}{8\pi^3} \int_R y(\mathbf{k},\omega) e^{i(\mathbf{k}\cdot\mathbf{x}-\omega t)} d\mathbf{k} d\omega. \tag{3.18}$$

The component $e^{i(\mathbf{k}\cdot\mathbf{x}-\omega t)}$ corresponds to a unit amplitude plane wave propagating with a velocity $c=|\mathbf{k}|/\omega$ and bearing $\theta=\tan^{-1}k_y/k_x$, so the time and space domain wavefield is a weighted summation of all such components.

From this point on, assume that the temporal transform of the data has been performed. Unlike Fourier transforms of time sampled data, spatial data are typically very sparsely sampled and FFT methods are generally not used. Instead a sum over the small number of components is computed. Writing this explicitly,

$$y(\mathbf{x}) = \hat{y}(\mathbf{x}) \sum_{n=1}^{N} \delta(\mathbf{x} - \mathbf{x}_n), \tag{3.19}$$

where $\hat{y}$ is the actual and wavefield and y is the sampled wavefield. Taking the Fourier transform of both sides and by the convolution theorem,

$$Y(\mathbf{k}) = \hat{Y}(\mathbf{k}) * \frac{1}{4\pi^2} \int_{R^2} \sum_{n=1}^{N} \delta(\mathbf{x}-\mathbf{x}_n) e^{i\mathbf{k}\cdot\mathbf{x}} d\mathbf{x} \tag{3.20}$$

$$Y(\mathbf{k}) = \hat{Y}(\mathbf{k}) * \frac{1}{4\pi^2} \sum_{n=1}^{N} e^{i\mathbf{k}\cdot\mathbf{x}_n}. \tag{3.21}$$

If we define the complex array response

$$B(\mathbf{k}) = \frac{1}{4\pi^2} \sum_{n=1}^{N} e^{i\mathbf{k}\cdot\mathbf{x}_n}, \tag{3.22}$$

then

$$Y(\mathbf{k}) = \hat{Y}(\mathbf{k})*B(\mathbf{k}). \tag{3.23}$$

The measured wavenumber spectrum is the convolution of the true wavenumber spectrum with the array response. More commonly the power is calculated since the phase of a two-dimensional field is difficult to interpret,

$$P(\mathbf{k}) = |Y(\mathbf{k})|^2 = |\hat{Y}(\mathbf{k})*B(\mathbf{k})|^2. \tag{3.24}$$

There are a variety of specialized algorithms in common usage: the conventional

(Bartlett) method [*Lacoss et al.*, 1969], the maximum likelihood (ML) method [*Capon*, 1969], the linear prediction method [*Lang and McClellan*, 1976; *Makhoul*, 1982], and eigenvector methods [*Schmidt*, 1986]. Analysis of the CIRCUS noise data have been performed only with the conventional and ML methods because they are relatively independent of model assumptions.

The conventional estimate is simply the modulus squared of the complex spatial transform. It can be rewritten concisely using matrix notation. Let e(k) be the "steering" vector whose elements are $e_j = e^{i\mathbf{k}\cdot\mathbf{x}_j}$, and let y($f$) be the vector of spectral estimates at each sensor. Then the discrete spatial Fourier transform of y becomes

$$Y(f,\mathbf{k}) = \mathbf{e}(\mathbf{k})^H \mathbf{y}(f),$$ (3.25)

and

$$P_{Conv}(f,\mathbf{k}) = E[|Y(f,\mathbf{k})|^2] = \mathbf{e}^H E[\mathbf{y}\mathbf{y}^H]\mathbf{e}.$$ (3.26)

Substitute the definition for the spectral matrix (Equation 3.14) and

$$P_{Conv}(f,\mathbf{k}) = \mathbf{e}^H S \mathbf{e}.$$ (3.27)

From Equation (3.15) it is evident that the resolution of the conventional wavenumber estimate is limited by the width of the central lobe of the array response $B^2(\mathbf{k})$. Sometimes a weighted steering vector is used where $e_j = w_j e^{i\mathbf{k}\cdot\mathbf{x}_j}$, to reduce the sidelobes of the array response, but weighting by conventional windows cannot decrease the width of the central lobe.

Non-linear estimates of the wavenumber spectrum can overcome this limitation. *Capon* [1969] derived a method which achieves better resolution by making the weights, or steering vectors adapt to the data. The weights are computed for an optimal window for each wavenumber, frequency and spatial signal and noise structure to reject both independent sensor noise and interfering propagating signals. A filter is sought that will pass a target plane wave undistorted with unity amplitude and also minimize the total power output of the array. Let $\mathbf{a} = col[a_1, \cdots, a_N]$ be the vector of weights. The first condition results in the constraint equation

$$\mathbf{a}^H \mathbf{e} = 1,$$ (3.28)

and the second condition is

$$P_{Capon}(k) = \min_{a(k)} E\left[a^H Sa\right].$$ (3.29)

Use the method of Lagrangian multipliers to minimize

$$F = a^H Sa - \mu(a^H e - 1).$$ (3.30)

Minimize F by taking the gradient with respect to a and setting it to zero.

$$\nabla_a \left[a^H Sa - \mu(a^H e - 1)\right] = 0,$$ (3.31)

$$2Sa - \mu e = 0,$$

or,

$$a = -\frac{\mu}{2} S^{-1} e.$$

Substitute a into the constraint equation (Equation 3.26) to solve for the multiplier,

$$-\frac{\mu}{2}\left[S^{-1} e\right]^H e = 1,$$

and

$$\mu = -\frac{2}{e^H S^{-1} e},$$

and so

$$a = \frac{S^{-1} e}{e^H S^{-1} e}.$$ (3.32)

Substituting the weights a into the power output of the array (Equation 3.24),

$$P_{Capon}(f,k) = \left[\frac{S^{-1} e}{e^H S^{-1} e}\right]^H S\left[\frac{S^{-1} e}{e^H S^{-1} e}\right]$$

$$P_{Capon}(f,k) = \frac{1}{e^H S^{-1} e}.$$ (3.33)

This estimator was named by *Capon* [1969], the maximum likelihood estimator. It does not actually correspond to the estimator derived from the maximum likelihood analysis but it is very similar in form [*Johnson*, 1982; *Kay and Marple*, 1982]. The method will be referred to as Capon's method henceforth.

The performance of any array processing method can be gauged by its resolution, bias

and stability. These quantities are sensitive to errors such as uncertain sensor positions, correlation between signal and noise, and inaccurate assumptions of the signal model. These errors are difficult to estimate for the present study. Great expense and effort was spent making the sensor positions accurate to within 3% of the aperture. Since the ambient noise is the object of study, the distinction between signal and noise becomes fuzzy. Clearly the signal to noise ratio is one, and there is a high degree of correlation between signal and noise. The signal model needs to be as unrestrictive as possible.

The conventional method has resolution limited by the beam pattern inherent in the array geometry. *Lacoss et al.*, [1969] showed that the stability of the conventional estimate depends on the redundancy in the co-array and the time-bandwidth product of the cross-spectrum estimate, with an array geometry factor. The only model assumption made is that the signal of interest is composed of plane waves.

Capon's method can achieve improved resolution because it actually makes use of the coherence structure of the noise. *Capon et al.*, [1973] showed that the method was highly effective at removing an interfering signal that was highly correlated. But the question of correlation between signal and noise has not been answered.

Other methods can achieve even better resolution than Capon's method, but they usually make stringent assumptions about the signal which may not be accurate and cannot be checked. For instance, the linear prediction methods assume an all-pole model for the signal and that the number of poles is known. The eigenvector methods are most effective when there are a small number of discrete sources, where small means much fewer than the number of sensors.

Figure 3.4 compares a wavenumber spectrum computed with the conventional method and Capon's method for a synthetic signal. The time series is a 2 Hz sine wave with a phase delay corresponding to a propagation velocity of 0.5 km s^{-1} (2 s km^{-1}) towards the south and 10% additive white noise. The conventional method obviously has significant sidelobe

energy and a broad main peak. However the power level is approximately correct. The estimate with Capon's method yields a much sharper spike, but the peak power level bears no simple relationship to the input. Wavenumber spectra have been computed with Capon's method in this study as a general rule. However it is has proven a useful check to compare the results with the conventional method.

Figure 3.1. Microseism spectral estimates using the segment averaged Fourier transform method showing the trade-off between variance and resolution. The dashed lines indicate the 95% confidence interval. The time-bandwidth product reduces to the number of segments used in the averaging. Because the record is of finite length, more averaging means less resolution.
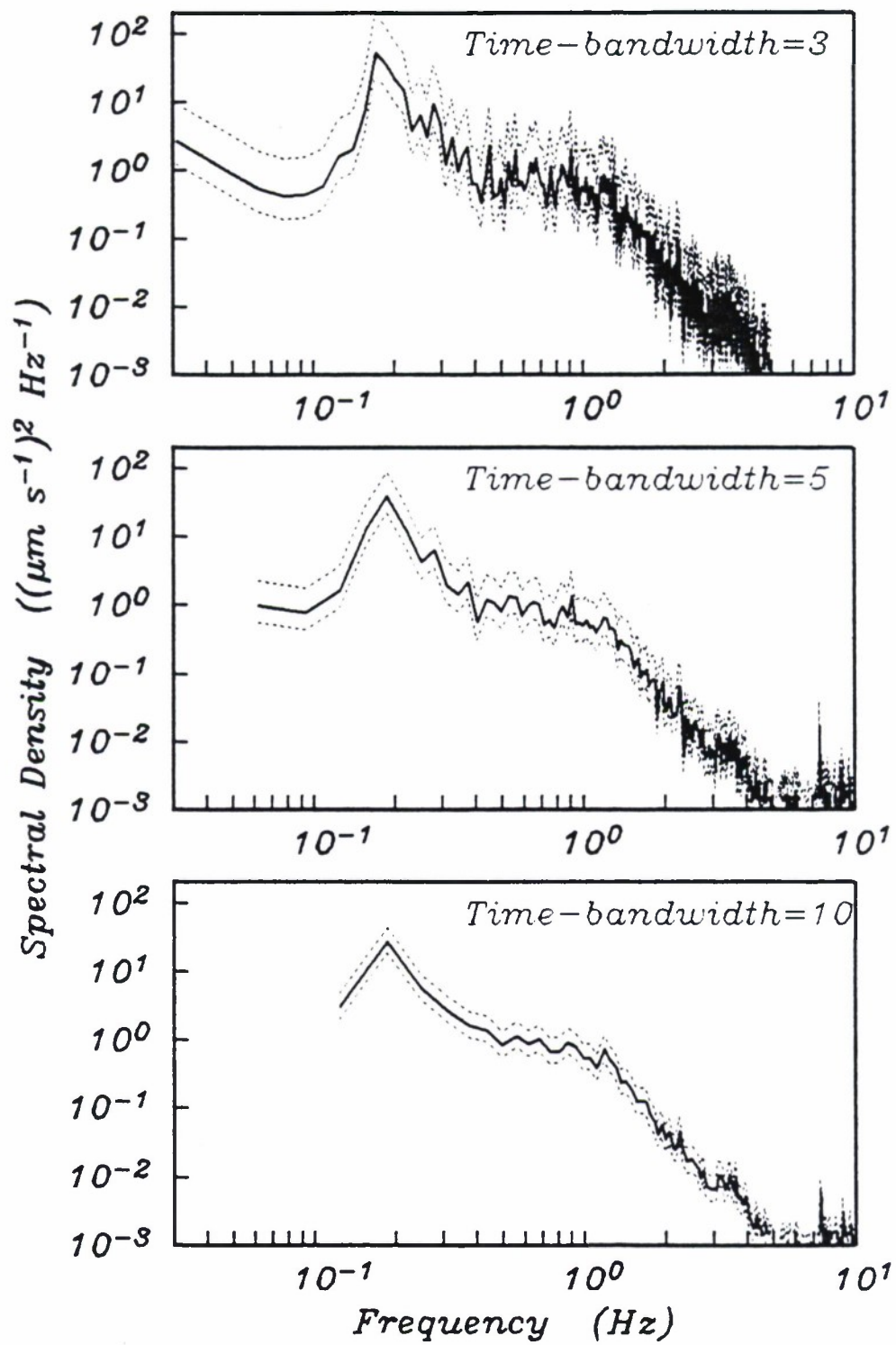
Figure 3.2. Microseism spectral estimate using the multiple taper method. The dashed lines indicate the 95% confidence interval. The length of the Fourier transform is the same for each case but the time-bandwidth product relates to the number of tapers used in the calculation. More tapers results in a broader peak.
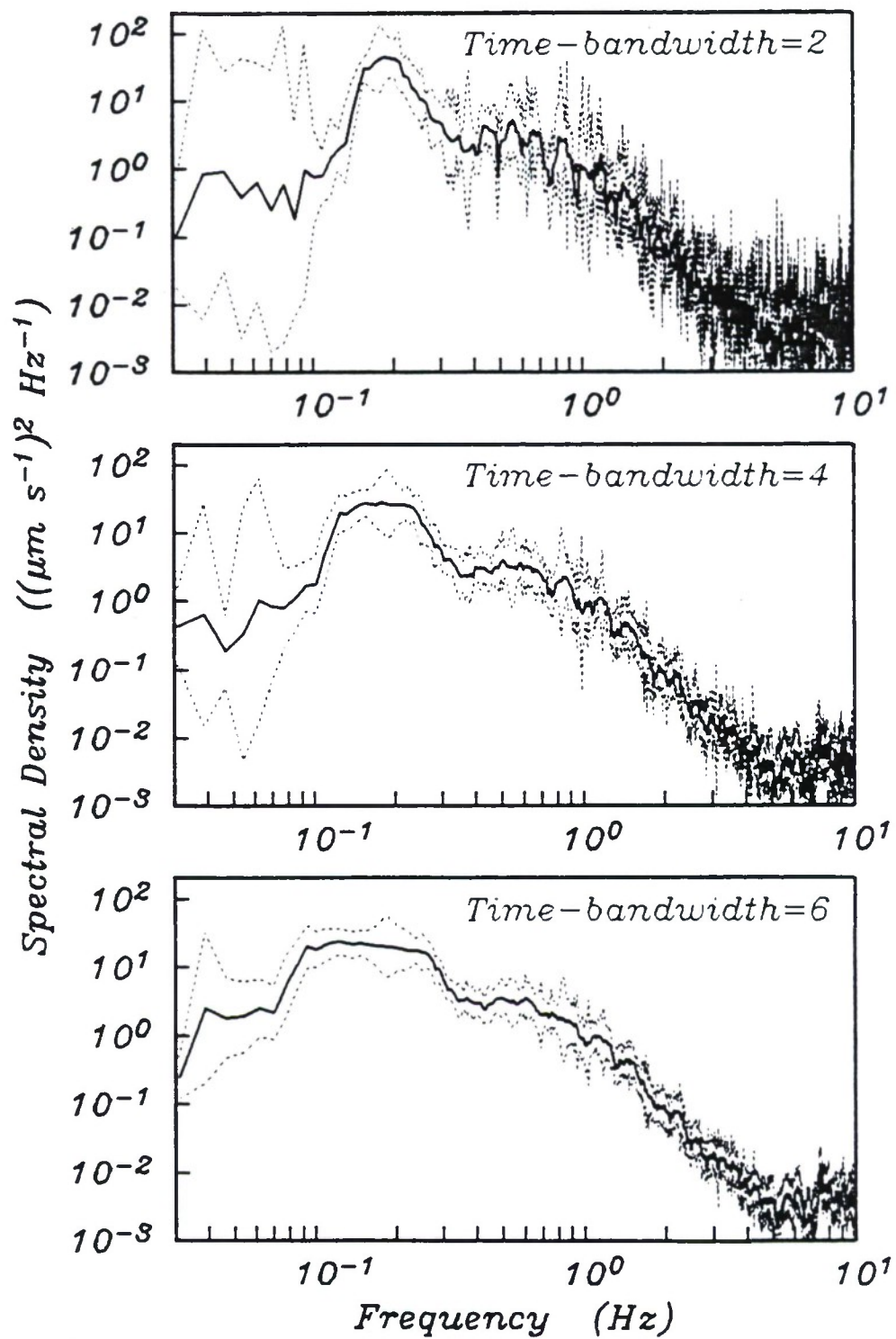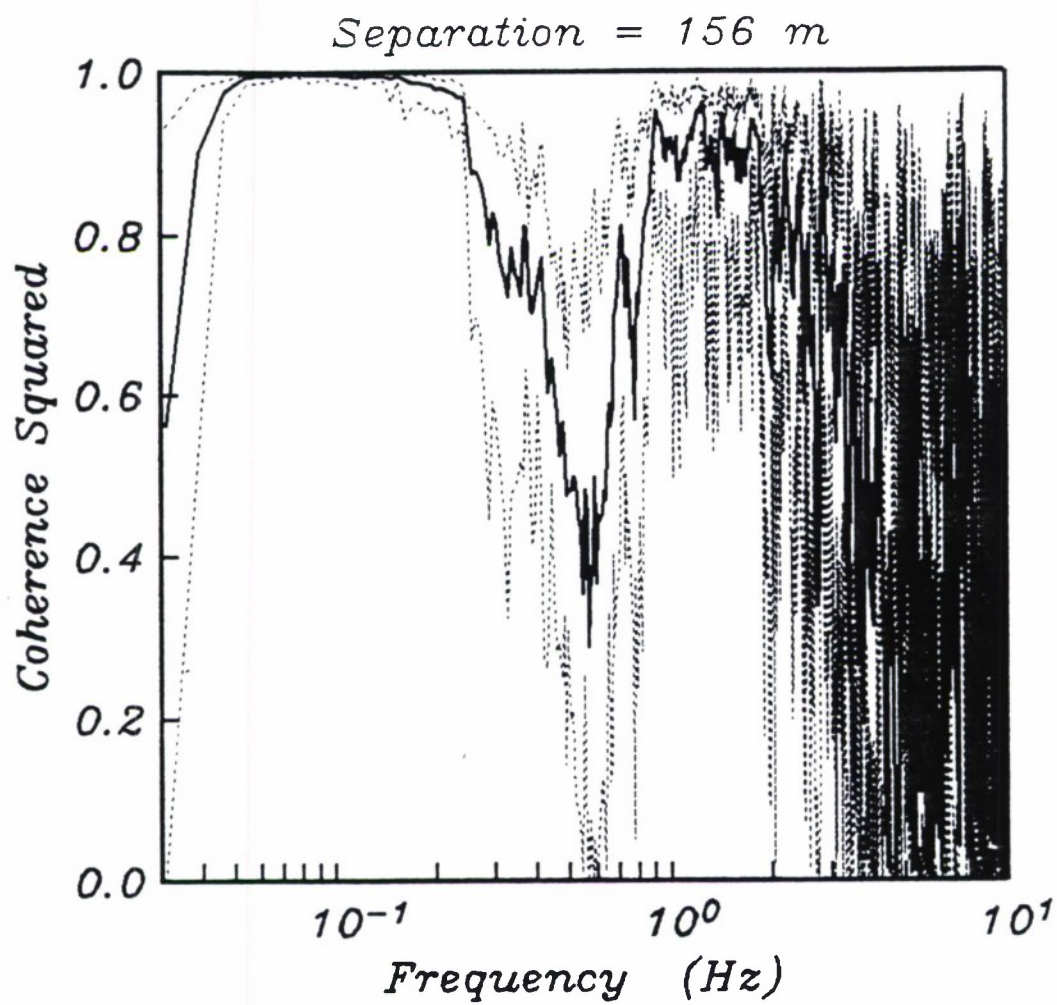
Figure 3.3. Cross-coherence between data from two vertical component seismometers separated by a distance of 156 m. The dashed lines indicate the 95% confidence interval.

Figure 3.4. Conventional and Capon's method wavenumber spectral estimates for a synthetic signal consisting of a sinusoid with phase slowness of 2 s km^{-1} propagating due south and 10% additive white noise.

Conventional Method

Capon's Method

(A)

(B)

East Slowness (s km⁻¹)

North Slowness (s km⁻¹)

dB re. Peak
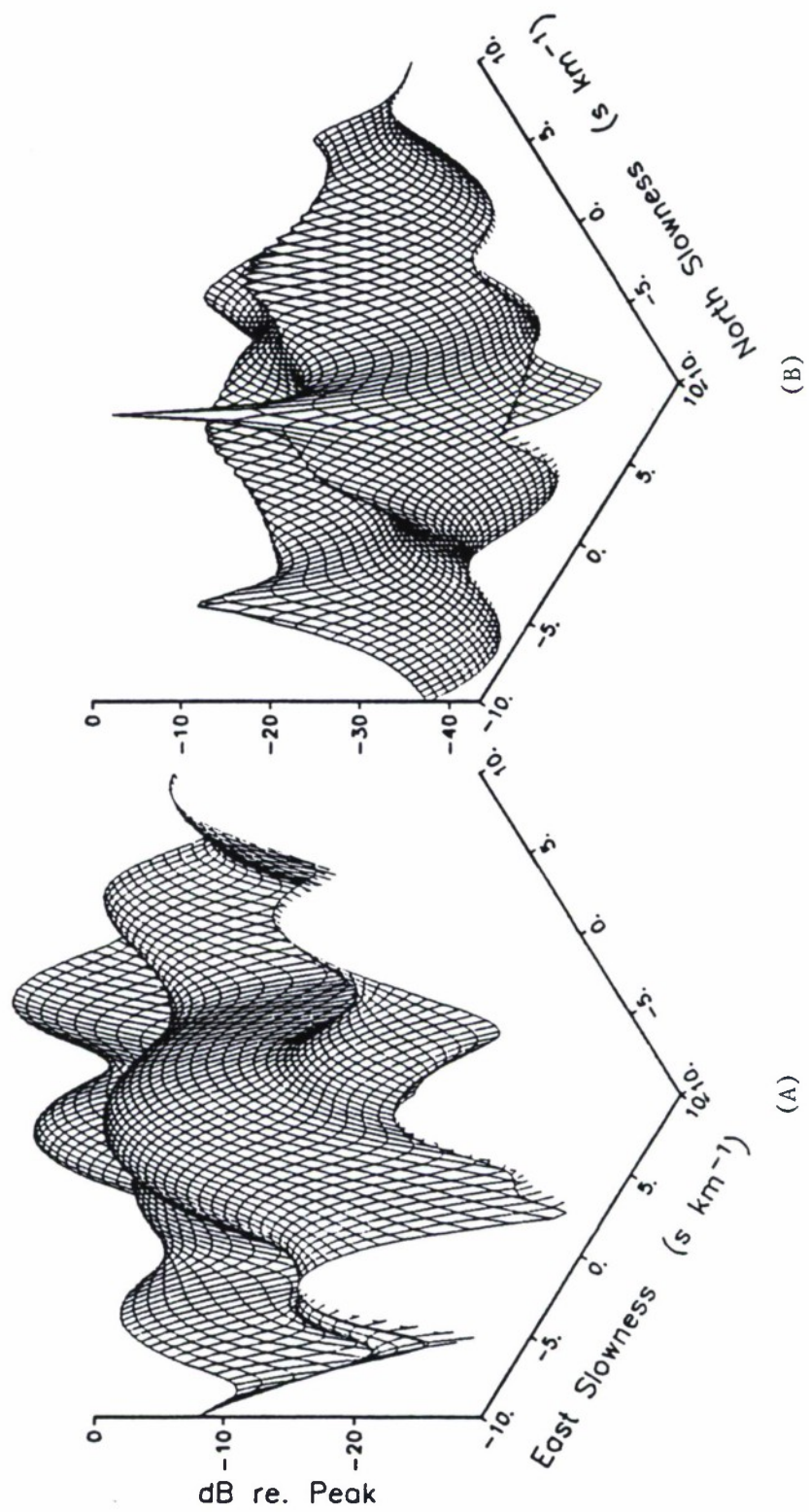
CHAPTER 4
COMPARISON OF AMBIENT NOISE WITH
SURFACE CONDITIONS

The purpose of the CIRCUS experiment was to gather noise data over a wide frequency and wavenumber band, and for a long enough time period to sample different weather conditions. The one-month deployment of the array recorded significant variability in the noise level. April and May are not times of severe weather in the northern mid-latitudes so there were no local storms during the period of observation the variability in the weather that occurred was well correlated with changes in the recorded noise levels.

NOISE SPECTRA AND THE GSOWM SWELL MODEL

The characteristics of the noise level will be described through the power spectra of the data records. Since the maximum instrument separation of 156 m, the gross features of the spectra quite consistent across all the instruments. As a result, comparisons between noise levels and surface conditions will be made with a single instrument, though not necessarily always the same one.

Figures 4.1-4.4 are synopses of an entire OBS data set. Power spectra are computed for each recording window which occur at intervals of six hours. The spectra are placed side by side with time increasing along the horizontal axis, similar to a sonogram. Each vertical scan represent a single recording window between 1/32 and 10 Hz frequency. The spectra are calculated for data segments of 64 seconds (8192 samples) by the multiple prolate spheroidal function taper method [*Thomson*, 1982]. The data are corrected for the instrument response to acceleration for the case of seismometers or to pressure changes for the hydrophone. For the purpose of plotting, the spectra are averaged over frequency bands of 1/12 octaves. Figure 4.1 is data from the vertical seismometer of OBS 8, Figures 4.2 and 4.3 are the two horizontal chan-

nels of OBS 8, and Figure 4.4 is data from the pressure sensor of OBS 6. The crystal hydro-
phone installed on OBS 8 had poor response at the lower frequencies while OBS 6 was
configured with a Cox-Webb transducer. However OBS 6 stopped recording after 17 days days
on the bottom.

The are several features of interest in these plots; refer especially to Figure 4.1. The
main peak centered between 0.1 and 0.2 Hz visible at all times, is the microseism peak. The
maximum level is variable, changing by a factor of up to 100 several times during the month.
The frequency of the microseism peak is also variable between 0.1 and 0.2 Hz. At higher fre-
quency a subsidiary wide peak appears and disappears independently of the level of the
microseism peak. There are four time intervals — at days 116, 120, 129, and 136 — where the
noise level grows especially quiet for a period of 36 hours. The horizontal channels show addi-
tional peaks at 0.3 and 0.6 Hz, but these are at multiples of the microseism peak and may be
overtones in the OBS capsule. The variation in the strength of the microseism peak in the pres-
sure (Figure 4.4) is similar to the vertical (Figure 4.1) but not identical. The variation at higher
frequency is not visible in the pressure mainly because pressure spectra have a faster roll-off
than ground acceleration; pressure is more directly comparable to ground velocity.

The deployment ships *R/V Melville* and *USNS Narragansett* did not remain on site
during the recording period and thus there are no direct measurements of the surface environ-
ment. We use instead the wind and swell hindcasts of the Global Spectral Ocean Wave Model
(GSOWM) of the U.S. Navy Fleet Numerical Oceanography Center (FNOC) [*Clancy et al.*,
1986]. A wind-wave growth model is used to compute the one-dimensional swell spectrum.
The energy is then distributed by azimuth according to the fourth power of the cosine between
the wind direction and the azimuth. Propagation of the energy is calculated along great circles
at the frequency-dependent group velocity. The initial wind state is updated four times a day
using the most accurate wind data available. Wave energy is computed for 15 frequency bins
between 0.039 and 0.308 Hz and for 24 points around the compass. The directional spectrum of

the swell and also the wind speed and direction and some miscellaneous parameters are output for grid points separated by 2.5° of latitude and longtitude at 12 hour intervals. Figure 4.5 shows the seven nearest grid points.

Figure 4.6 is the output of the GSOWM for 32.5°N, 120°W, the grid point closest to the CIRCUS array site, at a distance of 60 km. The format of the plot in Figure 4.6a is similar to Figures 4.1-4.4 except that the spectra are average of bands of 1/20 octaves and are at intervals of 12 hours.

A more quantitative comparison of the CIRCUS noise data and the GSOWM will be made later but the visual comparison between Figure 4.1 and Figure 4.6a is striking. The peaks in the swell energy at days 112-115, 121-126, and 135-142 correspond to high energy periods of the microseisms. Moreover the seismic and pressure energy peak is at twice the frequency of the swell. The time evolution of the swell peak frequency shows the deep water dispersion function. With some imagination one can see the evolution in the ocean bottom noise data as well.

Figure 4.6b is a different representation of the GSOWM output. Each polar diagram represents one time point. They are offset horizontally to line up with the corresponding time in Figure 4.6a. The vertical offset is purely for clarity of display. The cumulative swell energy is plotted as a function of azimuth with the direction corresponding to the direction of wave propagation. The circles correspond to spectral energy of 0.25 and 0.5 m^2. The wind direction and speed are also shown by the arrow. The convention is that the arrow points in the direction of propagation, which is opposite to the metereological convention. The same circles correspond to wind speeds of 5 and 10 m s^{-1} (about 10 and 20 kt respectively).

Another representation of the wind speed and direction at 32.5°N, 120°W appears in Figure 4.7. The direction is very steady, coming from NW. The speed varies between 1 and 11 m s^{-1} (2 and 23 kt respectively). The swell spectral level at 0.1 Hz and above varies with the wind speed, while the correlation between wind speed and spectral level below 0.1 Hz is less

obvious. The wind speed and swell spectra at adjacent grid points differ in important ways which will be discussed further.

The accuracy of GSOWM swell energy spectrum can be checked sporadically with wave height data from the wave rider buoy at Begg Rock (33°N, 119°W), at a distance of 110 km from the nearest grid point and 160 km from the CIRCUS site. During May 1987, the data link to Begg Rock was intermittent so the wave height data are sparse (Table 4.1). The agreement between the model and the data varies, three examples are shown in Figure 4.8.

As has been described briefly in preceding chapters, it has long been recognized that ambient noise levels at the ocean floor at frequencies below 10 Hz are primarily due to processes at the ocean surface. The theory of microseisms will be stated briefly and then a comparison between the ocean surface model and the bottom noise will be made.

REVIEW OF MICROSEISM THEORY

The passage of gravity waves across the water surface creates a pressure oscillation which varies with depth. Following *Phillips* [1980], let $\mathbf{u}$ be the particle velocity vector with components (u,v,w), and define a potential such that $\mathbf{u}=\nabla\phi$. The boundary condition at the ocean floor $z=-D$ is $\partial\phi/\partial z=0$ and the surface displacement is

$$\zeta=a\cos(\mathbf{k}\cdot\mathbf{x}-\omega t), \tag{4.1}$$

where k and ω are related by the dispersion equation

$$\omega^2 = gk\tanh kD. \tag{4.2}$$

The velocity potential is

$$\phi = \frac{\omega a\cosh k(z+D)}{k\sinh kD}\sin(\mathbf{k}\cdot\mathbf{x}-\omega t). \tag{4.3}$$

The pressure to first order as a function of depth is found from

$$p(z) = -\rho gz - \rho\left[\frac{\partial\phi}{\partial t}\right]_z. \tag{4.4}$$

Substituting in (4.2) and (4.3) yields

$$p(z) = -\rho gz + \rho ga\frac{\cosh k(z+D)}{\cosh kD}\cos(\mathbf{k}\cdot\mathbf{x}-\omega t). \tag{4.5}$$

The first term is the hydrostatic pressure. The dynamic pressure on the bottom $z=-D$, reduces to

$$p(D) = \frac{p(0)}{\cosh kD}.$$ (4.6)

When $kD \gg 1$ this quantity becomes negligible.

By taking the analysis to second order, it is found that there can be a substantial pressure signal on the bottom, even in deep water [*Miche*, 1940; *Longuet-Higgins*, 1950]. Still following *Phillips* [1980], the horizontal spatial mean of the pressure up to second order terms is

$$\bar{p}(z) = g \int_z^0 \rho dz + \rho(0) \frac{\partial}{\partial t} \overline{\zeta w(0)} - \overline{\rho(z) w(z)^2}.$$ (4.7)

The first term is the hydrostatic pressure and the last term can be shown to attenuate exponentially with depth. The second term vanishes if the spatial mean is constant over time as is the case for a traveling wave. However for a standing wave,

$$\zeta = a \cos(\mathbf{k} \cdot \mathbf{x}) \cos(\omega t),$$ (4.8)

this term becomes

$$\bar{p}_1 = -\frac{1}{2} \rho(0) a^2 \omega^2 \cos 2\omega t.$$ (4.9)

The frequency of the pressure oscillation is double that of the surface wave, and the amplitude is proportional to the square of the amplitude and the square of the frequency of the surface wave.

Longuet-Higgins [1950] considered a rigid ocean bottom, *Hasselman* [1963] extended the analysis to include an elastic medium below the water layer. Two important results accrued from this. First, the elastic medium was found to be excited primarily by a source in the water with phase velocity equal to that of the resonant modes in the solid. Second, and as a result of the first, it became necessary to consider, not standing waves with infinite phase velocity caused by exactly opposed wavenumber components, but wave trains with nearly opposite wavenumbers that produce a pressure signal with finite phase velocity. *Hasselman* [1963] derived an expression for the pressure spectrum which included terms with sums of

wavenumbers and differences of wavenumbers. The sum terms result in components with very low phase velocity and therefore do not contribute to the microseism spectrum. The difference terms become important when $k_1 \approx -k_2$. The approximation to the pressure spectrum just below the ocean surface then becomes

$$P(\mathbf{k},\omega) = \frac{\rho^2 g^2 \omega}{2} \int_{-\pi}^{\pi} Z(\omega/2,\theta) Z(\omega/2,\theta+\pi) d\theta. \qquad (4.10)$$

The pressure oscillation will only propagate away from the sea surface if $|\mathbf{k}| \leq \omega/\alpha$. By integrating over wavenumber between $0 \leq |\mathbf{k}| \leq \omega/\alpha$, the frequency dependence for a point measurement of the pressure on the ocean floor becomes

$$P(\omega) = \frac{\pi \rho^2 g^2 \omega^3}{4\alpha^2} \int_{-\pi}^{\pi} Z(\omega/2,\theta) Z(\omega/2,\theta+\pi) d\theta. \qquad (4.11)$$

The pressure spectrum is determined by an integral over azimuth of the product of the directional swell spectrum with itself evaluated in the opposite direction and all evaluated at half the frequency of the pressure. Equation (4.11) includes no effect from the bottom.

Swell energy at a given frequency but with opposing direction may have several causes. *Haubrich et al.* [1963] demonstrated convincingly that reflections of swell may lead to wave-wave interactions. There were several lines of evidence for this conclusion. There was no appreciable time delay between the variation in the swell spectrum and the variation in the seismic spectrum indicating that the generating area was very close to the coast. The measured beamwidth of the seismic energy was also consistent with a generating area in a narrow strip in the ocean near the receiver. Finally, the narrowness of the microseism spectral peak limited the difference in propagation distance of the interacting swell sets and constrained the interaction to be near the coast.

There has not been enough data collected to determine if the microseism level in the ocean varies with distance from the coast. It is known that there is a double frequency microseism presence in the open ocean. An alternative way in which wave-wave interactions could be generated is if the wind direction varies rapidly and generates a new swell field on top of the old

one [*Kibblewhite and Ewans*, 1986]. However, though the level may not be as high, the double frequency energy on the ocean floor appears to exist independently of events such as wind shifts. The directional spectra of local wind waves appear to have a spread of wavenumbers, *Longuet-Higgins et al.* [1963] parametrized the directional dependence of the spectrum of the surface wave field by

$$G(\theta) = \frac{\cos^{\mu}[\frac{1}{2}(\theta - \theta_0)]}{2^{-1-\mu}\pi^{1/2}\Gamma(\frac{\mu}{2}+1)/\Gamma(\frac{\mu}{2}+\frac{1}{2})}. \tag{4.12}$$

This parametrization was supported by observations by *Tyler et al.* [1974]. They found that the beam parameter μ varies between 1 at high frequencies and 10 at the spectral peak.

If the directional spectrum of the swell is not directly available, it is often useful to separate the frequency and directional dependence in Equation (4.11),

$$Z(f, \theta) = W(f)G(\theta) \tag{4.13}$$

[*Hughes* 1976; *Kibblewhite and Ewans*, 1986]. In this form, the pressure spectrum becomes

$$P(f) = \frac{2g^2\pi^4\rho^2}{\alpha^2}f^3W^2(f/2)\int_{-\pi}^{\pi}G(\theta)G(\theta+\pi)d\theta, \tag{4.14}$$

where $G(\theta)$ often takes the form of Equation 4.12.

The pressure field in turn, generates seismic waves in the ocean floor, and the passage of seismic waves has an effect on the pressure. The displacement of the horizontal ocean floor can be computed by the convolution integral

$$u(r, z, \omega) = \int_R G(r, z; r_0, z_0; \omega) f(r-r_0, z_0, \omega) dr_0, \tag{4.15}$$

where $f(r, z, \omega)$ is a body force, and $G(r, z; r_0, z_0, \omega)$ is the Green's function, the response to a point source at (r_0, z_0). The Green's functions can be computed numerically with a variety of methods [*Kennett and Kerry*, 1979; *Woodhouse*, 1980; *Schmidt and Tango*, 1986]. The actual application of this formula is complicated in the subject of microseisms because the source is a partially correlated distributed function [*Hasselman*, 1963]. With some manipulation, it is possible to recast Equation 4.15 in terms of a transfer function and the spatial coherence of the source.

This was used effectively by *Adair* [1985] and *Webb and Cox*, [1986]. However this will be not particularly useful in this study. The transfer function approach requires different frequencies and wavenumbers to be independent. The next chapter will present data showing that there is scattering between wavenumbers and that therefore the generation of seismic noise is more complicated than is allowed by the two-dimensional Green function approach.

COMPARISON OF SWELL AND BOTTOM NOISE

The application of Equation (4.11) to the GSOWM directional spectra should model the ocean bottom pressure spectra. A problem appears when this is attempted. In general, the directional spectral generated by the GSOWM for this area contain no energy directed in opposite directions, so application of the integral over azimuth yields zero. The wave growth part of the model includes a $\cos^4$ distribution of energy over azimuth. However, the data are provided to three decimal digits and since the quantities in the frequency and directional bins are small (in units of ft^2), the information may be lost in the output.

Instead of doing the direct integration of Equation (4.11), the one- dimensional swell spectrum is taken and multiplied by Equation (4.12) with $\mu=2$. Then Equation (4.14) is applied to generate a pressure spectrum prediction. An example computed for the grid point at 32.5°N, 120°W is shown in Figure 4.9. This grid point provided a better fit to the measurements than the one closest to the array site. The latter point, though closer to the measurements is at a location on the continental borderland and is in much shallower water.

The comparison between measured and predicted pressure is shown for three time periods in Figure 4.10. The degree of fit is variable. Certain high energy events in the recorded pressure are not predicted by the swell model. The peak in the pressure spectra for days 112-117 is much stronger than predicted and it lasts longer. As a general rule there is a local wind wave component at the higher frequencies in the GSOWM which is not visible in the pressure spectra. The relationship between wind speed and swell spectral density at 0.2 Hz is clearly evident in Figure 4.11. The wind state used to compute wave growth in the GSOWM is

updated four times a day with actual measurements [*Clancy et al.*, 1986]. These grid points are not far from land and major military and commercial shipping lanes so the wind data is expected to be accurate.

Some aspects of the OBS 8 vertical component fit the swell hindcast better than the pressure does, especially at the higher frequencies. Above 1 Hz the seismic data exhibit fairly constant levels for a given frequency, interrupted for short intervals by troughs of very low noise levels (Figure 4.1). The abrupt drop in noise level is even more evident in Figure 4.12. Examination of troughs shows that they evolve with time. The falling edge occurs first at the higher frequencies (4 Hz) and migrates down to 1 Hz over the period of about a day. The rising edge 24 to 36 hours later follows the same pattern. These troughs occur at times when the surface wind speed is low. This step-like behavior of the spectrum has also been observed by *McCreery and Duennebier*, [1989]. When the wind dies down, the waves at higher frequency are attenuated more quickly. The peak frequency of wind waves has been observed to get lower as the duration of the wind increases (e.g. *Phillips*, 1980), and this is consistent with the observations here. During a sustained wind period, the wave spectrum quickly reaches saturation with its characteristic f^{-5} frequency dependence.

The peak at days 138-143 is much more prominent in the seismic data than in the GSOWM at 32.5°N, 120°W. A plot of a wider area (Figure 4.13) shows this peak in the swell more prominently to the west. The predominant swell direction at this point is from the north, and the GSOWM propagates swell along great circles so the grid points further east may be shadowed by Pt. Conception. Only one record is available from Begg Rock at day 138 and it does not differ radically from the GSOWM hindcast (Figure 4.8). It appears then, that the generation of seismic waves at this time is taking place far to the west and propagating to the array as Rayleigh waves. A definitive way to test this would be to determine the direction of propagation of the seismic waves at this time. It will be shown, however, in the last chapter that the CIRCUS array was not able to resolve velocities at the microseism peak frequency.

Table 4.1

Begg Rock Buoy Records		
no.	day	time (CUT)
1	112	07:05
2	112	19:04
3	113	07:04
4	113	13:04
5	114	07:04
6	114	10:30
7	114	13:04
8	114	19:06
9	116	22:29
10	117	10:29
11	118	07:04
12	121	04:32
13	121	10:30
14	121	13:04
15	121	19:05
16	122	07:04
17	123	19:04
18	123	22:32
19	124	16:30
20	124	19:05
21	125	01:06
22	125	04:26
23	125	07:07
24	129	10:30
25	137	22:30
26	139	01:07
27	140	19:05

Figure 4.1. Spectral history of the vertical seismometer component of OBS 8. The horizontal axis is in days, starting with April 22 and ending with May 23. Each vertical scan is a power spectrum for a single recording window. There are four recording windows per day. The color is proportional to the decibel power as shown by the color bar on the right side. The spectra have been resampled at logarithmic intervals for the purpose of plotting.

OBS 8, Vertical
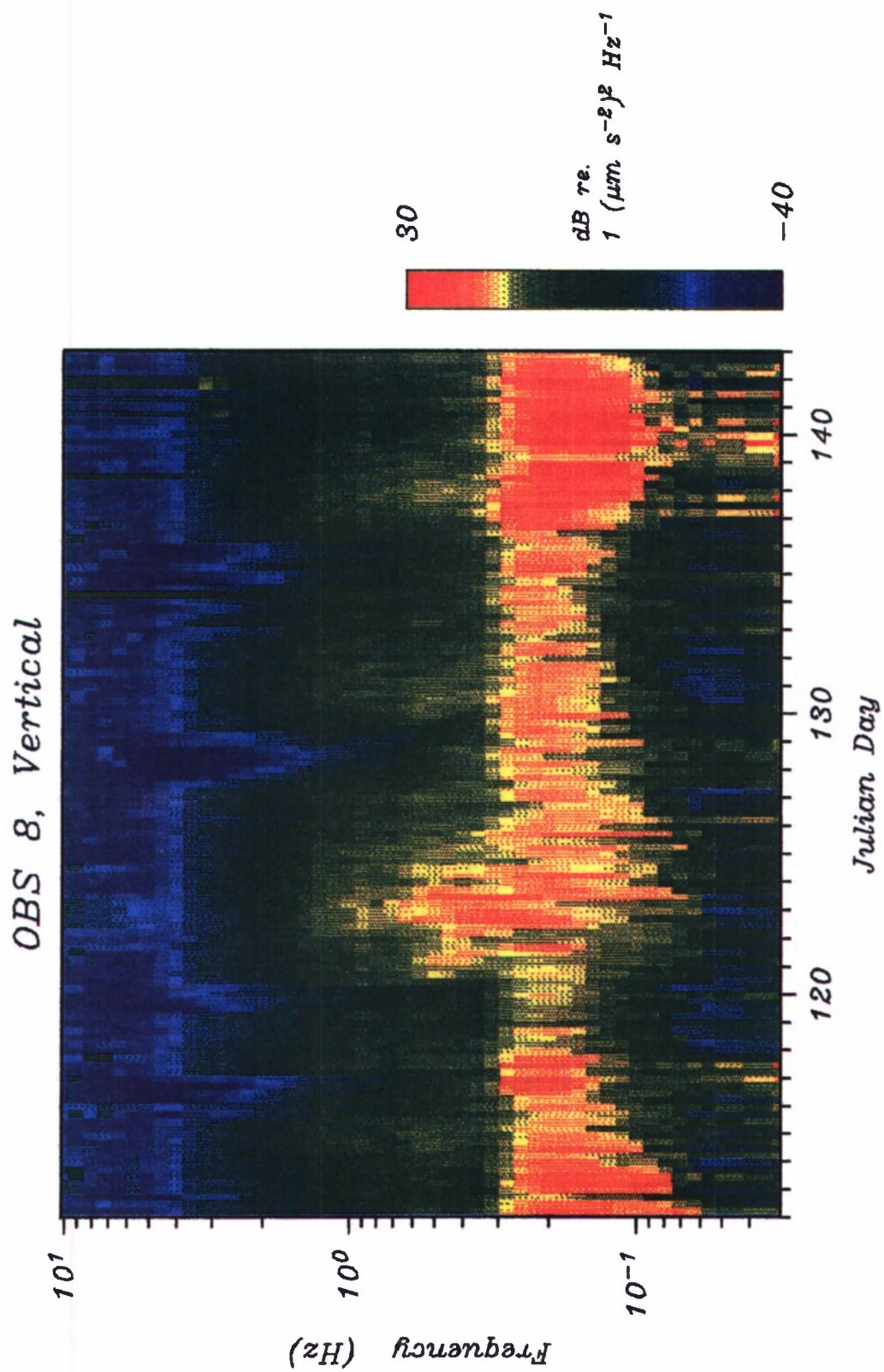
Figure 4.2. Spectral history of the first unrotated horizontal component of OBS 8. See Figure 4.1 for details of the plot.
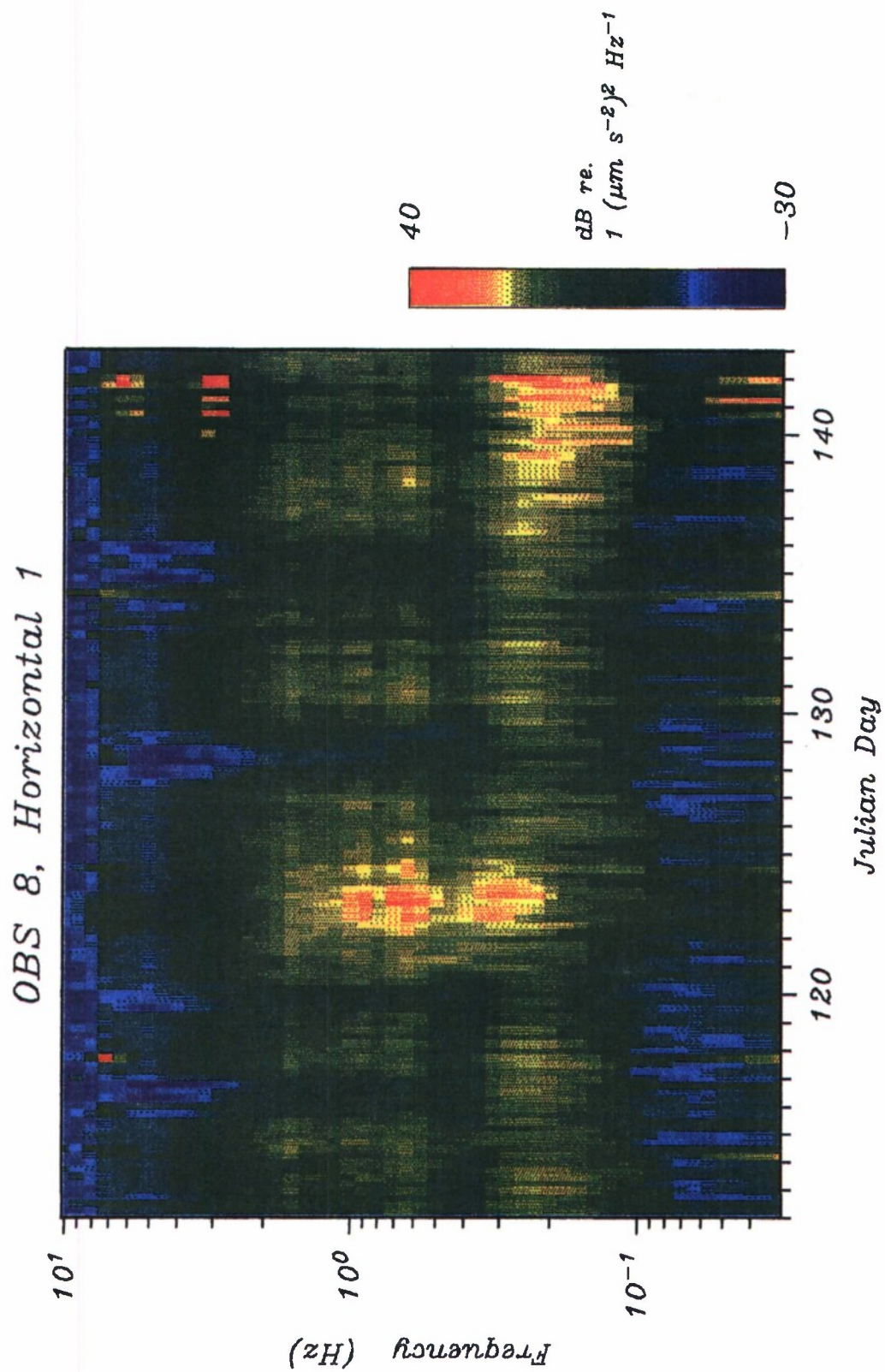
OBS 8, Horizontal 1

Figure 4.3. Spectral history of the second unrotated horizontal component of OBS 8. See Figure 4.1 for details of the plot.

OBS 8, Horizontal 2
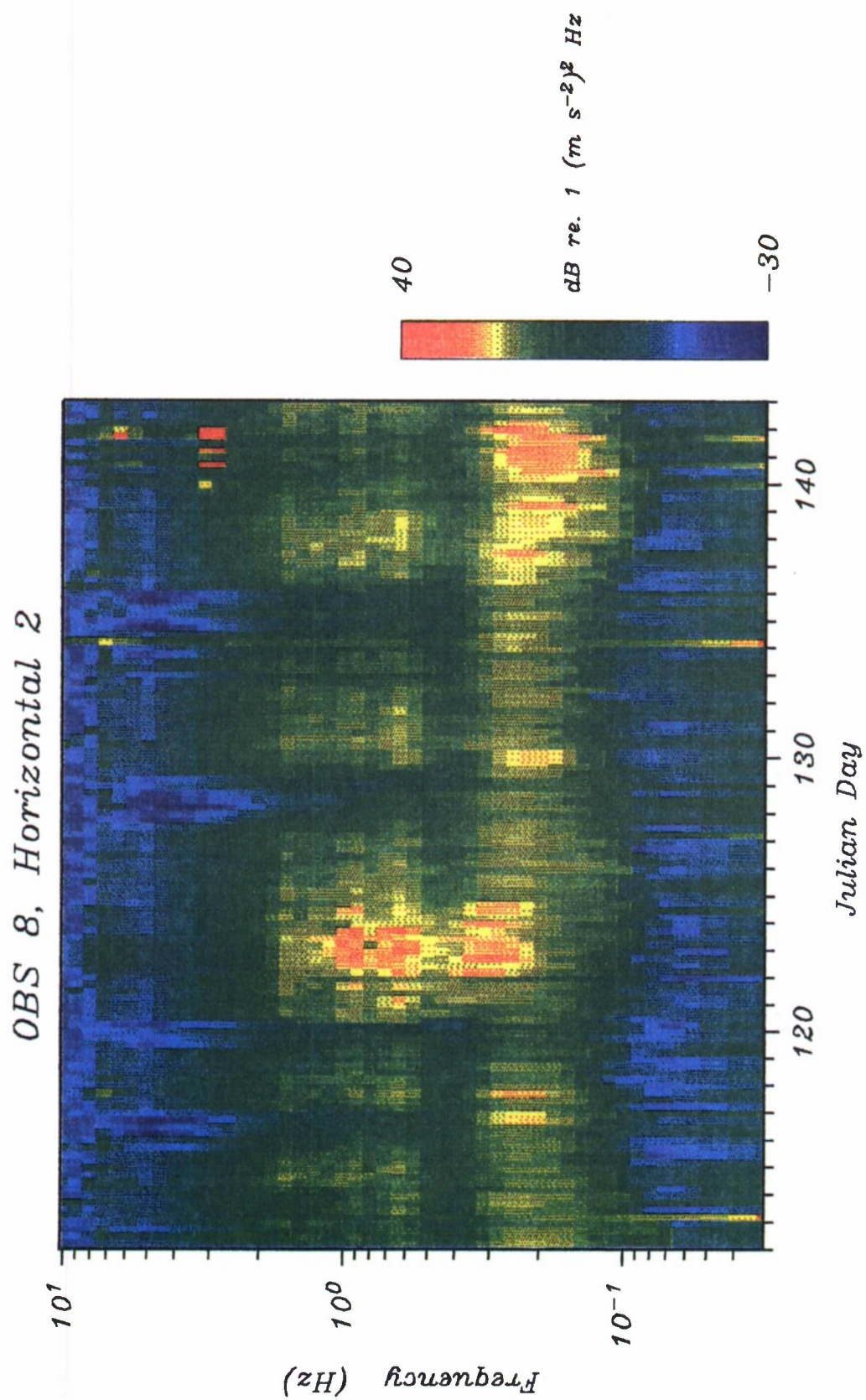
Figure 4.4. Spectral history of the pressure component of OBS 6. See Figure 4.2 for details of the plot. Blank areas indicate missing data.

OBS 6, Pressure
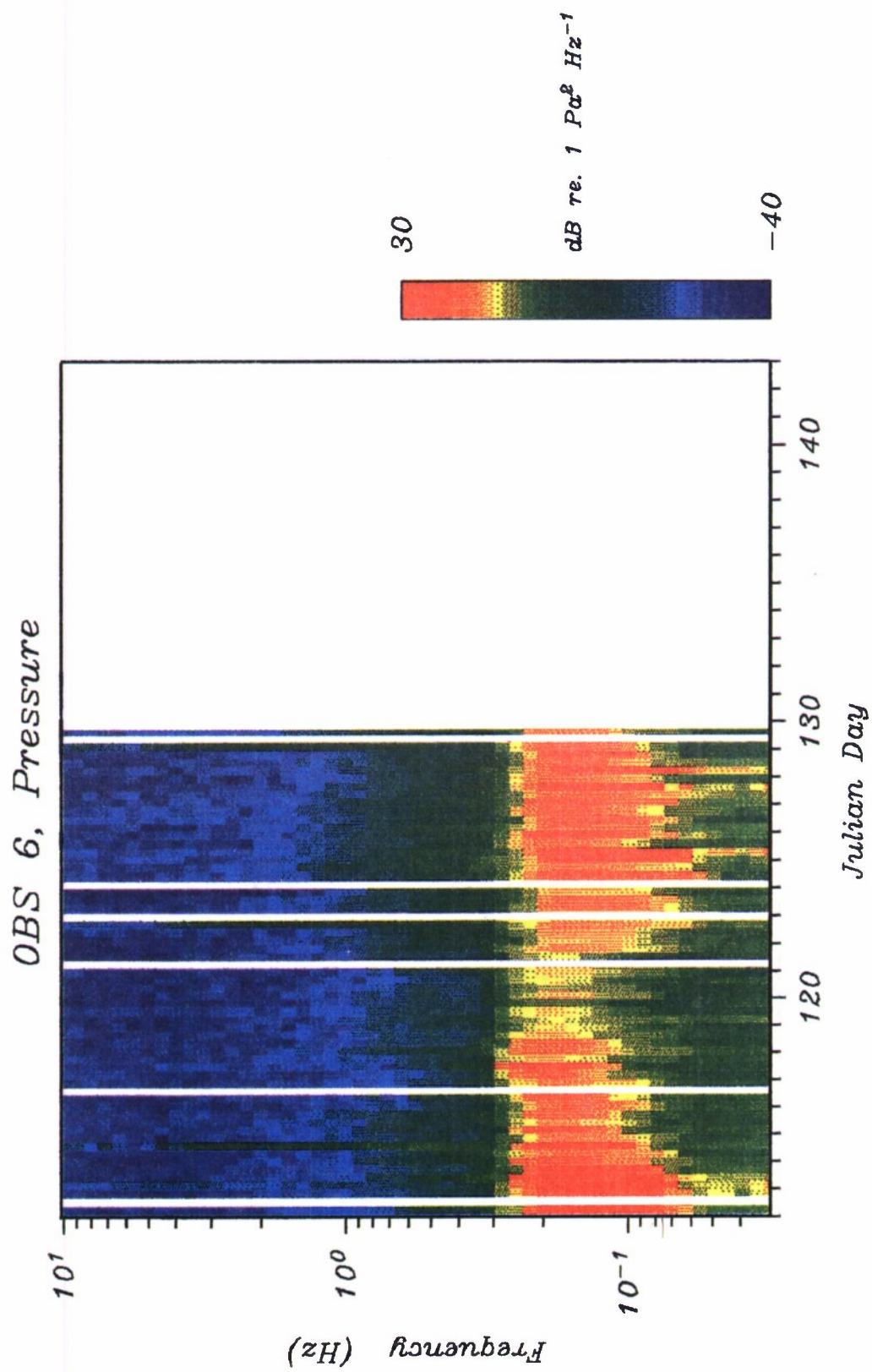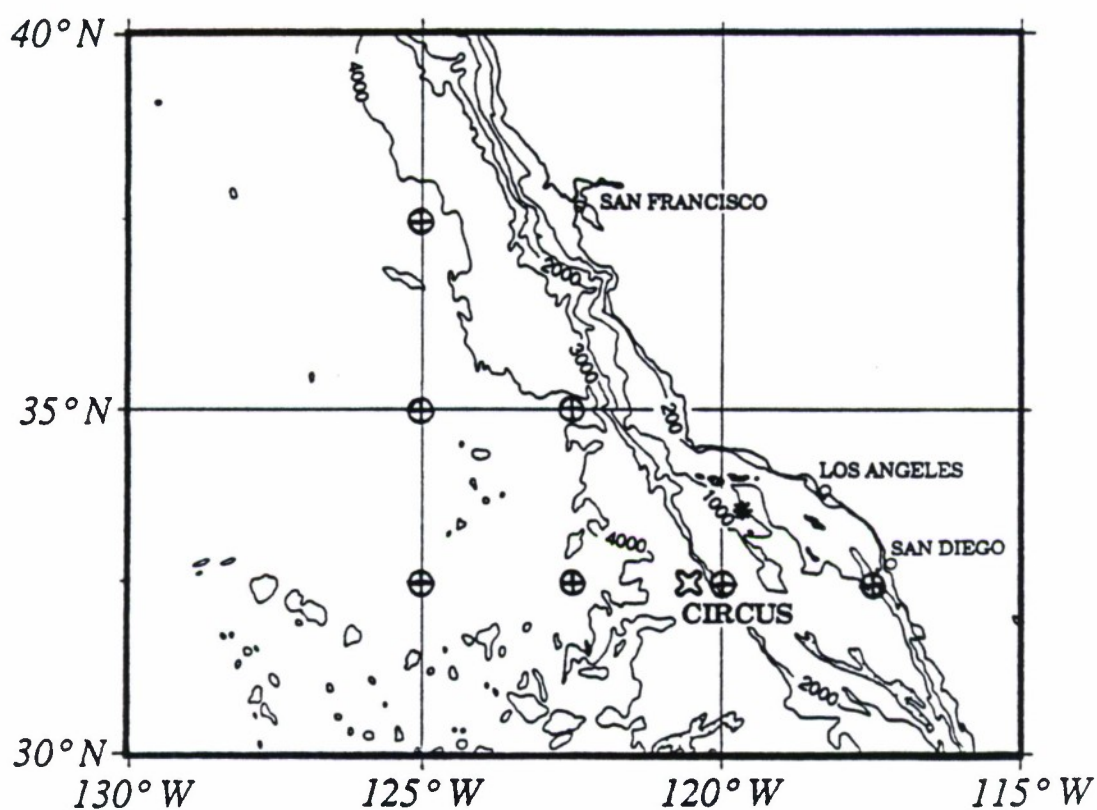
Figure 4.5. GSOWM model grid points near the array site for which data was made available by the Fleet Numerical Oceanography Center.

Figure 4.6. Spectral history of the GSOWM swell model. a) Spectral power as a function of frequency, summed over azimuth and displayed the same as in Figure 4.1, b) Directional power summed over all frequencies. The circles mark spectral energy levels of 0.25 and 0.5 m^2. The origin of the circles for each time coincides with the corresponding time in 4.6a. The wind vector is also drawn for each time.

63

GSOWM Swell Hindcast (32.5°N,120°W)
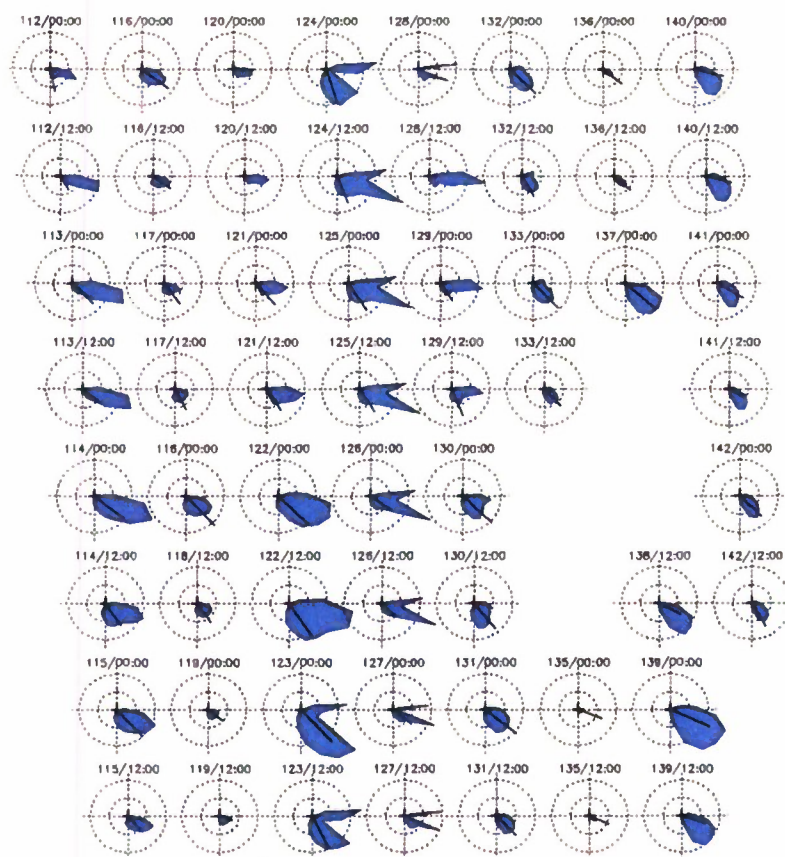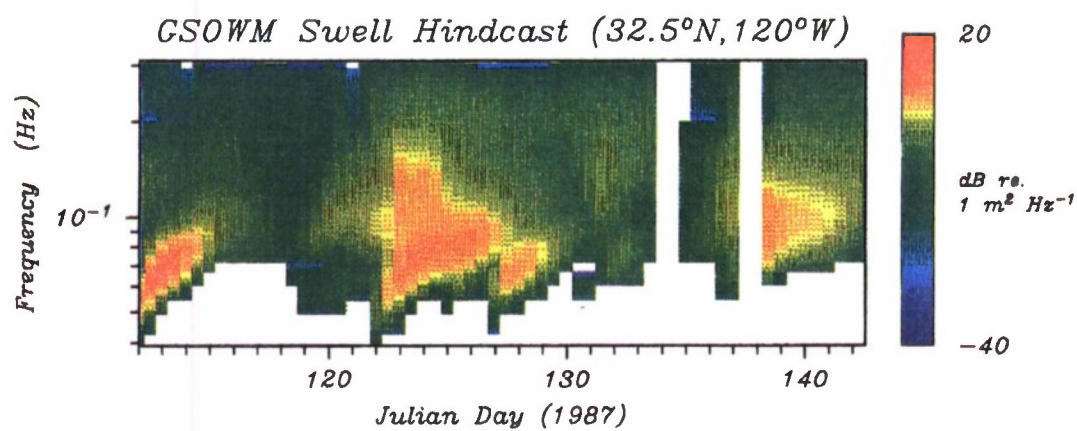
Figure 4.7. GSOWM wind speed and direction hindcast for the nearest grid point to the CIRCUS array.

65

FNOC Wind Hindcast at 32.5°N, 120°W
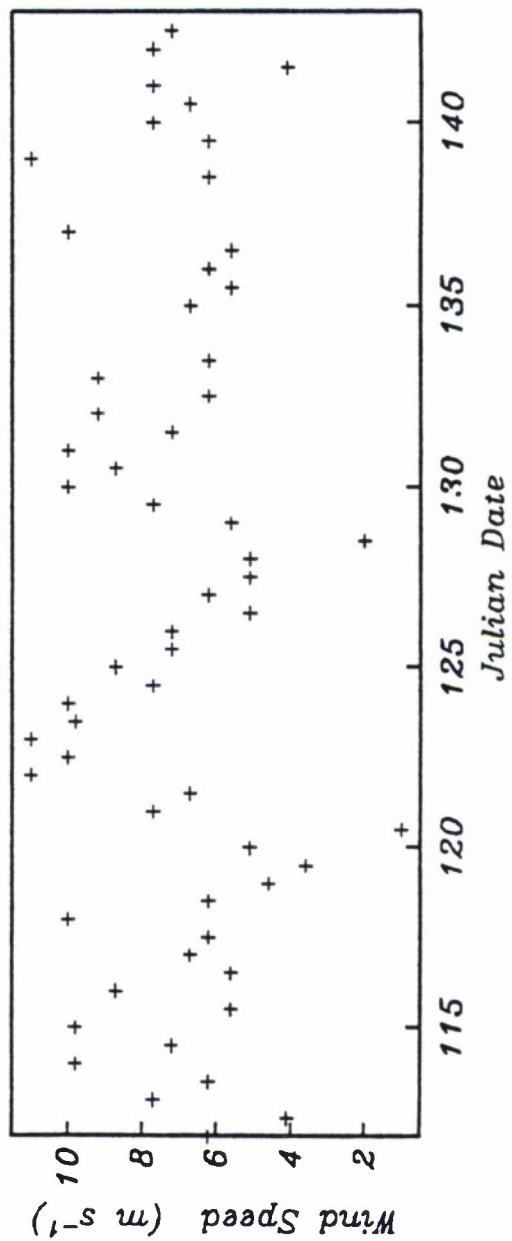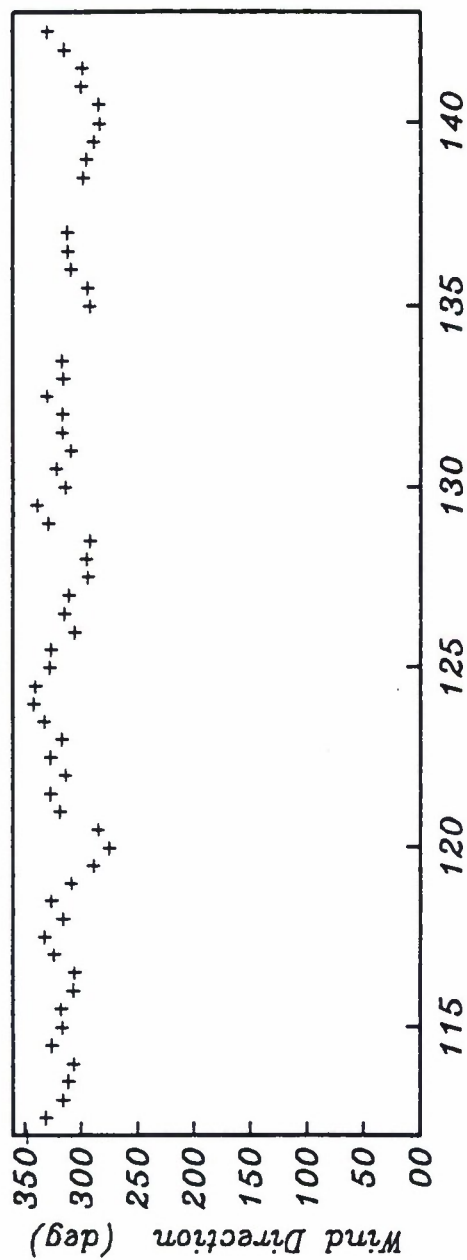
Figure 4.8. Comparison of the GSOWM swell hindcast spectrum with data from the buoy at Begg Rock at three times. The solid lines are for the Begg Rock data computed from one-minute records. The dotted lines are the swell model. a) Day 113, b) Day 117, c) Day 138.

Comparison of GSOWM and Begg Rock data

(A) Day 113 — solid Begg Rock, dash GSOWM

(B) Day 117

(C) Day 138

Spectral Density (m^2 Hz^{-1})

Frequency (Hz)
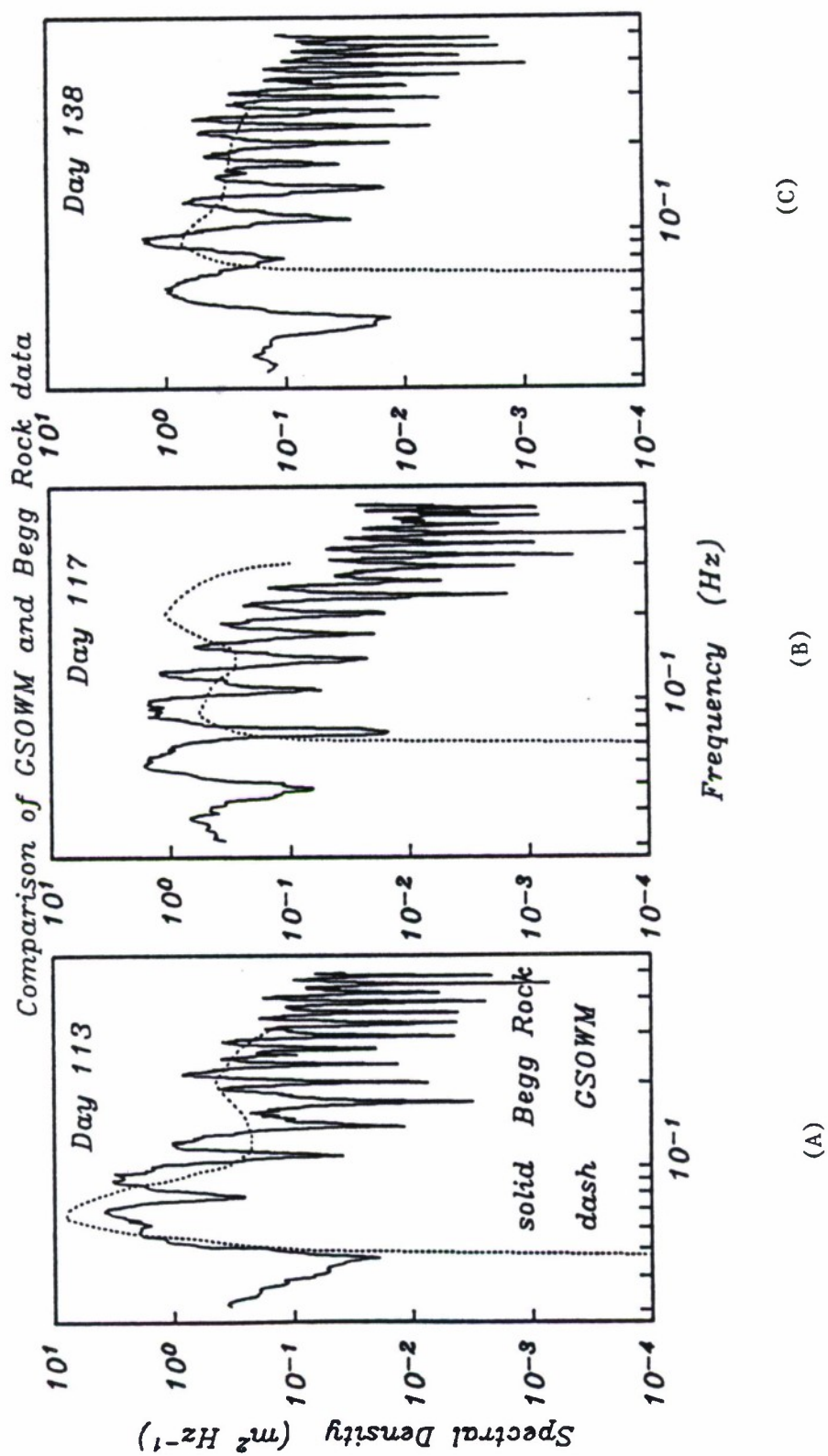
Figure 4.9. Comparison of the bottom pressure spectrum predicted from the GSOWM swell model and the CIRCUS measurements. The form of the plot is similar to those of Figures 4.6a. a) GSOWM hindcast, b) CIRCUS data.

OBS 6 Pressure

Predicted Pressure

Frequency (Hz)

Frequency (Hz)

Julian Day (1987)

dB re. 1 Pa² Hz⁻¹

40

−40
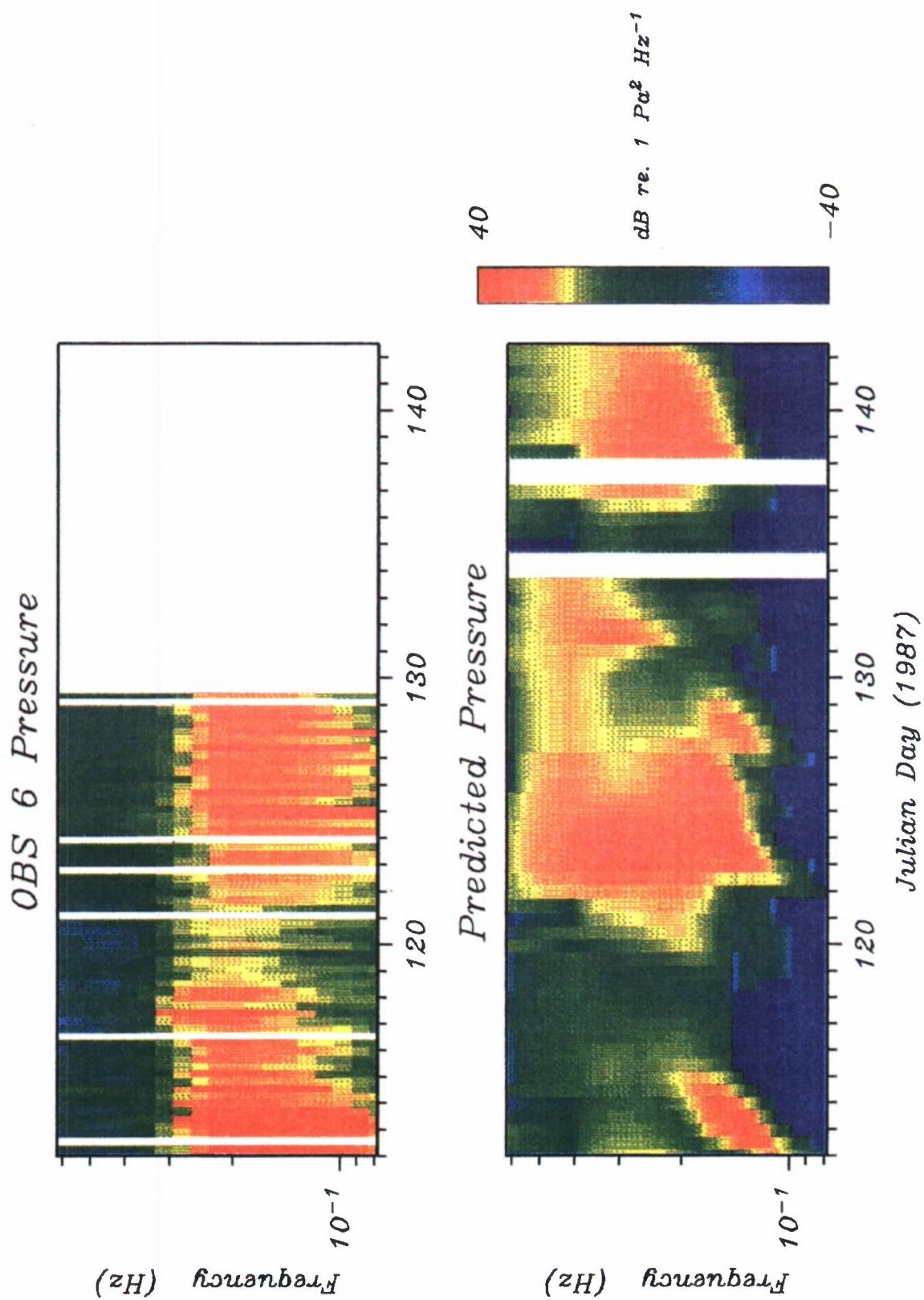
Figure 4.10. Comparison of the bottom pressure spectrum predicted from the GSOWM swell model and the CIRCUS measurements at three times. The solid lines are the CIRCUS measurements. The dotted lines are the prediction from the GSOWM swell hindcast. a) Day 113, b) Day 120, c) Day 126.

71

Measured vs. Predicted Bottom Pressure
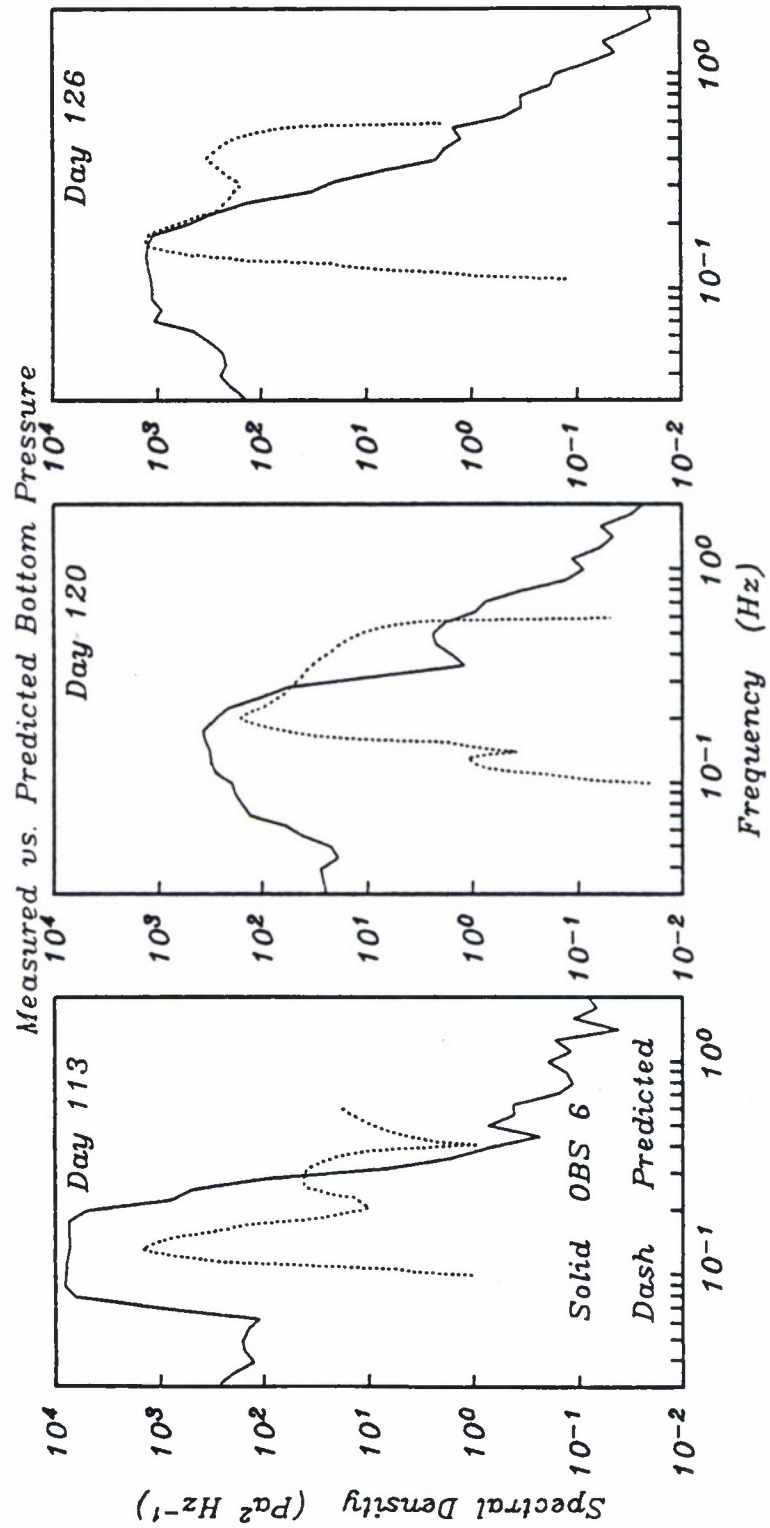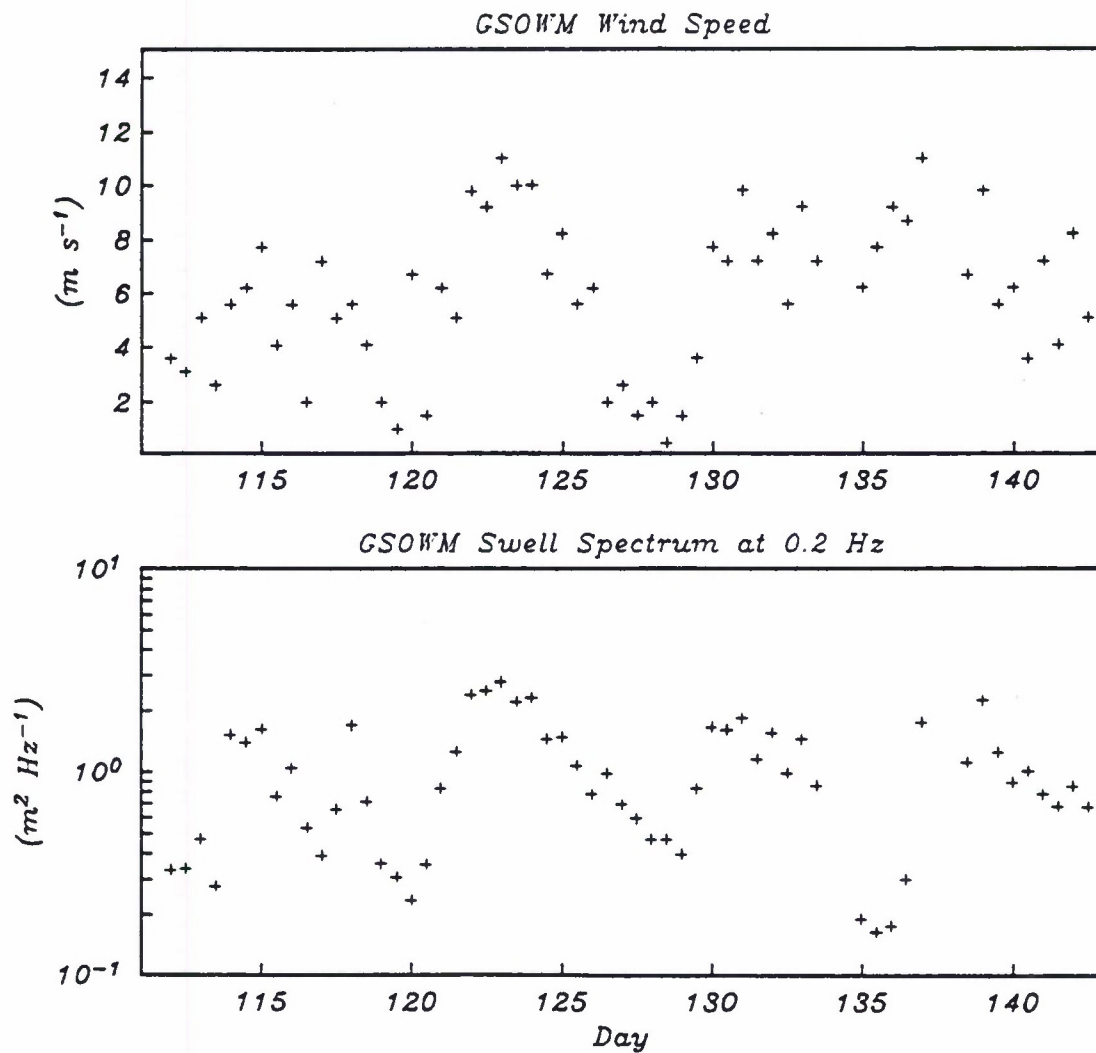
Figure 4.11. Comparison of GSOWM hindcasts for wind and swell energy at 0.2 Hz. a) Wind speed, b) Swell energy at 0.2 Hz.
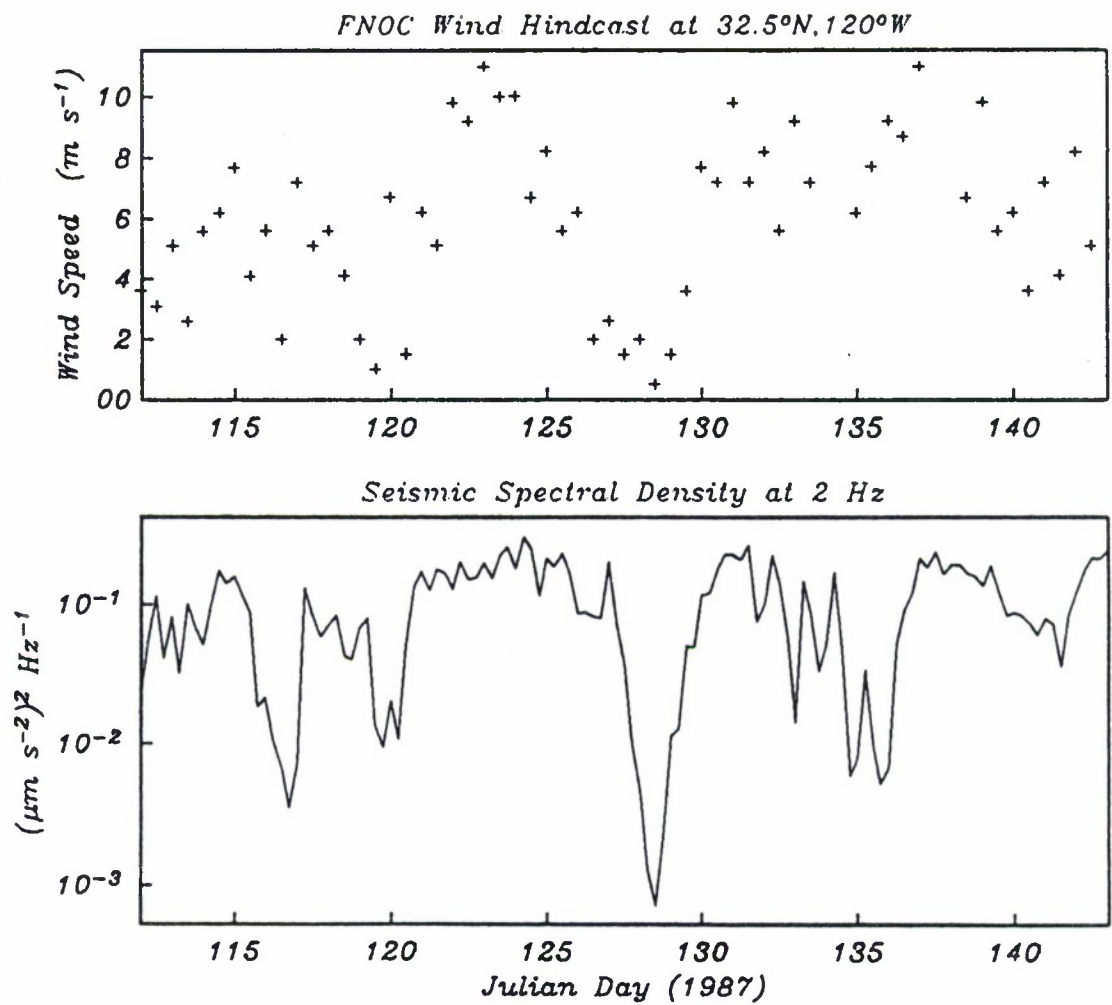
Figure 4.12. Comparison of the GSOWM hindcast for wind speed and the measured seismic noise energy at 2 Hz. a) Wind speed, b) Seismic level at 2 Hz.

Figure 4.13. GSOWM swell hindcasts at several grid points near the array. See Figure 4.6a for description of the plot.

75
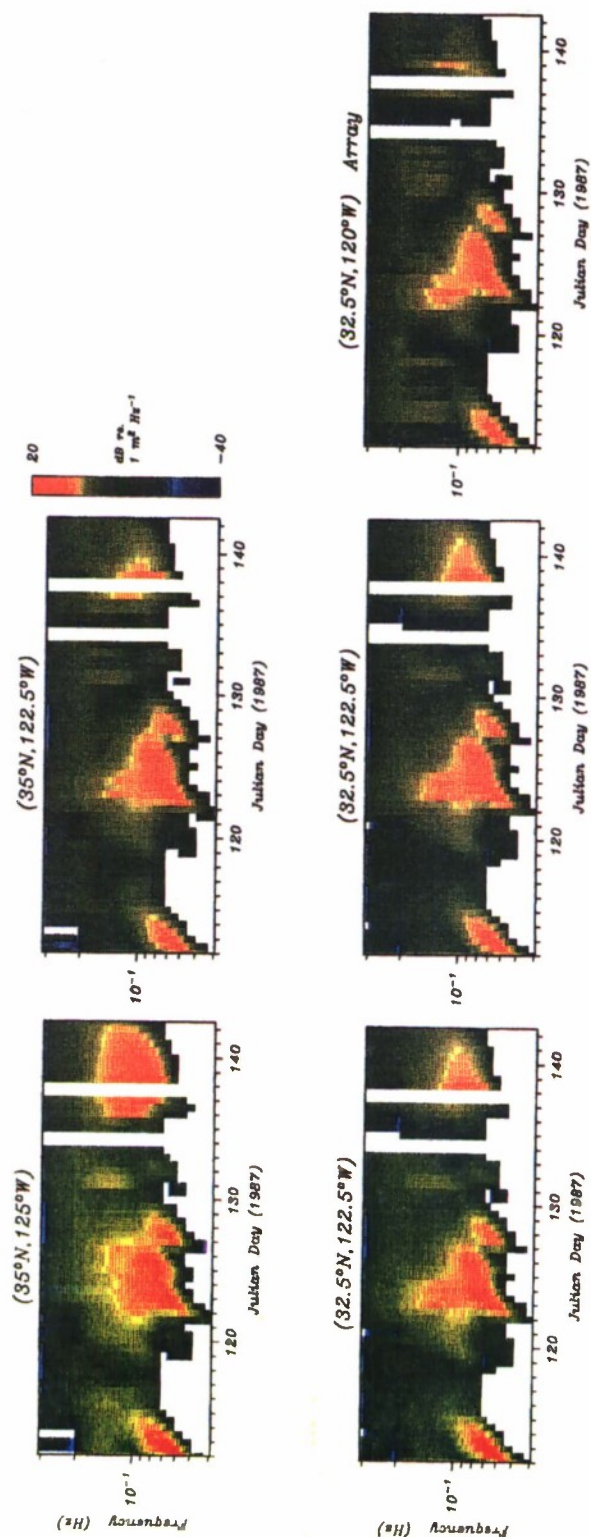
CHAPTER 5

COHERENCE MEASUREMENT AND MODELING

Multiple sensors allow the direct measurement of signal coherence, and if sensors are spaced at a variety of offsets, coherence length can be estimated. The coherence length of ambient noise has two important consequences for arrays designed to sense known signals. The first is that the array gain only becomes substantial if the sensor separations are greater than the noise coherence length. The second is that differences in coherence lengths (or wavelengths) can be used to improve the signal to noise ratio. Here the noise has short wavelengths and sensor groups act as wavenumber filters to suppress short-wavelength noise while leaving longer-wavelength signals (from ships, earthquakes, or explosions) unimpaired. This technique is widely used in sensor arrays used in reflection seismology both on land and at sea.

The nine instruments give 36 different sensor separations. All the separations greater than 80 m are relative to OBS 1 which was separated from the rest of the array. The coherence for each pair of instruments for a particular window are shown in Figure 5.1. The plot is typical of the observations at this site. There are two bands of high coherence, below 0.4 Hz and between 0.8 and 3 Hz. Between those two bands there is a notch of lower coherence which widens with increasing separation.

The ambient seismic noise field derives its characteristics from three processes: the source of energy, the coupling of the energy into the elastic medium, and the propagation of energy in the elastic medium. It was shown in Chapter 4, through the theory of *Longuet-Higgins*, [1950] and *Hasselman* [1963], that under certain conditions, ocean surface swell can generate pressure fluctuations that reach the ocean floor unattenuated. It was also shown that the wavenumber of the resulting pressure fluctuations is limited to $|k| \leq \omega/\alpha$, where α is the acoustic velocity of water. The pressure fluctuations can couple into the ocean floor when their wavenumber is equal to that of the resonant modes in the elastic medium. However, the

excitation of high wavenumber (low velocity) seismic waves which are observed requires a different interaction which is not well understood. The last process, the propagation of energy in the elastic medium, will be the main focus of this chapter. The observed spatial coherence puts strong constraints on the nature of the seismic propagation between the coupling region and the receivers.

The coherence model is calculated from seismic modes in the sedimentary wave guide. Modal dispersion curves and synthetic seismograms were calculated using the normal mode formalism of *Woodhouse* [1980] as implemented by *Gomberg and Masters* [1988]. The mode spectra are calculated for a point tensor source in the lossy, elastic solid.

Measured seismic velocities are used in the input model. A 1984 experiment, undertaken at DSDP hole 469, studied the velocity structure of the sediments [*Sauter et al.*, 1986]. Explosives were detonated on the ocean floor so that significant energy would be coupled into the sediment waveguide. Dispersed Stoneley wave trains were generated and the observed dispersion pattern (Figure 5.2) was matched by iterative modeling with the synthetic seismogram program. The shape of the envelope of the wavetrains is strongly determined by the seismic Q structure of the waveguide. A Q model was determined by matching the synthetic seismograms to the data [*Sauter*, 1987]. The bulk of the energy of these dispersed wave trains propagated at velocities between 30 and 100 m s^{-1} and was quickly attenuated.

The observation that spectral energy from small explosions in shallow water produced Stoneley waves with a spectral peak in the 1-5 Hz range, led *Tuthill et al.*, [1981] to suggest that these waves were significant contributors to sea-floor noise. The CIRCUS experiment was designed to examine this assertion by attempting to observe natural occurrences of these very low velocity waves on the ocean floor.

The present study is concerned with frequencies extending much lower than were observed from the small explosions. The wavefunction at the lower frequencies extends into the basaltic crust so the sediment velocity model of *Sauter et al.* [1986] has been merged with a

crustal model which is representative of this region of the Pacific ocean crust [*Spudich and Orcutt*, 1980]. The velocity model is shown in Figure 5.3 and the associated phase and group dispersion curves in Figure 5.4. The dispersion model is plotted as a function of slowness because this parameter relates more directly to coherence length than does phase velocity. The phase velocity undergoes a change at 0.5 Hz as it makes the transition between Rayleigh waves and Stoneley waves. The Stoneley (or Scholte) waves are the continuation of Rayleigh waves to phase velocities lower than that of water, 1.5 km s^{-1} (c.f. *Tolstoy*, 1954). At these lower velocities, the vertical wavefunction is evanescent in the water, decaying upward away from the interface. The sea floor becomes the surface around which the waves are trapped.

Computation of plane wave synthetic seismograms alone makes no predictions for the coherence structure, however *Capon* [1973] showed that limits on coherence length could be imposed by an isotropic distribution of sources. For an isotropic distribution of plane wave sources, *Capon* [1973] showed by integrating the wavefield over azimuth that the coherence field is given by

$$K^2(\omega, r) = J_0^2(\omega p(\omega)r) \qquad (5.1)$$

where K^2 is the mean square coherence (MSC), J_0 is the zero-order Bessel function of the first kind, ω is the radial frequency, $p(\omega)$ is the frequency dependent phase slowness (the reciprocal of phase velocity), and r is the separation between sensors. The function $p(\omega)$ in the argument to the Bessel function is determined from the phase dispersion functions (Figure 5.4) A realization of Equation (5.1) for mode 0 is shown in Figure 5.5. The distance ordinate of the first zero of the Bessel function, by which coherence length is being defined, is directly related to the phase slowness at a given frequency. The transition from long to short coherence length occurs between 0.5 and 1 Hz and is associated with phase velocity changes in this frequency band.

In contrast to Figure 5.5, the observations (Figure 5.1) display multiple transitions from long to short coherence length, evidence that multiple modes are present. The mean squared coherence measures the proportion of energy that is organized. The total squared

coherence is the sum of the squared coherence from many sources in proportion to the power of each individual source. For the present model,

$$K^2(\omega) = \sum_{j=0}^{N} w_j(\omega) J_0^2 (\omega p_j(\omega)r)$$

(5.2)

where w_j is the proportional power in mode j,

$$w_j(\omega) = \frac{P_j(\omega)}{\sum_{i=0}^{N} P_i(\omega)}$$

and $P_j(\omega)$ is the power in mode j.

Power spectra for modes 0 through 3 are shown in Figure 5.6, computed for a distance of 15 km and a source depth of 1 m below the sea floor. The higher modes dominate at frequencies above 1 Hz. Figure 5.7 shows the coherence predicted from Equation (5.2) using the proportional power from Figure 5.6. Comparison of the coherence model (Figure 5.7) and the coherence observations (Figure 5.1) reveal a good match. The computation explains the band of high coherence between 0.8 and 3 Hz and the low coherence notch between 0.4 and 0.8 Hz.

To compute synthetic power spectra, a source distance and depth must be assumed. A distance of 15 km was chosen by trial and error to achieve the observed separation between the bands of high coherence. The the lower edge of the high frequency band in the coherence model (Figure 5.7) is controlled by the frequency at which the higher modes begin to dominate the fundamental mode. The eigenfunction for the mode 0 is strongest near the ocean floor. Mode 0 is thus excited strongly by a source near the surface, but since the Q of the upper sediments is low, mode 0 is attenuated more strongly than are the higher modes. This is illustrated by four examples in Figure 5.8 for different ranges and source depths. For a shallow (1 m) source the dependence of mode attenuation on distance is strong. For a deeper (100 m) source the mode attenuation with distance is less clear. In Figure 5.9 the frequency at which the higher modes exceed the fundamental mode is plotted as a function of source distance and depth. For a deeper source, the fundamental mode is not excited as strongly and there is less dependence

a deeper source, the fundamental mode is not excited as strongly and there is less dependence on distance. The source moment tensor may also affect the excitation of modes. Since we have insufficient data to determine such a tensor a diagonal tensor has been used for these calculation.

A physical interpretation can be associated with the 15 km distance derived from the coherence model. Figure 5.10 shows a bathymetric map for the immediate vicinity of the experiment, with a circle marking a radius of 15 km from the array site. Significant topographic features are located roughly at this distance, in particular the Patton escarpment to the east and a seamount to the northwest. A likely explanation is that inhomogeneities in the boundaries can scatter incident waves into the surficial layers. *Levander and Hill* [1985] showed by numerical modeling how high wave number signals generated at depth (or analogously at the water surface) can be coupled into high wave number (slowly propagating) signals in the ocean bottom. *Dougherty and Stephen* [1988] demonstrated how volume heterogeneity could convert incident body waves into surface waves. While we cannot make a definitive distinction here between these two possibilities, the bathymetric data available to us most closely resembles the assumptions made by *Levander and Hill* [1985].

Low coherence near 0.6 Hz in this model requires that the coherence between the separate modes is small. All modes are excited by the same source but because of the large variation in phase velocity, different frequencies reaching the receiver at a given time were generated at different times. As an extreme example, mode 3 at 1 Hz will propagate 15 km in 10 s, while mode 0 at 1 Hz requires 150 s. The time difference is long compared to the correlation time of ocean swell. The expected time separation between modes exceeds the length of the discrete Fourier transform windows and the calculated coherence is therefore reduced (c.f. *Jenkins and Watts*, 1968, p. 399).

The coherence model differs from the observed coherence in the following respects. The low coherence notch is not nearly as deep in the data and the band of coherence near 1 Hz

is wider in the data, which suggests that the coherence lengths for the model are too low. A more general beam pattern than for the isotropic case, is the form $\cos^\mu(\theta/2)$ [*Longuet-Higgins et al.*, 1963; Webb, 1986]. An isotropic wave field is implied by $\mu = 0$, and a single plane wave by $\mu = \infty$. Coherence functions are shown in Figure 5.11 for a variety of beam parameters μ. The coherence length increases for increasing directional confinement, suggesting that a narrower beam can improve the fit. The coherence model of Figure 5.7 is recalculated for $\mu = 4$ and shown in Figure 5.12 and shows a better match to the data. The improvement with a narrower source beam is not surprising since the noise is probably associated with the dominant bathymetric feature, which is the Patton escarpment to the northeast.

The dimension of the array is very small compared to the distance to the source. If the array had been much more extensive, so that we could decompose the wavefield by mode and azimuth, we could extract more information about the scattering sources and mechanisms. In the study of earthquakes, the global array of low frequency seismic stations allows reconstruction of the time history of each component of the tensor source [*Dziewonski et al.*, 1987; *Riedesel and Jordan*, 1989; *Gilbert*, 1971]. In principle the only difficulty barring us from doing this at smaller scale on the sea floor is the matter of achieving adequate spatial sampling to decompose the wavefield.

In summary, measurement with a 150 m aperture array on the seafloor has placed significant constraints on the coherence of ambient noise between 0.05 and 10 Hz. The observed pattern of coherence is well modeled by an isotropic or broad beam distribution of low order Raleigh/Stoneley waves. The velocity and attenuation structure of the Rayleigh wave guide affects the coherence structure by controlling the relative power of the different modes as a function of frequency and distance from the source. The coherence field at this site is profoundly affected by the low velocity sediments that cover the basin. In the framework of this model, the band of high coherence length between 0.8 and 2 Hz suggests that the seismic waves

which comprise the noise are excited at a distance of 15 to 20 km or alternatively at a depth greater than 100 m below the ocean floor. Either of these possibilities imply that the energy which is generated at the ocean surface is scattered into the sedimentary layer at the boundaries of the basin. The good fit of this model to the observed coherence indicates that at this site at least, scattered energy is a more important source of seismic noise at the ocean floor than is direct radiation from the sea surface above the sensor.

In contrast with the results presented here, the physics by which noise is coupled into the sea floor in shallow water is quite different. There *Schmidt and Kuperman* [1988] have demonstrated that it occurs by direct coupling of sea-surface noise into the waveguide through the evanescent part of the wave function. Energy in the water column has a much stronger contribution to noise levels measured on the deep ocean floor.

Figure 5.1. Spatial coherence measured from record 229. The horizontal axis is frequency from 0.03 to 10 Hz, and the vertical axis is separation between sensors from 0 to 156 m. Color is proportional to mean squared coherence.

Coherence (Window 229)
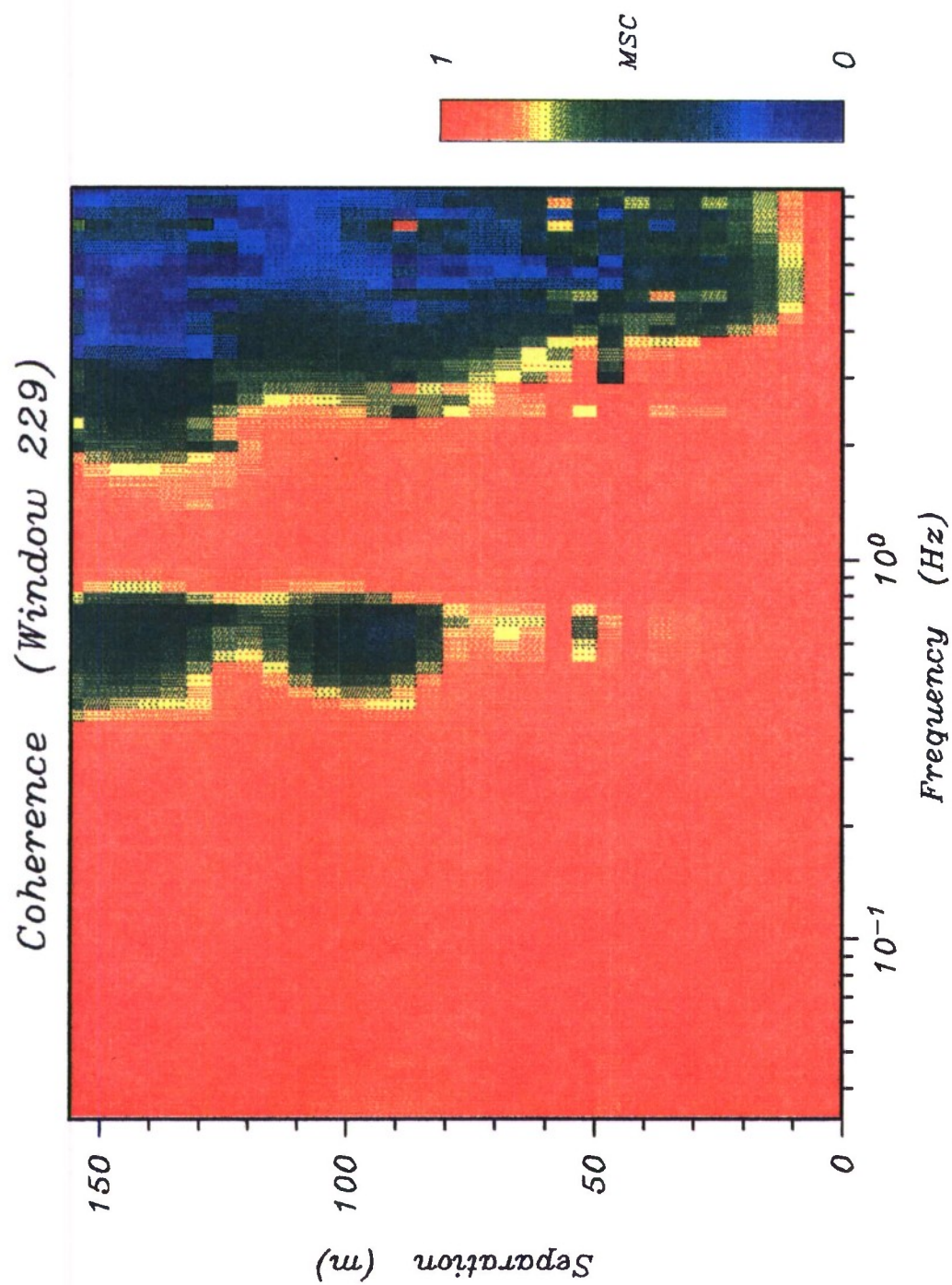
Figure 5.2. Stoneley wave recorded from an ocean floor shot. The dispersion analysis below the time series shows the variation in frequency with time relative to the source, or equivalently, to group slowness.

Instrument 6   Event 11   Component 1
Range   0.939 km

Time   (s)

Group Slowness   (s km⁻¹)
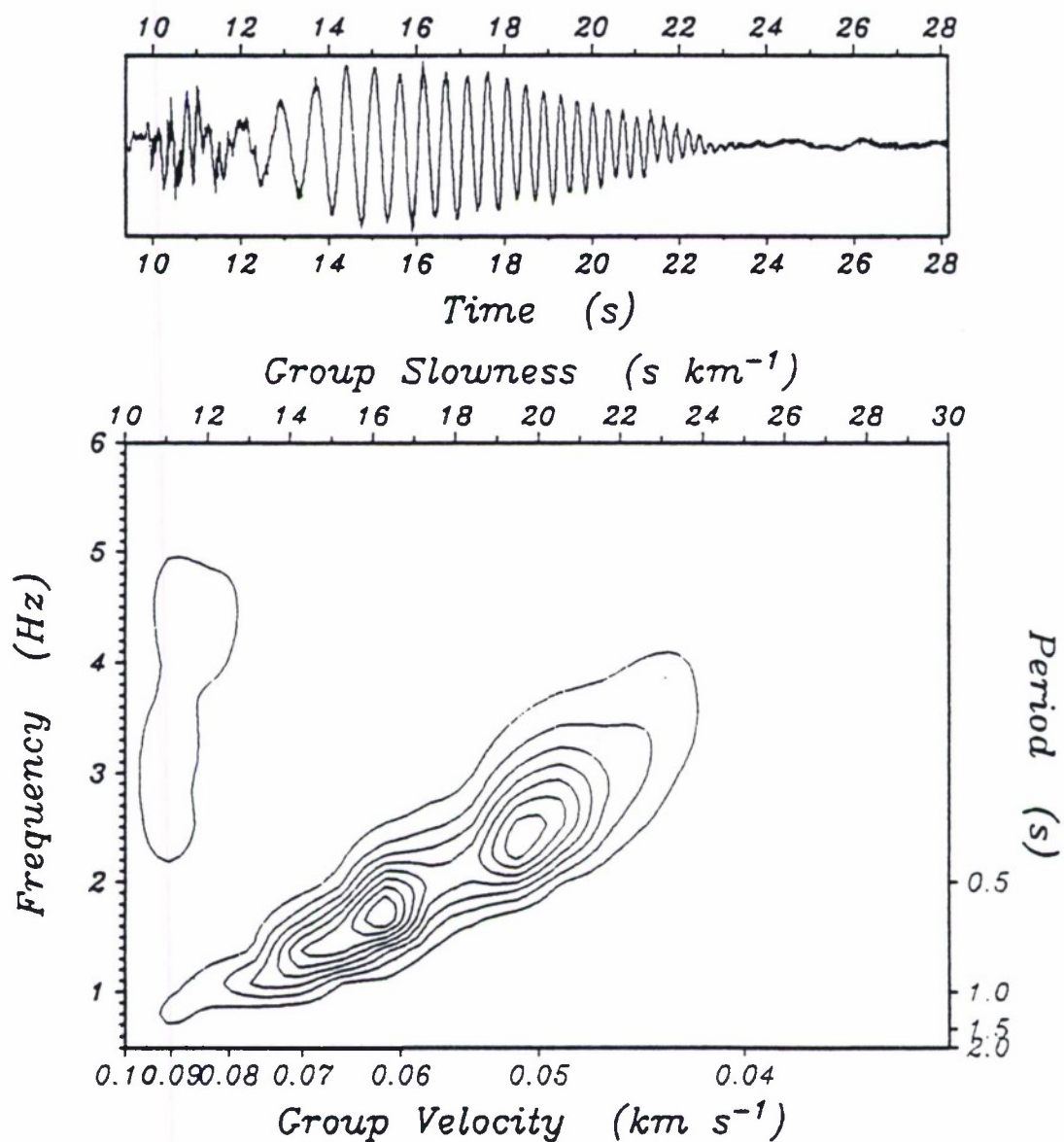
AMPLITUDE

Contour interval   2.0e-03

Filter parameters: Alpha 20.00,   Relative bandwidth

Figure 5.3. Velocity model for the CIRCUS array site. The velocities in the upper sediments are derived from the dispersion analysis of bottom shots. The crustal velocities are from *Spudich and Orcutt* [1980].
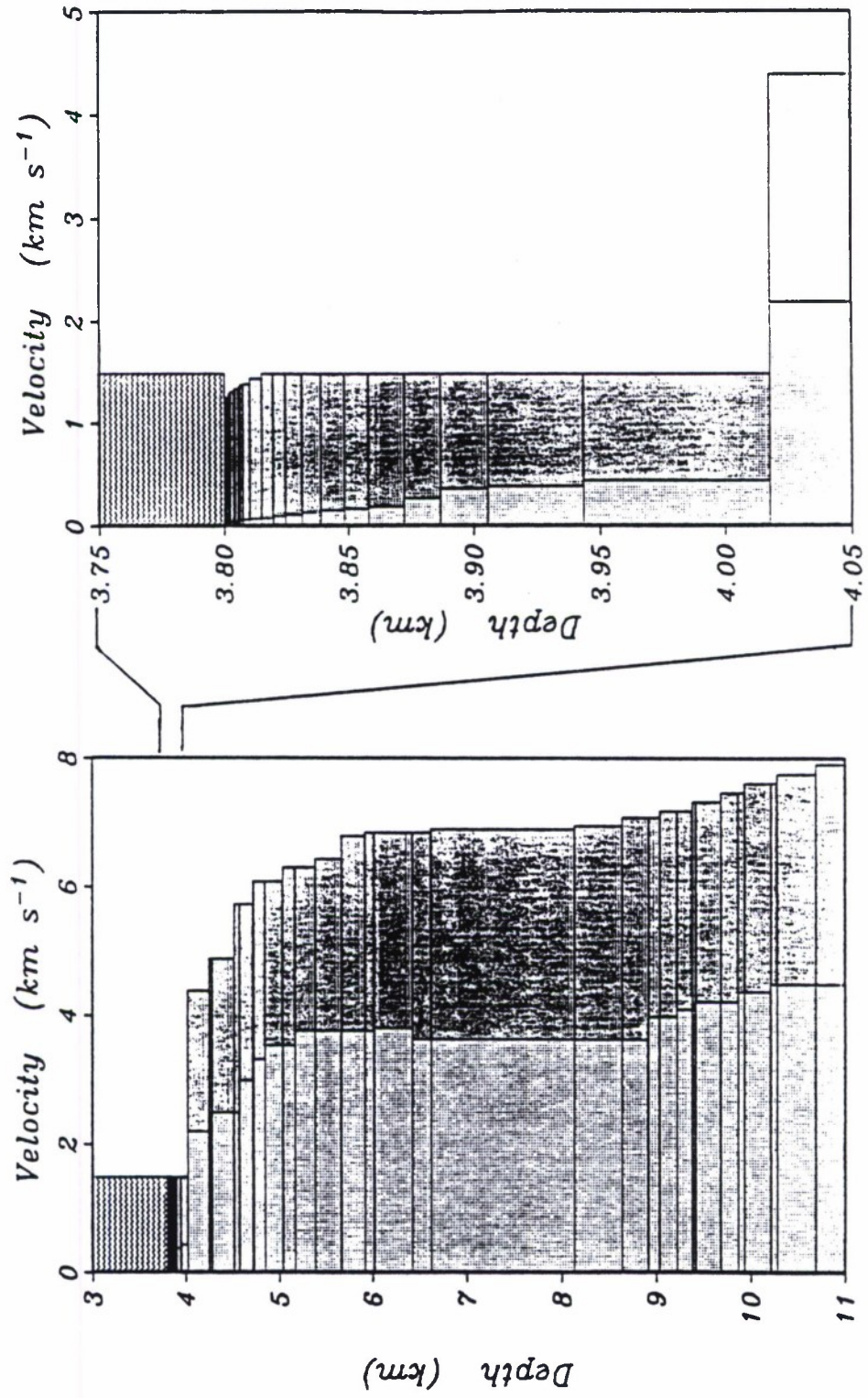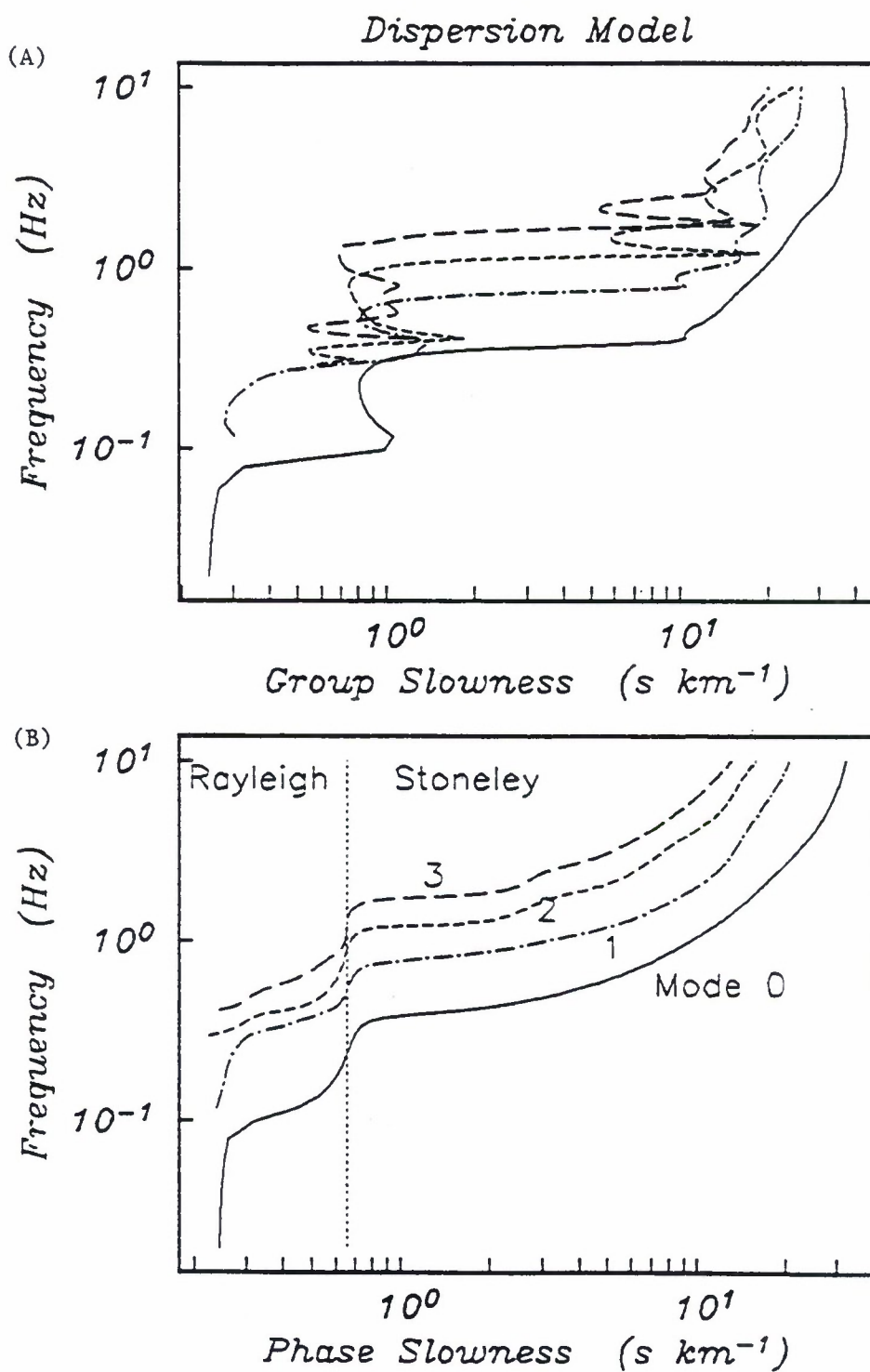
Figure 5.4. Synthetic dispersion curves. The line style is consistent for each mode in both displays. a) Group slowness, b) Phase slowness.

Figure 5.5. Synthetic spatial coherence calculated from the mode 0 dispersion curve. See Figure 5.1 for description of the plot.
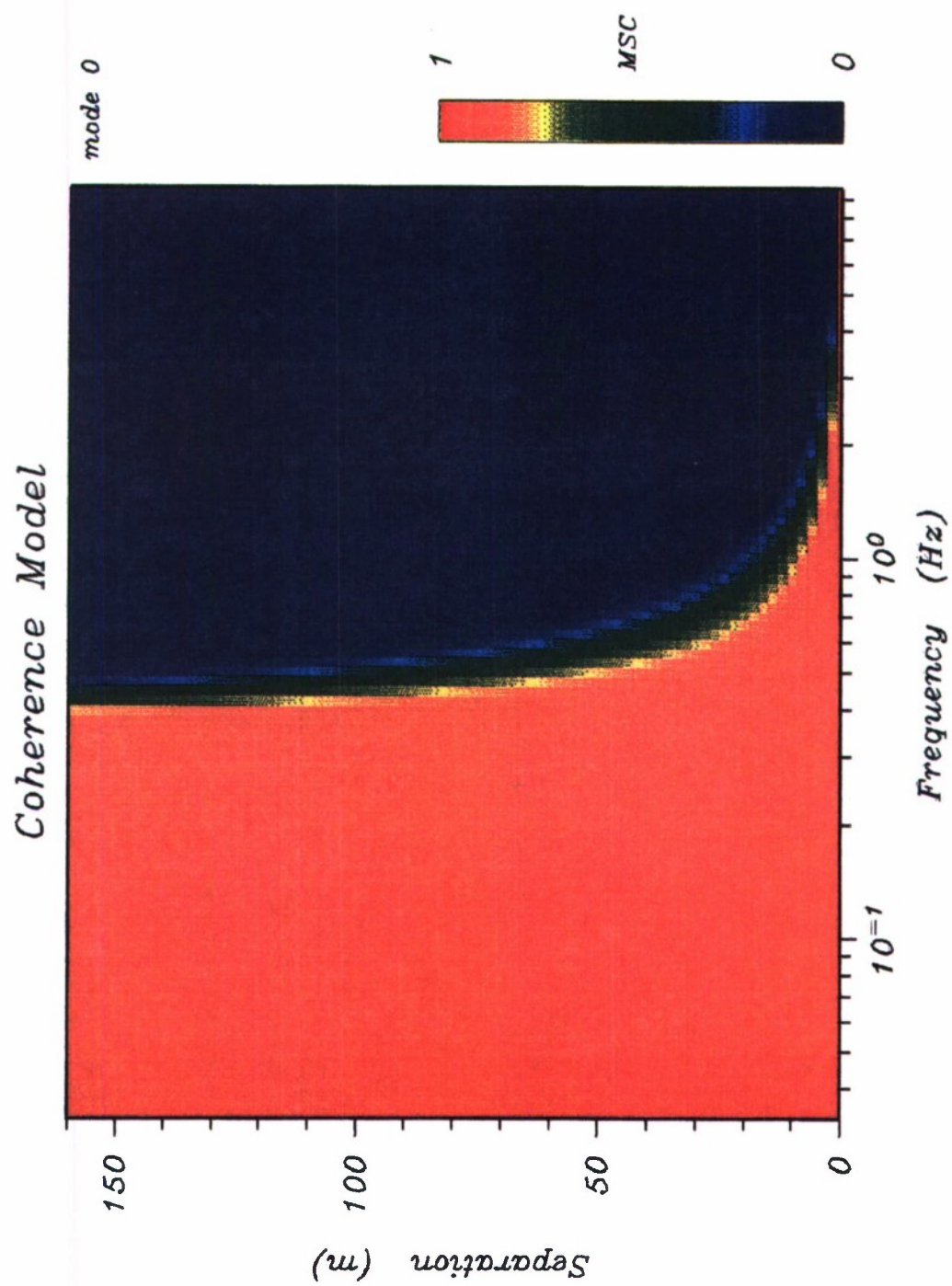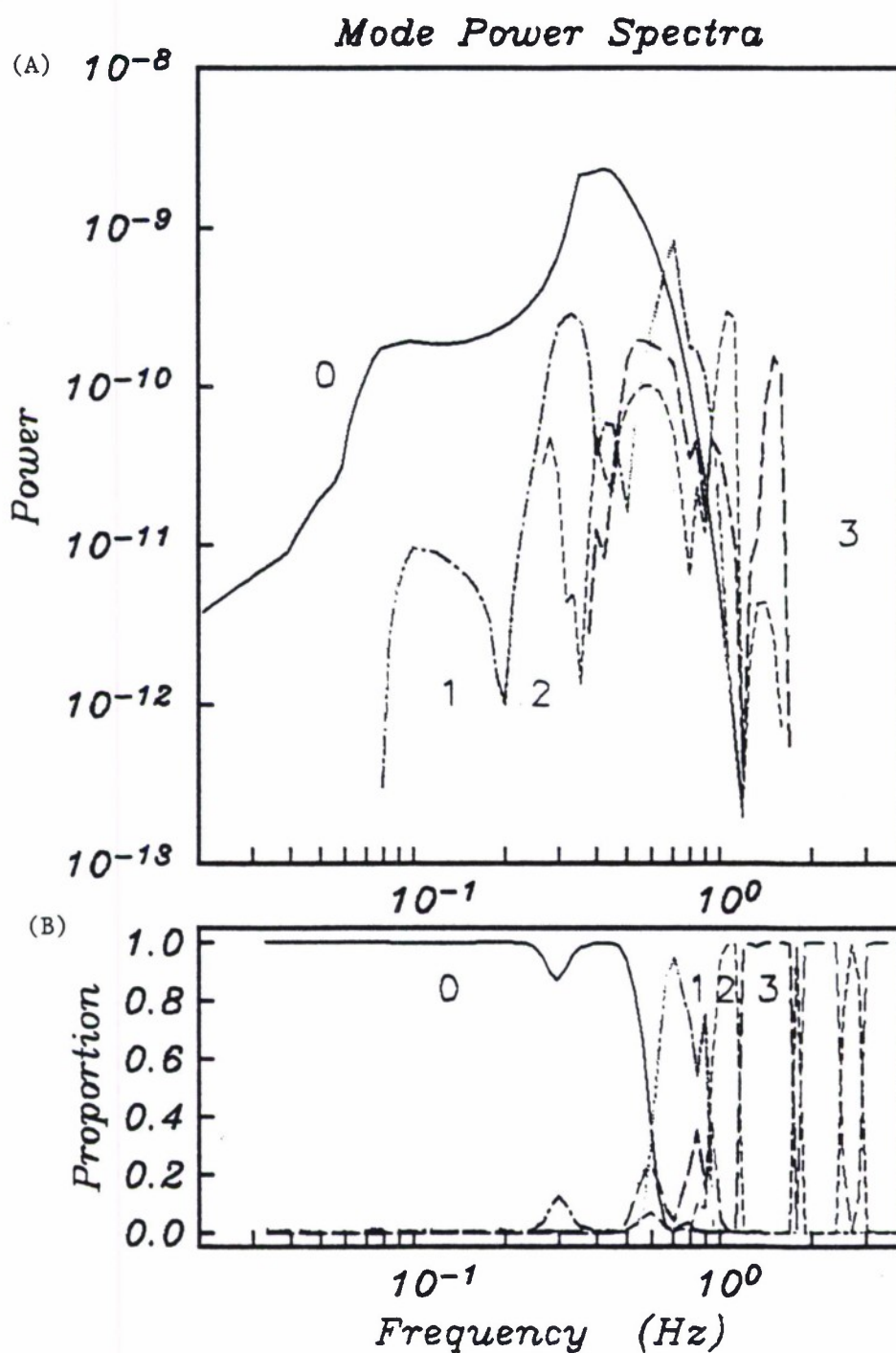
Coherence Model

Figure 5.6. Synthetic power spectra and relative power for modes 0 through 3. The line styles are the same as in Figure 5.4. a) Power spectra, b) Proportion of each mode to total power.

Figure 5.7. Synthetic spatial coherence for modes 0 through 3 and an isotropic source distribution.

Coherence Model ($\mu = 0$)

modes 0–3
distance = 15

MSC

1

0

Frequency (Hz)

10^{-1}

10^0

Separation (m)

0

50

100

150
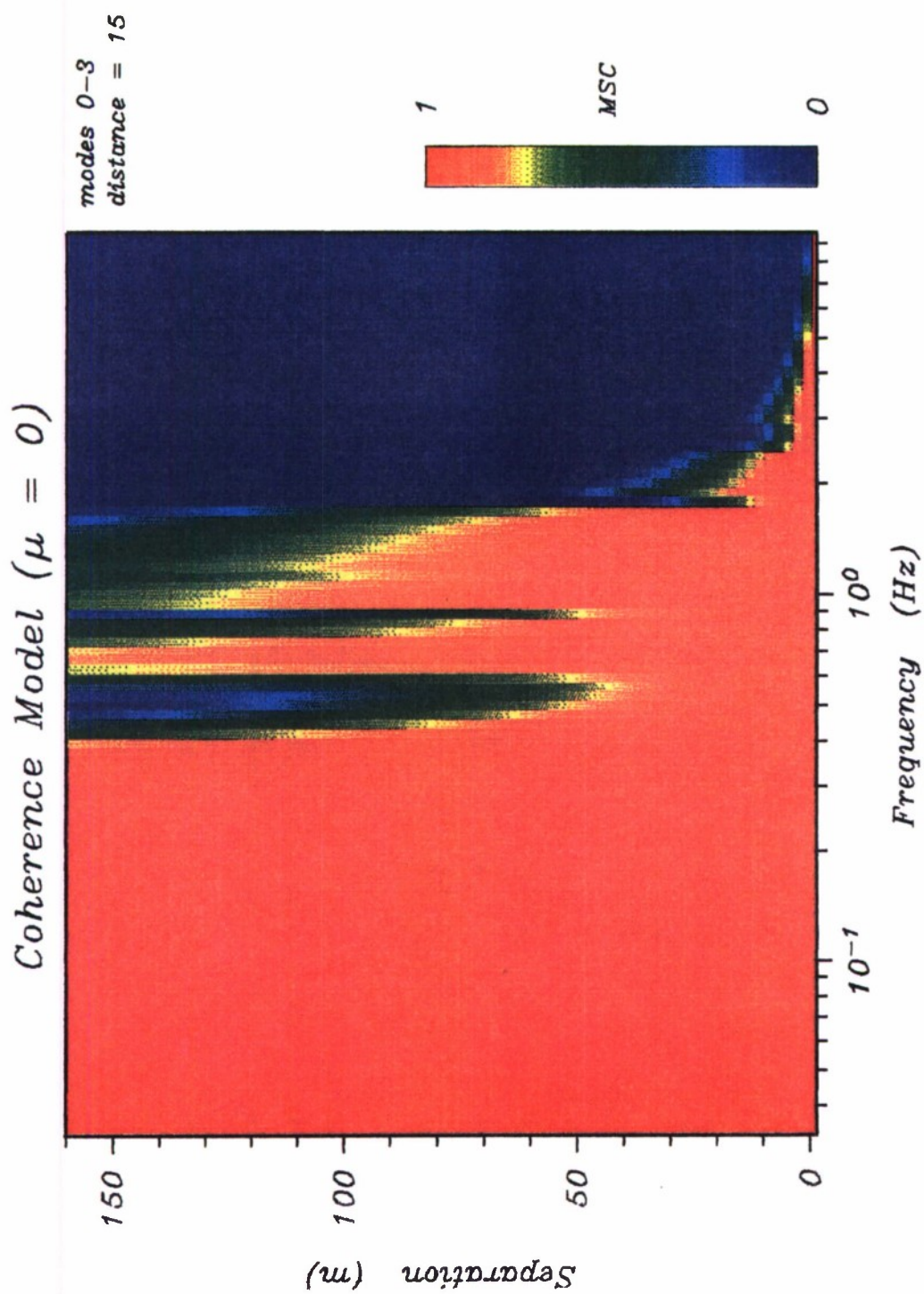
Figure 5.8. Examples of mode spectra for different source depth and distances. a) Source depth = 1 m, distance = 10 km, b) Source depth = 1 m, distance = 100 km, c) Source depth = 100 m, distance = 10 km, c) Source depth = 100 m, distance = 100 km.

Effect of Source Depth and Distance on Mode Power Partitioning
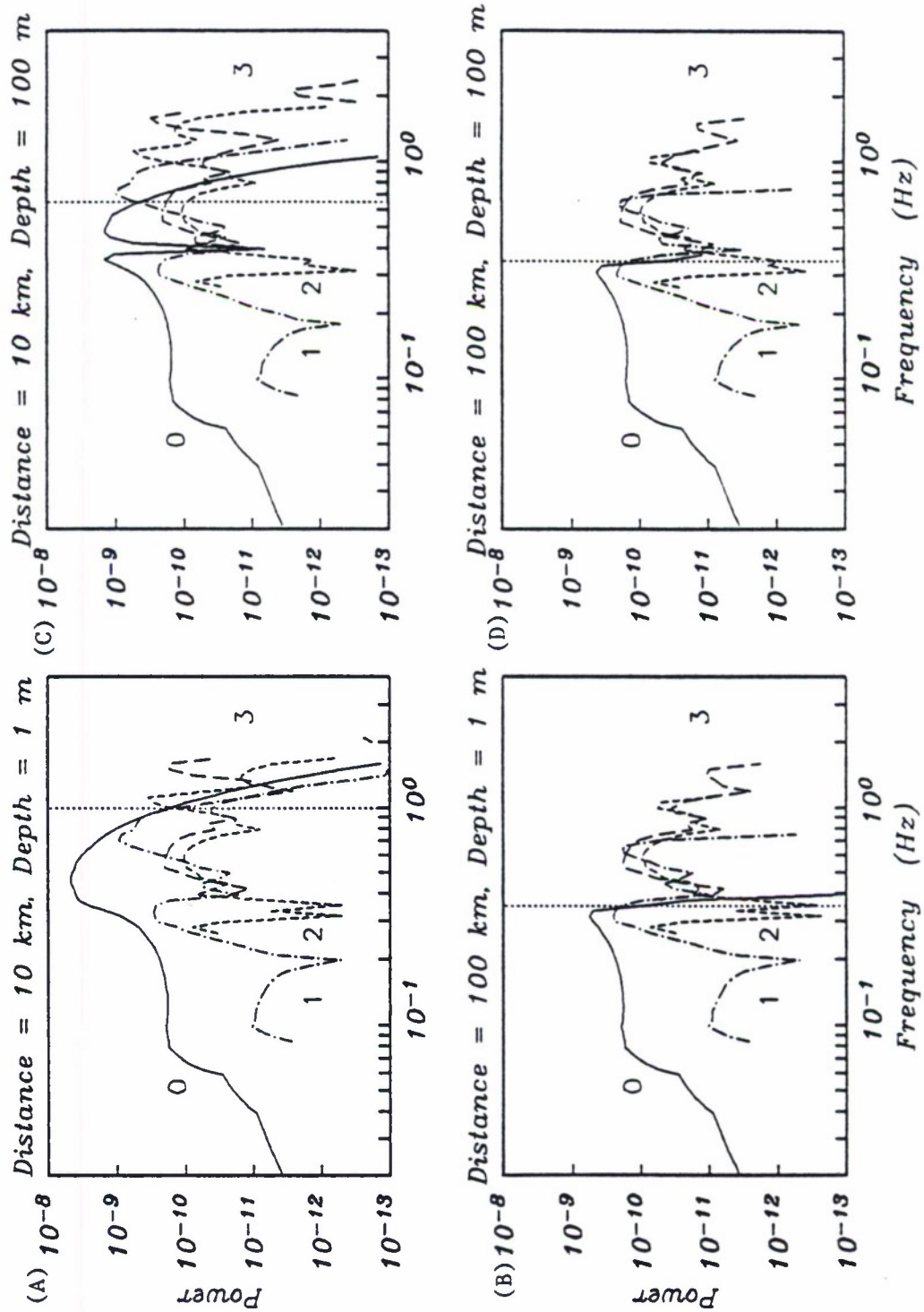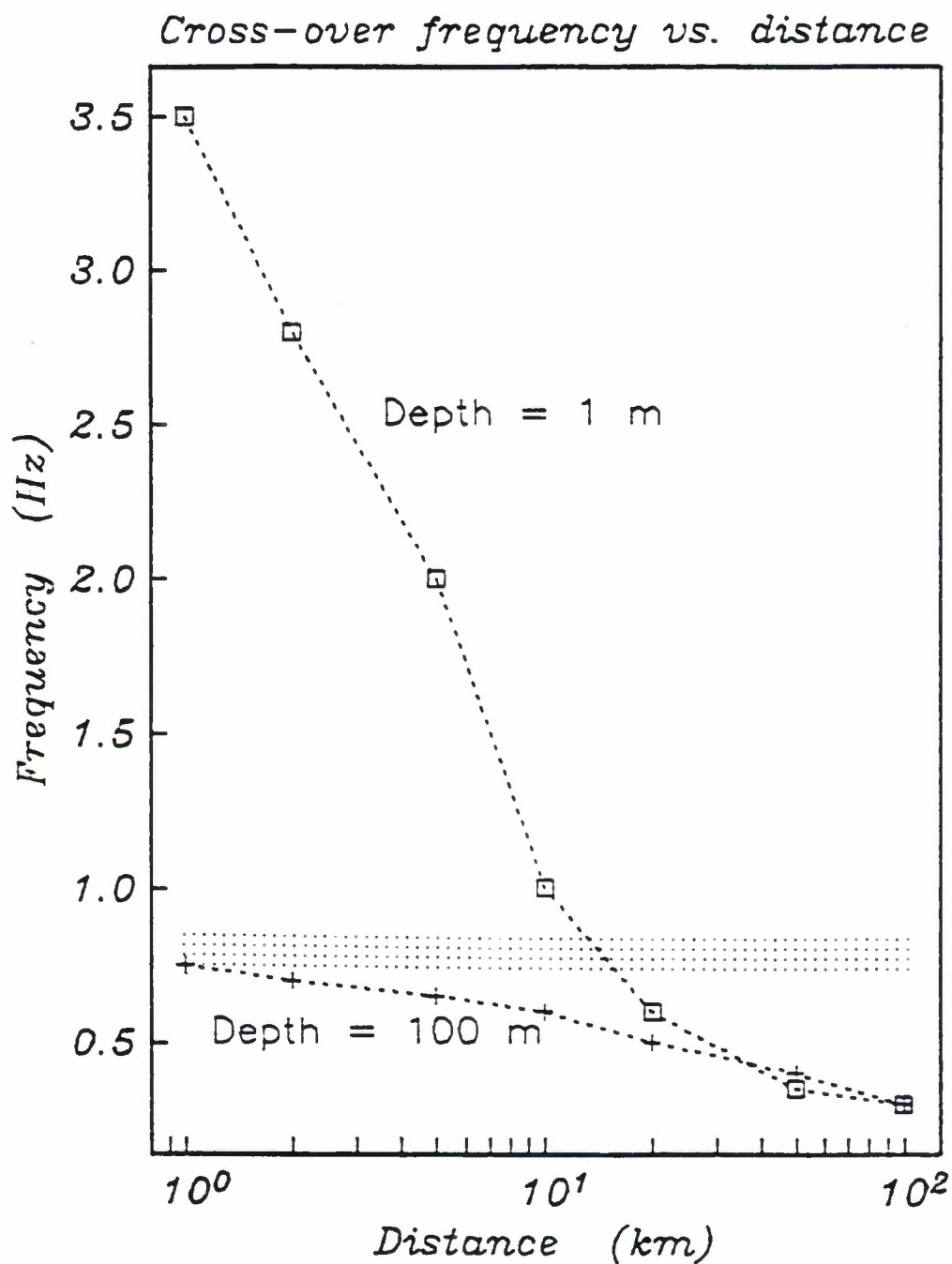
Figure 5.9. Frequency at which one of the higher modes becomes dominant over the fundamental mode versus source distance at source depth of 10 and 100 m.

Figure 5.10. Bathymetry of the CIRCUS array vicinity. The contour interval is 100 m.
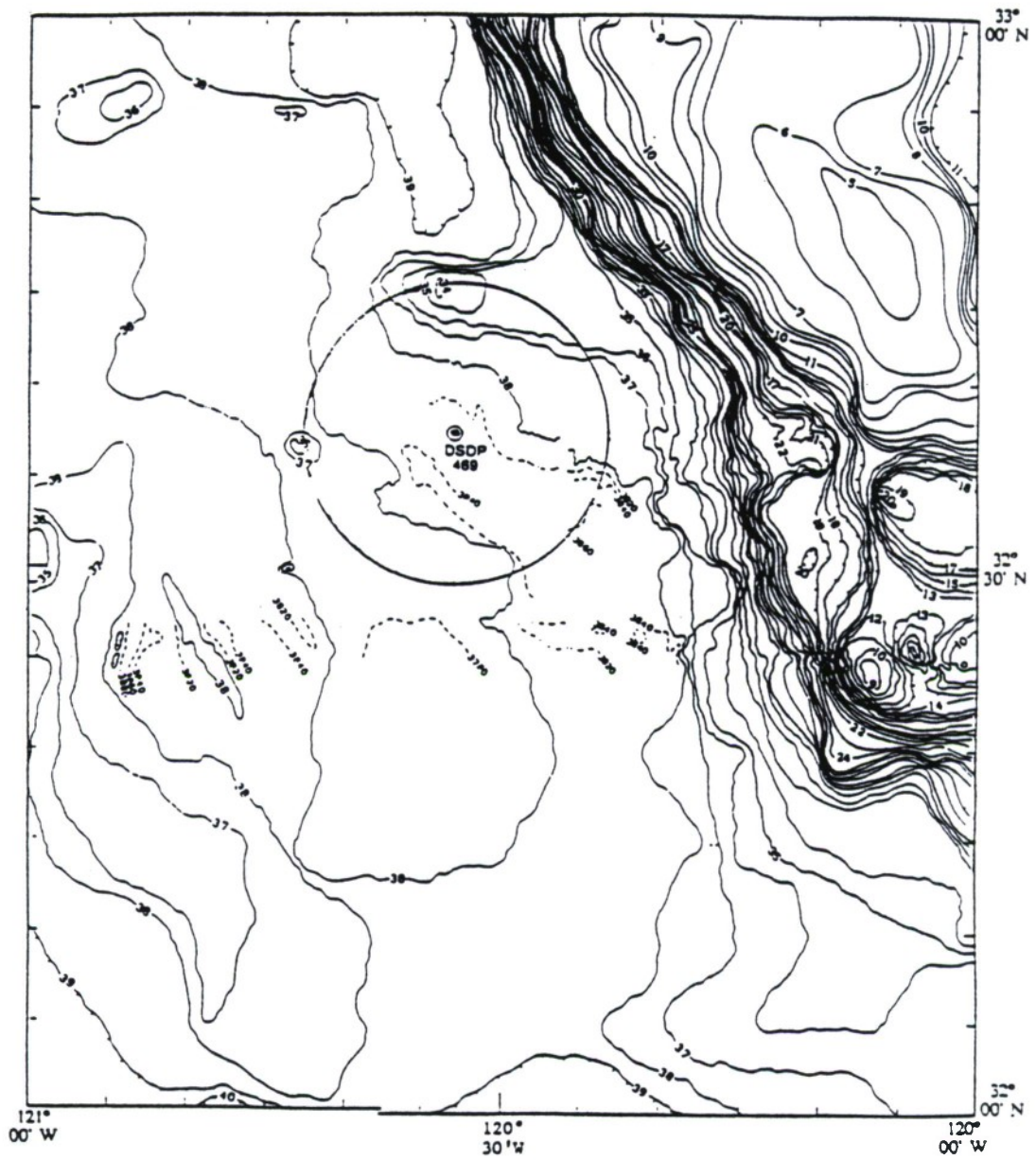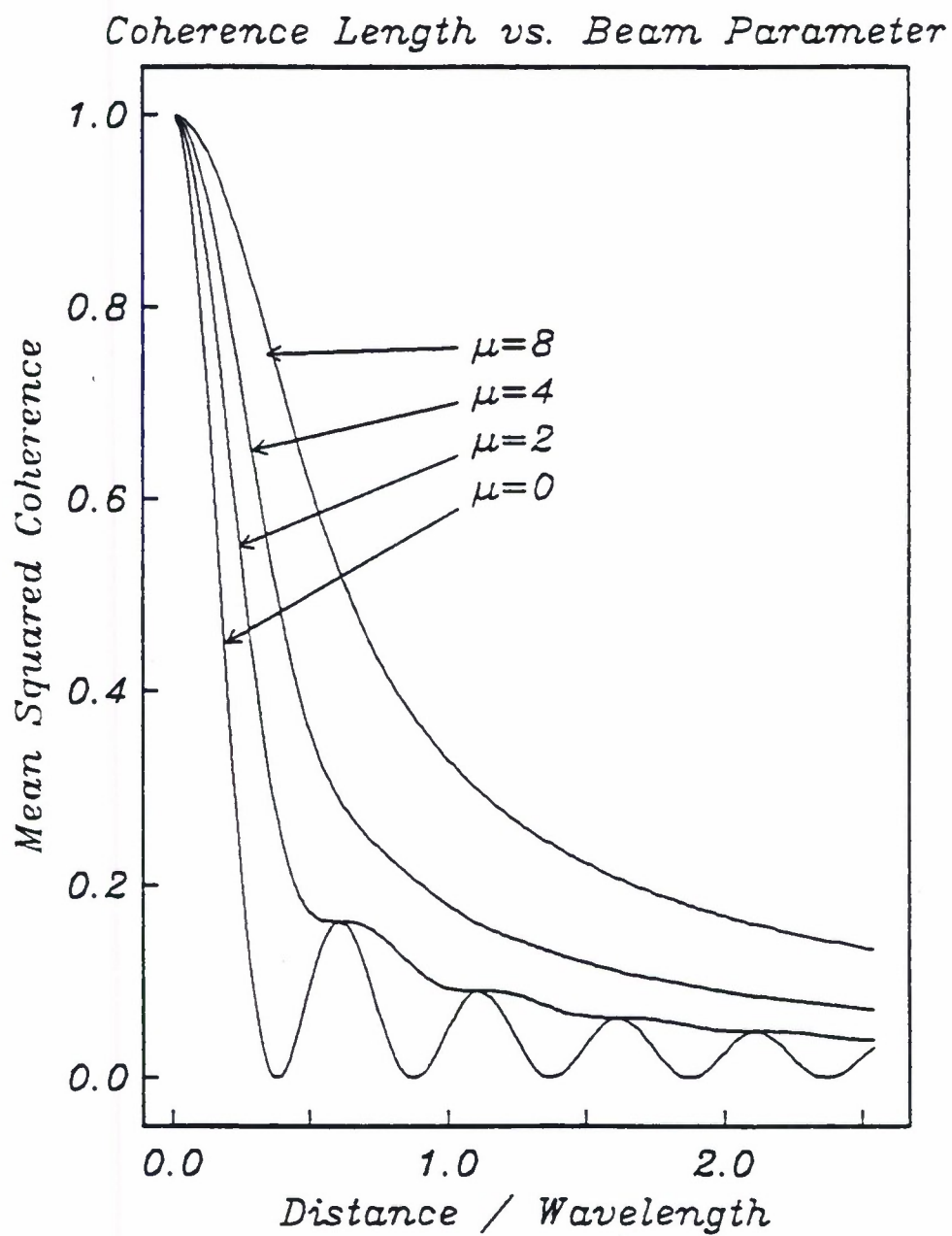
Figure 5.11. Coherence versus distance for four beam parameters.

Figure 5.12. Synthetic spatial coherence for modes 0 through 3 and a distributed source predominantly on one side of the array.

Coherence Model ($\mu = 4$)

modes 0-3
distance = 15
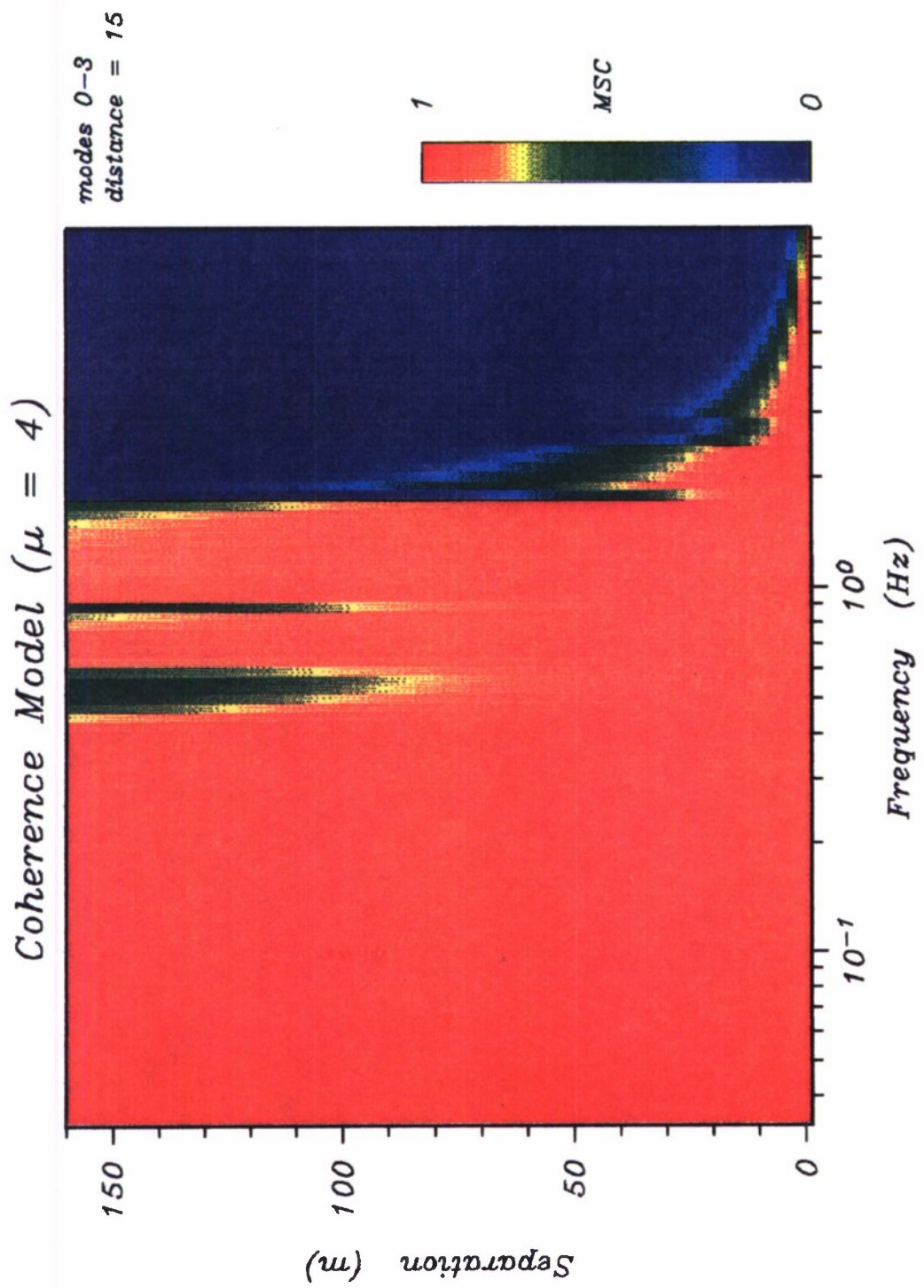
CHAPTER 6

BEAMFORMING RESULTS

Sensors are placed in arrays for two reasons, to enhance signal to noise ratio, and to make direct measurement of phase velocity, which can be converted to bearing and velocity estimates. Arrays have been used very successfully in the disciplines of radio science and underwater acoustics to determine the bearing of signal sources. In both those fields, the problem is simplified because acoustic waves in water and electromagnetic waves propagate at approximately a single, well known velocity. Apparent phase velocity across the array is thus mapped uniquely into angle of incidence. Seismic waves, on the other hand, travel at a range of velocities between 40 m s^{-1} in water-saturated muds on the ocean floor, to 13 km s^{-1} in the lower mantle. Some additional knowledge of the propagation path is usually required in the seismic case. Exploration of Earth structure, of the type done for petroleum exploration routinely uses linear arrays of many elements, both for estimating apparent phase velocity through moveout determination, and for enhancing coherent arrivals through stacking. The technique has not been used as commonly for global seismology and for natural seismic sources because of the more expensive sensors required for those applications. There are a few examples of large arrays used for measuring teleseismic signals, the most notable example is LASA, the Large Aperture Seismic Array [*Capon et al.*, 1969].

Data from LASA had a substantial impact on the study of microseisms [*Haubrich and McCamy*, 1969; *LaCoss et al.*, 1969]. It was determined that background noise propagates at 3.5 km s^{-1} in the frequency range of 0.03 and 0.05 Hz. At these frequencies, this velocity can be identified with the fundamental Rayleigh mode for a continental path. The apparent direction to the source of this energy was from the coast nearest to oceanic storms, thus corroborating the hypothesis that ocean waves are the primary source of microseisms. In the frequency range of 0.3 to 0.5 Hz, the propagation was also found to be 3.5 km s^{-1}, corresponding to higher mode

Rayleigh waves. At frequencies above 3 Hz, the velocity was measured at 13 km s^{-1} and was associated with P-waves propagating in the lower mantle.

Few attempts at beamforming on the deep ocean floor have been made. The CIRCUS was the first that permitted coherent processing of signals on more than two sensors. The CIRCUS array was of a more limited nature than typical land arrays. Ocean bottom seismometers are expensive and few in number so it was necessary to limit the wavenumber bandwidth of the array to between 6 and 125 cycles km^{-1}. The width of the central lobe of the array response is 10 km^{-1}, or $10/2\pi f$ s km^{-1} in terms of slowness (reciprocal velocity). Figure 6.1 shows how this resolution limit relates to expected phase velocities from the dispersion curves. Measurements below the the dashed line cannot be resolved with conventional beamforming from a slowness of zero. Some improvement in resolution can be achieved with Capon's method but the array can effectively measure phase velocity only above 0.5 Hz. The uncertainty in relative timing of the OBS', which was discussed in Chapter 2, will further limit the resolution of beamforming.

Another limitation is that the CIRCUS array was never effectively calibrated. The experiment plans called for a series of shots to be detonated in the water at a variety of azimuths around the array. However the OBS clocks and the clock by which the shooting was timed were offset from each other by one minute, so the first arrivals from the shots were not recorded by the OBS. The deployment ships provide a less satisfactory alternative signal to be used for array calibration. Rotating machinery in the propulsion systems generates spectral lines in the water (Figure 6.2). Impulsive sources are more desirable because timing and position errors can be seen directly on each sensors' record as time offsets. With continuous wave sources such errors are only observable as phase delay, and there is an inherent ambiguity, which becomes harder to overcome at the higher frequencies associated with ship noise. There were two ships present during the first two days of the deployment, the *R/V Melville* and the *USNS Narragansett*. They have radically different propulsion systems and so would be expected to have distin-

guishable acoustic signatures. It has however, proved difficult to assign spectral lines to one ship or the other. There is usually no simple relationship between between spectral line amplitude and ship distance. Beamforming has provide unambiguous answers for only two spectral lines, examples of which are shown in Figures 6.3 and 6.4. In these figures, the wavenumber axes have been scaled by the analysis frequency so that the units become those of slowness. The vector fro the origin to any point represents propagation in that direction with slowness proportional to the length of the vector. The dashed circle centered at the origin represents the acoustic slowness of water $1/\alpha$. A signal propagating horizontally horizontally in the water will be indicated by wavenumber analysis as a point on this circle. A signal propagating vertically will appear at the center. The color at each point represents the power level. The 5.75 Hz line has been identified with the *R/V Melville* while it is holding station nearly above the array (Figure 6.3). The line is absent when the ship is underway or at some distance. The 19.5 and 19.6 Hz lines have been identified with a continuous wave source that was towed behind the *USNS Narragansett* (Figure 6.4). However, in the figure it is evident that at this frequency there is also a source with the bearing corresponding to the *R/V Melville*. Figure 6.4 show a misfit of the predicted position of 0.2 s km^{-1}. In many other cases, beamforming does not identify a bearing that corresponds to either one of the ship positions. It is unknown at this time whether the inconsistent performance of the wavenumber processing is due to errors in the data such as timing errors or position errors, or whether it is due to low stability of the spectral estimates.

Keeping in mind the possible inaccuracies in the wavenumber estimates, a survey of the early part of the experiment follows. The error in the clocks is expected to get worse with time, and indeed more scatter in the estimated velocities is evident in the later records. Figures 6.5 through 6.7 show wavenumber spectra for window 219 for frequencies of 0.25, 0.75, and 1.25 Hz. The spectra are computed by Capon's method with segment averaged Fourier transforms with a time-bandwidth product of 25. Energy propagating to the southwest at each frequency. A slowly propagating wave is detected at 0.75 Hz, but otherwise the observed slowness is between 0.5 and 1.0 s km^{-1}. As expected, examination of other records shows some

variability, but slow propagation velocity is commonly observed at frequencies between 0.25 and 0.75 Hz. Figure 6.8 is a summary of all velocities measured for the first 20 records between 0.125 and 3 Hz. Also shown in the figure are the dispersion curves from *Sauter et al.* [1986] which were used in Chapter 5 to compute synthetic spectra. The dispersion curves are emphasized where the individual mode is dominant (compare with Figure 5.4). There is rough agreement with the expected velocities so the results from the beamforming analysis are consistent with the results derived from modeling the spatial coherence. The distribution of energy among the modes is evident. As frequency increases, the phase slowness increases as it follows a given mode's dispersion curve, then decreases when it jumps to the next higher mode as it becomes predominant. The scatter of the points is relatively large. However, comparison with the results of *Haubrich and McCamy* [1969] (see their Figure 9), reveals that even at LASA, under more ideal circumstances, the scatter is substantial.

The direction of propagation is summarized in Figure 6.9. The histogram shows a preponderance of energy propagating to the southwest. This is consistent with a source of energy at the edge of the sedimentary basin, which is closest to the array site towards the northeast, at the base of the Patton escarpment.

Clear from Figures 6.8 and 6.1 is that the target wavenumber band (and thus slowness) of the CIRCUS array was too low. It had been presumed from observation of the close range bottom shots, that the predominant energy would be on the very slow part of the dispersion curve, above 10 s km^{-1}. The discovery that the energy is coupled into the sediment wave guide at a distance of several kilometers means that these very slow waves are attenuated below detection by the time they reach the array. At the frequency at which the fundamental mode would be propagating at 10 to 30 s km^{-1}, the faster overtones are detected instead.

The most important result from this study is that there is significant energy propagating at the ocean bottom at low velocity, especially at frequencies between 0.5 and 3 Hz. The source of ambient noise energy is pressure fluctuations at the ocean surface. It has been shown

that this type of source cannot excite modes in the ocean bottom at phase slowness greater than $1/\alpha = 0.66$ s km^{-1}. The fact that such low velocities are indeed observed indicates that some form of energy scattering is taking place. The nature of the scattering is beyond the scope of this study, but a reasonable conclusion is that it occurs where the sediment bed pinches out and there is a sloping boundary between the sediments and the hard rock.

IMPLICATIONS FOR FUTURE WORK

The decomposition of the ambient noise field into seismic modes has important implications for sub-bottom sensor data. The justification given for making the effort to deploy sensors in a borehole is that there is a potential for improving the signal to noise ratio of measured teleseismic signals. The degree to which this is true is a consequence of the depth dependence of the ambient noise compared to that of the desired signal. Body waves are often of interest, especially at higher frequencies, and they do not depend on distance from the seafloor directly. Ambient noise is presumed to consist of interface waves, an assertion supported by this study. The depth dependence of interface waves can be determined from the mode structure. At this site, the fundamental Rayleigh mode is the primary contributor to noise below 0.8 Hz. Above that, and up to about 5 Hz, higher Rayleigh modes have higher amplitudes. The higher modes decay less rapidly with depth than the fundamental so it is important to consider their effects when considering the question of sensor depth.

An alternative to placing sensors in a borehole, is to use an array of sensors to enhance the signal to noise ratio. Knowledge of the coherence length of the ambient noise at different frequencies makes possible the design of optimum array configurations to maximize array gain. The present study showed that the minimum coherence length in the frequencies observed is 50 m, and although not directly observed, suggests that the upper limit is on the order of one kilometer. Further studies should be designed to for these greater length scales. The predetermined recording schedule for the CIRCUS deployment was not serendipitous enough to acquire a teleseismic event. Further studies should include event triggering so that

the gain for interesting seismic signals can be measured directly.

Finally, the CIRCUS array, being in the horizontal plane, made no direct measurements of vertical noise coherence. The present study has successfully modeled ambient noise as horizontally propagating trapped modes, suggesting that these predominate over acoustic energy in the water column. Future work should test this result more directly by incorporating a vertical array.
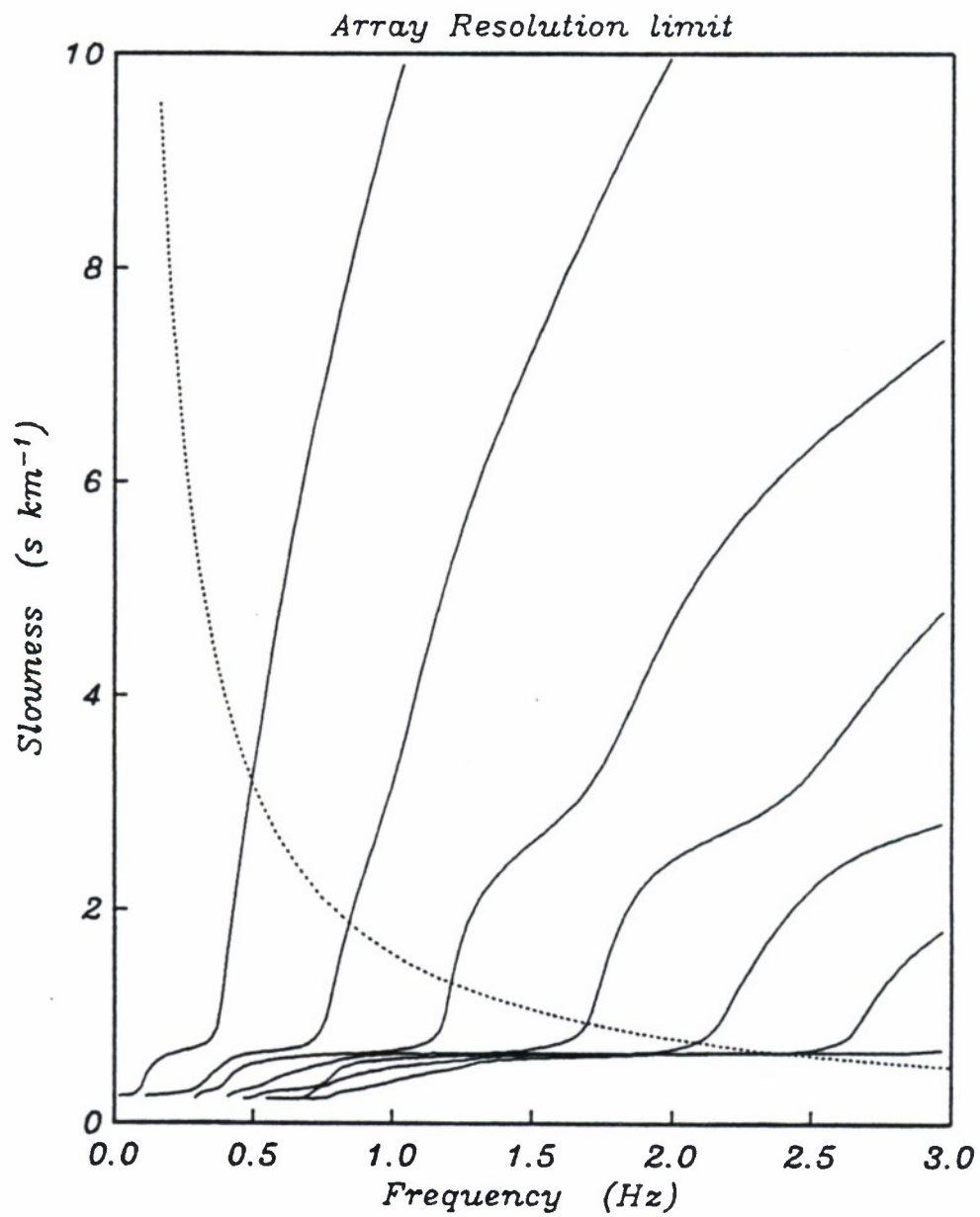
Figure 6.1. CIRCUS array resolution limit compared to expected seismic dispersion curves.
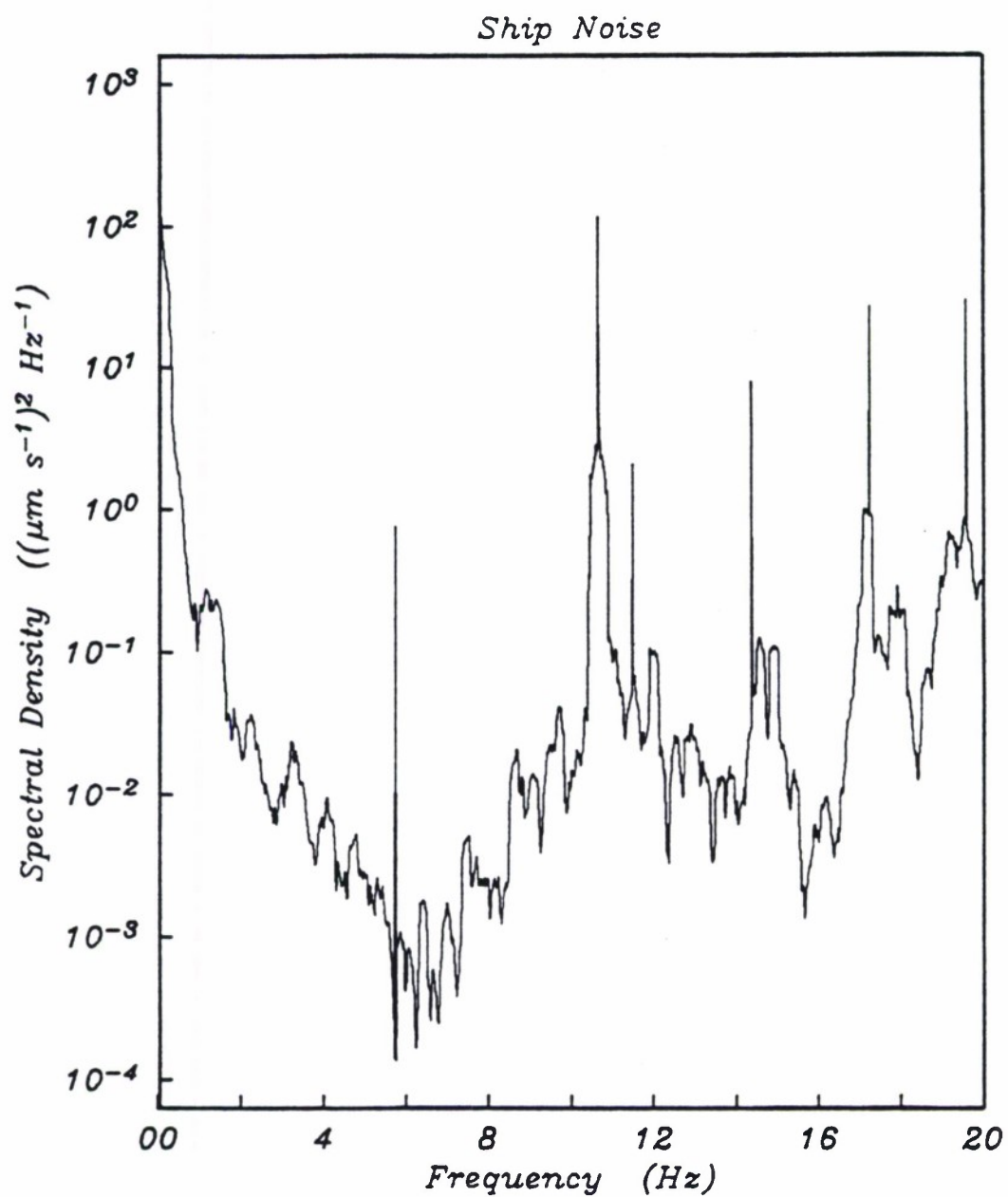
Figure 6.2. Noise spectrum while the R/I *Melville* and *USNS Narragansett* are on site. Spectral lines are resolved with multiple taper harmonic analysis.
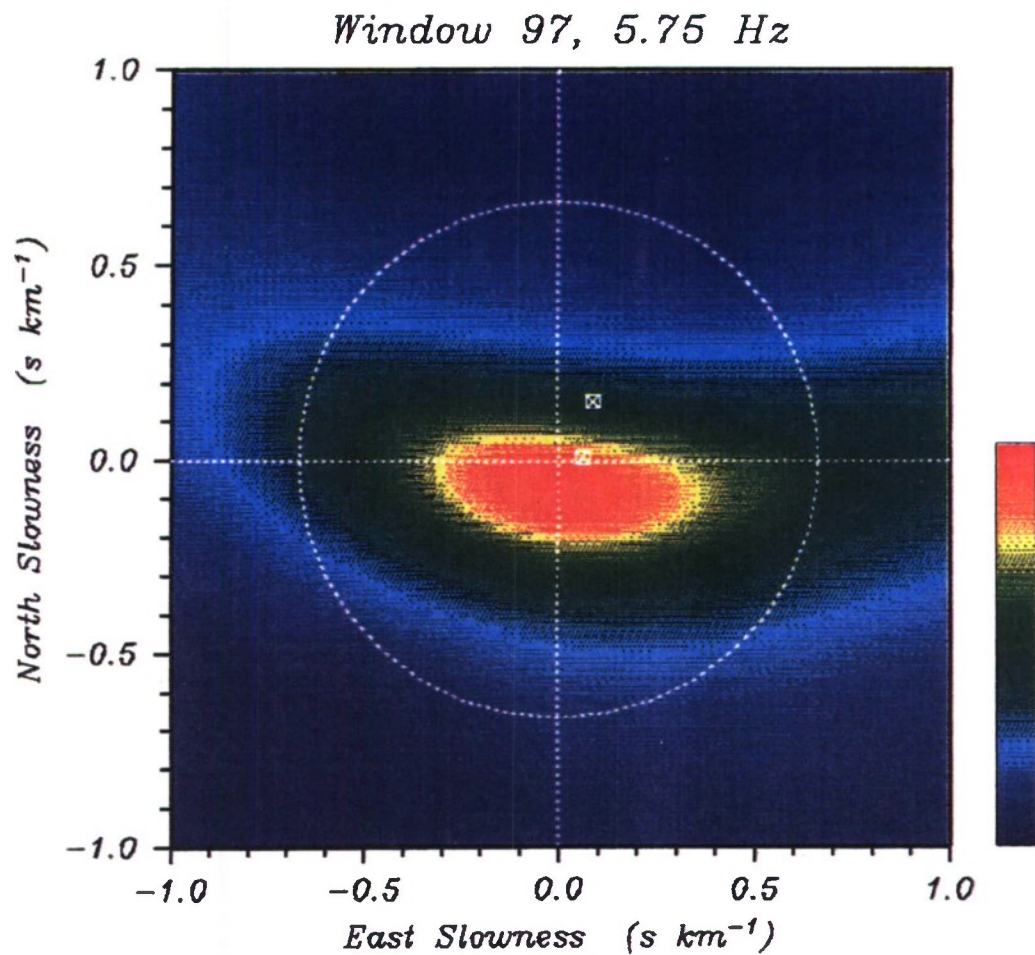
Figure 6.3. Beamforming on the ship signals at 5.75 Hz. The axes are wavenumber times the analysis frequency giving slowness. Color at each point is proportional to the power. The azimuth of a slowness vector gives the direction of propagation rather than the direction towards the source. The two squares are the expected ship bearings. At this frequency the *R/V Melville* emits a strong signal and is located successfully.
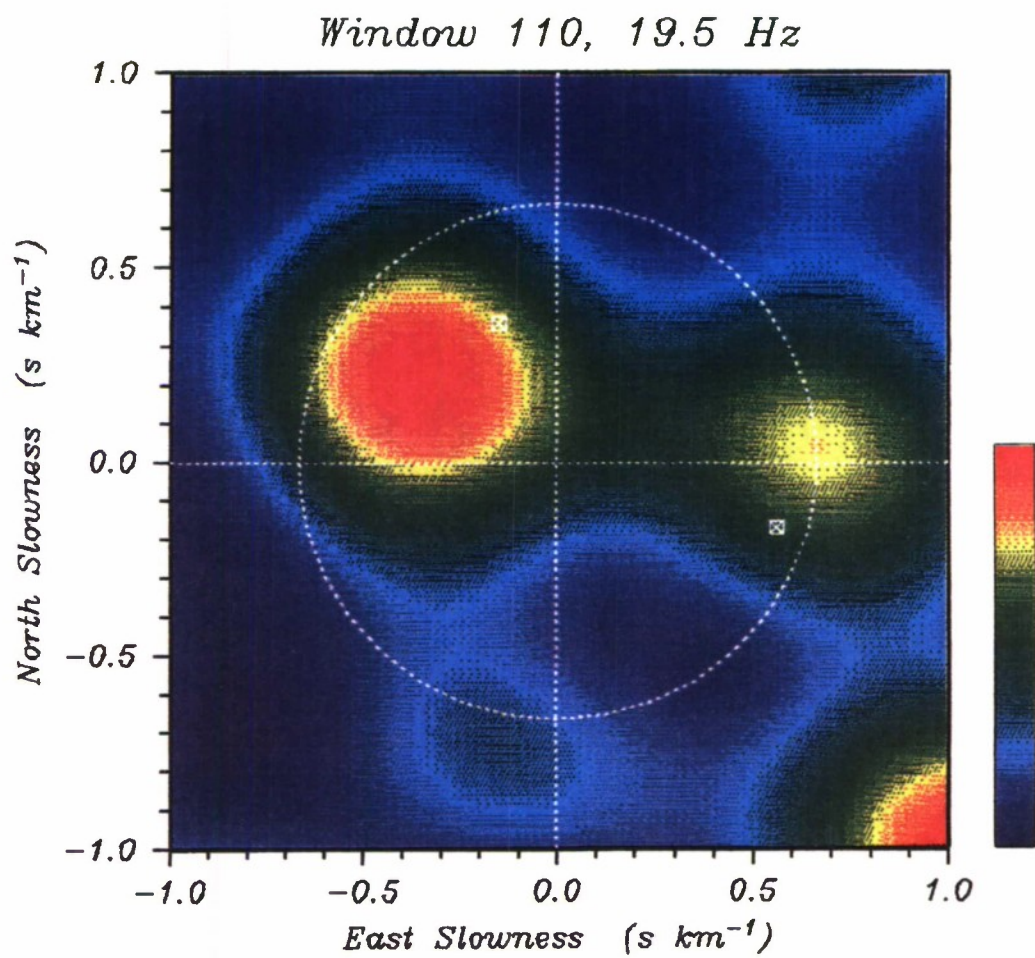
Figure 6.4. Beamforming on the ship signals at 19.5 Hz. At this frequency the *USNS Narragansett* emits the stronger signal but there is a small error in the bearing estimation.
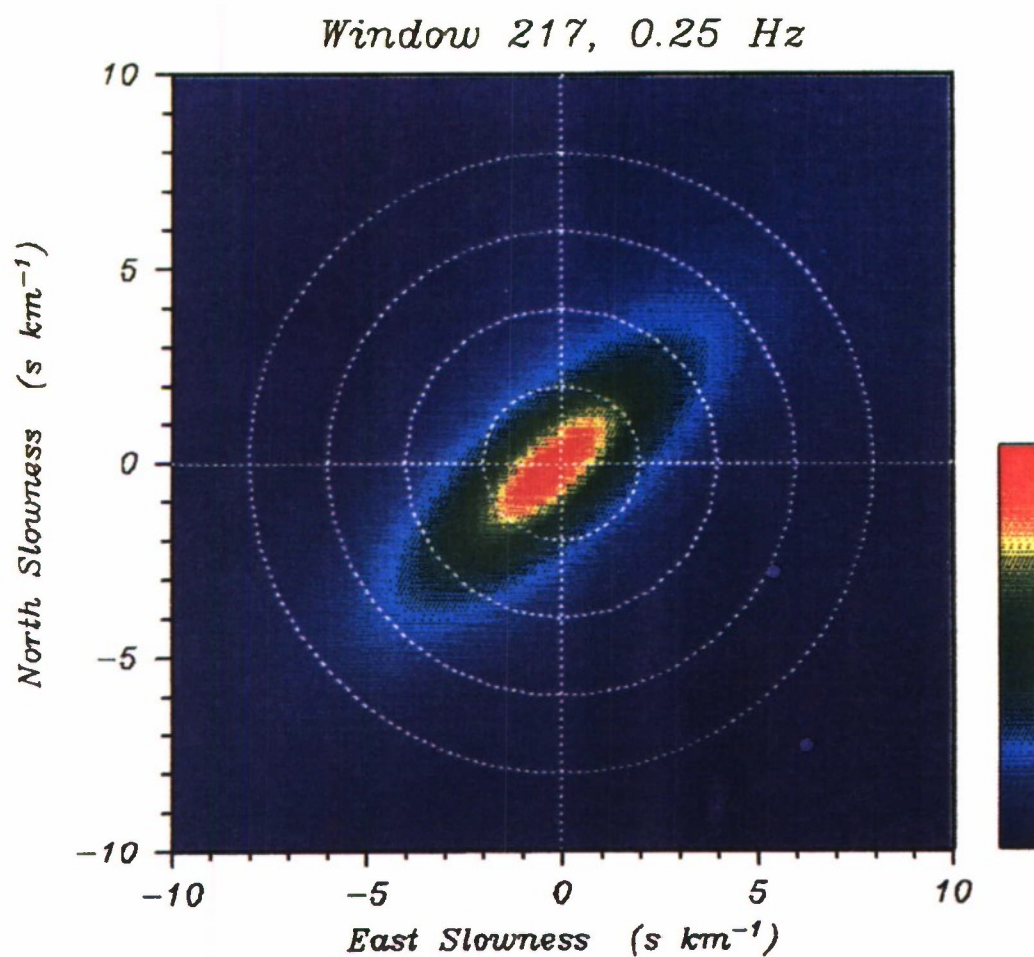
Figure 6.5. Beamforming on microseism noise at 0.25 Hz. The observed phase slowness is not resolvably different from zero.
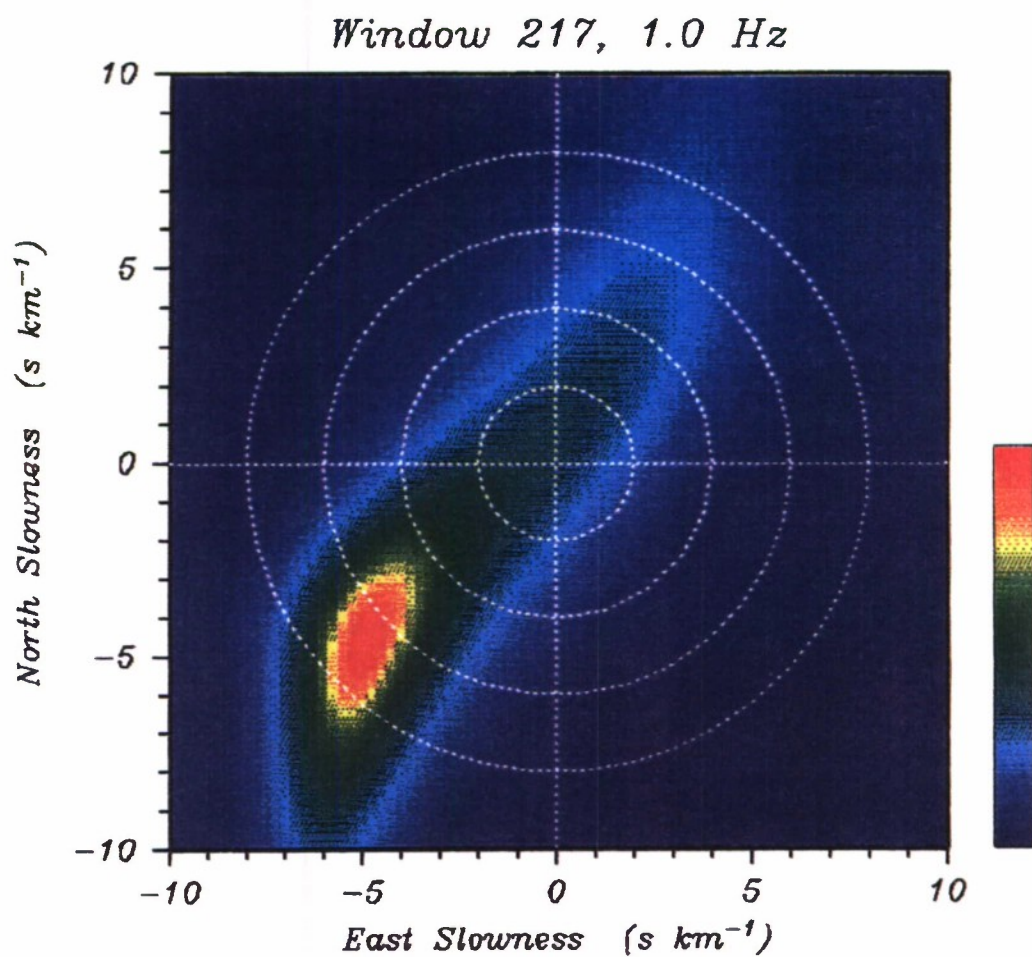
Figure 6.6. Beamforming on microseism noise at 1.0 Hz. The direction of propagation is toward the southwest and with a slowness of 7 s km^{-1}.
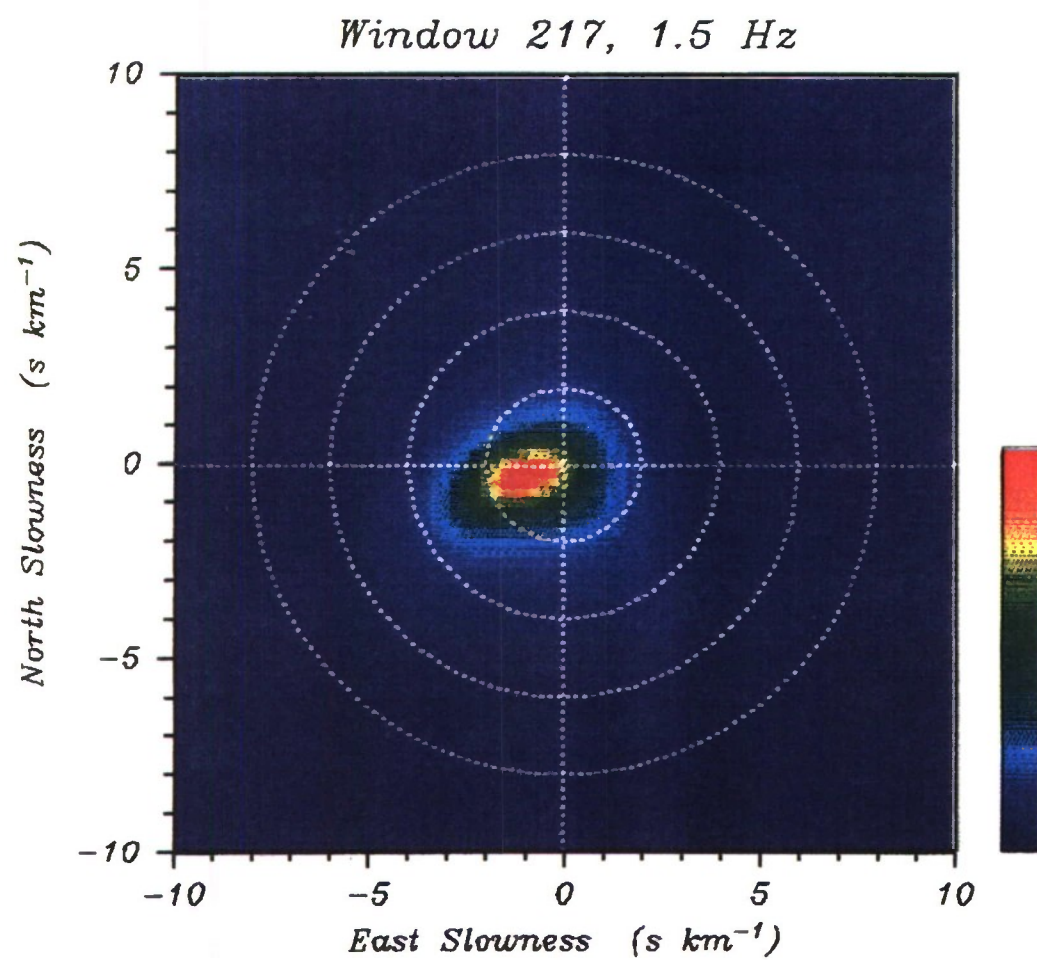
Figure 6.7. Beamforming on microseism noise at 1.5 Hz. The phase slowness is about 1 s km^{-1}.
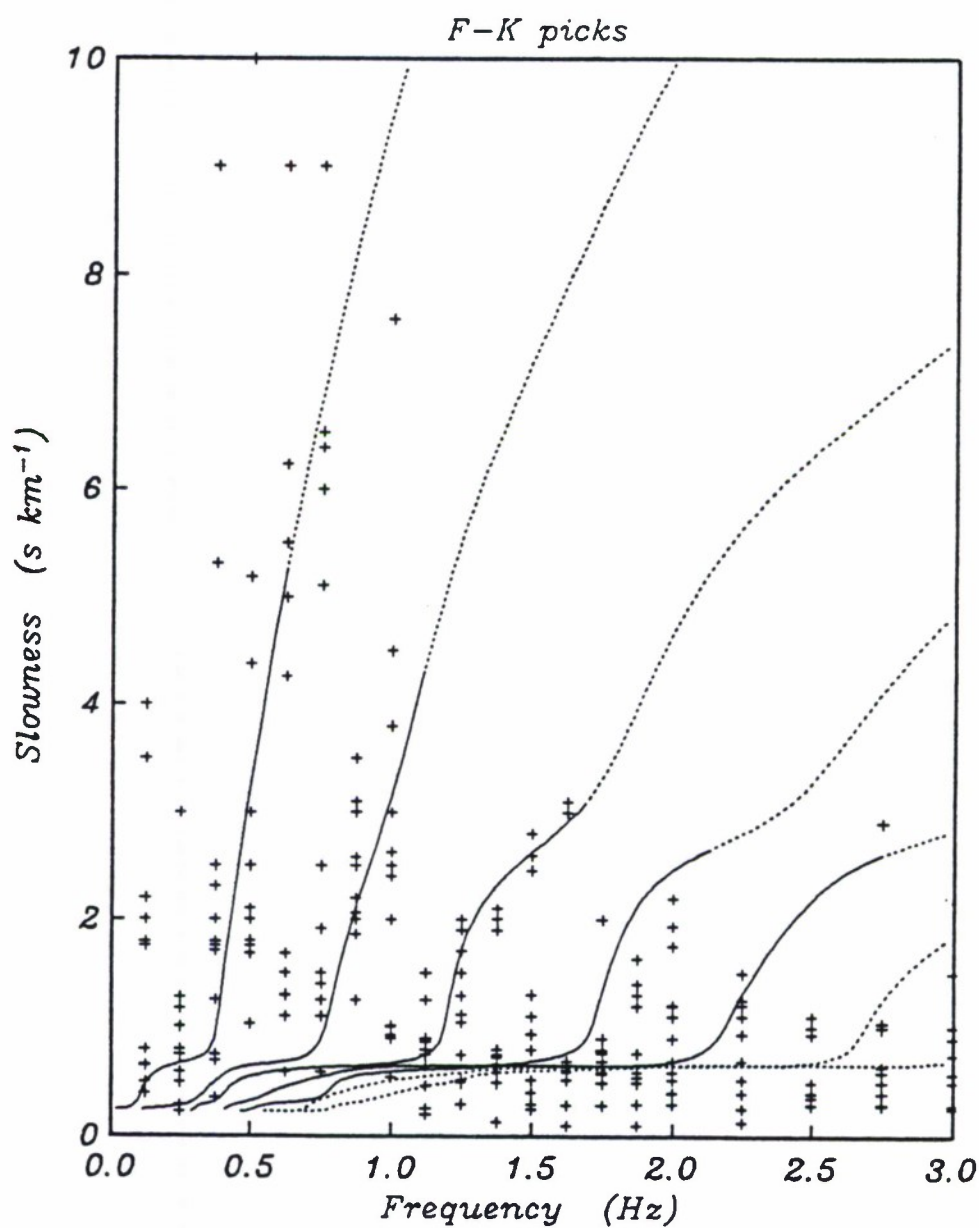
Figure 6.8. Summary of the phase slowness peaks for the first 20 recording windows plotted as a function of frequency. Scatter is substantial but the points lie near the predicted dispersion curves. The solid part of each curve is the frequency range at which the given mode is dominant according to the coherence model.
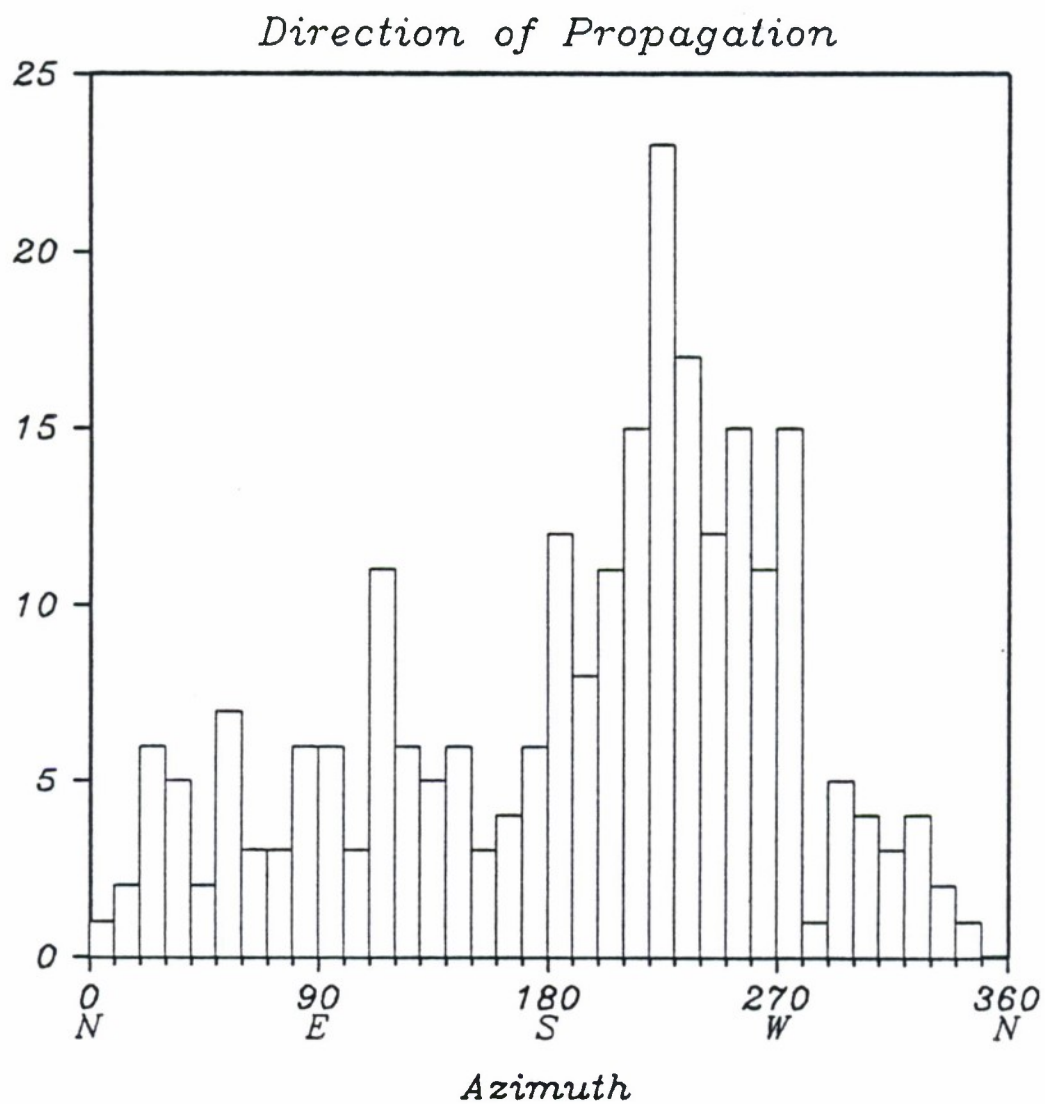
Figure 6.9. Summary of the direction of microseism propagation for the same 20 records as in Figure 6.8. Azimuth picks are binned in 10° intervals. A predominant southwesterly direction is evident.

REFERENCES

Adair, R. G., Microseisms in the deep Ocean: Observations and Theory, PhD Thesis, 166 pp., University of California, San Diego, La Jolla, Ca., 1985.

Adair, R. G., J. A. Orcutt, and T. H. Jordan, Low frequency noise observations in the deep ocean, *J. Acoust. Soc. Am.*, *80*, 633-645, 1986.

Adair, R. G., J. A. Orcutt, and T. H. Jordan, Preliminary analysis of ocean bottom and sub-bottom microseism noise during the Ngendei experiment, in *Init. Repts. DSDP*, edited by H. W. Menard, J. Natland, T. H. Jordan, and J. A. Orcutt, vol. 91, pp. 357-375, U.S. Govt. Printing Office, Washington, D.C., 1987.

Capon, J., High resolution frequency-wavenumber analysis, *Proc. IEEE*, *57*, 1408-1418, 1969.

Capon, J., Signal processing and frequency-wavenumber spectrum analysis fo a large aperture seismic array, in *Methods of Computational Physics*, edited by B. A. Bolt, vol. 13, pp. 2-59, Academic Press, New York, N.Y., 1973.

Chave, A. D., Mutliple window spectral analysis, unpublished manuscript, 1988.

Claerbout, J. F., *Fundamentals of Geophysical Data Processing*, McGraw-Hill, New York, N.Y., 1976.

Clancy, R. M., J. E. Kaitala, and L. F. Zambresky, The Fleet Numerical Oceanography Center Global Spectral Ocean Wave Model, *Bull. Amer. Meteor. Soc.*, *67*, 498-512, 1986.

Cox, C. S., T. Deaton, and S. C. Webb, A deep-sea differential pressure gauge, *J. Atmos. and Ocean Tech.*, *2*, 237-246, 1984.

Deacon, B. E. R., Relation between sea waves and microseisms, *Nature*, *160*, 419-421, 1947.

Dougherty, M. E. and R. A. Stephen, Seismic energy partitioning and scattering in laterally heterogeneous ocean crust, *PAGEOPH*, *128*, 195-229, 1988.

D'Spain, G. L. and W. H. Hodgkiss, Comparison of swallow float ocean bottom seismometer and sonobuoy data in the VLF band, MPL Technical Memorandum MPL-U-32/88, Marine Physical Laboratory, San Diego, Ca., 1988.

Duennebier, F. K., C. S. McCreery, D. Harris, R. K. Cessaro, C. Fisher, and P. Anderson, OSS IV: Noise levels, signal-to-noise ratios, and noise sources, in *Init. Repts. DSDP*, edited by F. K. Duennebier, R. A. Stephen, and J. F. Gettrust, vol. 88, U.S. Govt. Printing Office, Washington, D.C., 1987.

Dziewonski, A. M., G. Ekström, J. E. Franzen, and J. H. Woodhouse, Global seismicity of 1979: Centroid-moment tensor solutions for 524 earthquakes, *Phys. Earth Planet. Interiors*, *34*, 129-136, 1987.

Efron, B., *The Jackknife, the Bootstrap, and Other Resampling Plans*, SIAM, Philadelphia, Pa., 1982.

Gilbert, J. F., Excitation of normal modes of the earth by earthquake sources, *Geophys. J. R. Astr. Soc., 22,* 223-226, 1971.

Gomberg, J. S. and T. G. Masters, Waveform modeling using locked-mode synthetic and differential seismograms: application to determination of the structure of Mexico, *Geophysical J., 94,* 193-218, 1988.

Hasselman, K. A., A statistical analysis of the generation of microseisms, *Rev. Geophys. Space Phys., 1,* 177-210, 1963.

Haubrich, R. A., Earth noise, 5 to 500 millicyles per second - 1. Spatial stationarity, normality, and nonlinearity, *J. Geophys. Res., 70,* 1415-1427, 1965.

Haubrich, R. A., Array design, *Bull. Seis. Soc. Am., 58,* 977-991, 1968.

Haubrich, R. A. and R. L. McCamy, Microseisms: coastal and pelagic sources, *Rev. Geophys., 7,* 539-572, 1969.

Haubrich, R. A., W. H. Munk, and F. E. Snodgrass, Comparative spectra of microseism and swell, *Bull. Seismol. Soc. Am., 53,* 1032-1039, 1963.

Hughes, B., Estimation of underwater sound (and infrasound) produced by nonlinearly interacting waves, *J. Acoust. Soc. Am., 60,* 1032-1039, 1976.

Iyer, H. M., History and science of microseisms, VESIAC state art rept., 4410-64x, 1964.

Jenkins, G. M. and D. G. Watts, *Spectral Analysis and its Applications*, Holden-Day, San Francisco, Ca., 1968.

Kibblewhite, A. C. and K. C. Ewans, Wave-wave interactions, microseisms and, infrasonic ambient noise in the ocean, *J. Acoust. Soc. Am., 78,* 981-994, 1986.

LaCoss, R. T., E. J. Kelly, and M. N. Toksoz, Estimation of noise structure using arrays, *Geophysics, 34,* 21-38, 1969.

Lang, S. W. and J. H. McClellan, Frequency estimation with maximum entropy spectral estimators, *IEEE Trans. Acoust., Speech, Signal Processing, ASSP-28,* 716-724, 1981.

Latham, G. V. and G. H. Sutton, Seismic measurements on the ocean floor 1, Bermuda area, *J. Geophys. Res., 71,* 2545-1573, 1966.

Levander, A. R. and N. R. Hill, P-SV resonances in irregular low-velocity surface layers, *Bull. Seism. Soc. Am., 75,* 847-864, 1985.

Longuet-Higgins, M. S., A theory on the origin of microseisms, *Phil. Trans. Roy. Soc., Series A, 243,* 1-35, 1950.

Longuet-Higgins, M. S., D. E. Cartwright, and N. D. Smith, Observations of the directional spectrum of sea waves using the motion of a floating buoy, in *Ocean Wave Spectra*, pp. 111-132, Prentice-Hall, Englewood Cliffs, N. J., 1963.

Lowenstein, C. D., Navigation and data logging for the MPL Deep Tow, in *Trans. of the Application of Sea Going Computers 1969 Symposium*, pp. 91-98, Marine Technological Society, 1969.

Makhoul, J., Linear prediction: A tutorial review, *Proc. IEEE, 63,* 561-580, 1975.

McCreery, C. S. and F. K. Duennebier, Ambient infrasonic noise and wind, Submitted to *Bull. Seis. Soc. Am.,* 1989.

Miche, M., Mouvements ondulatoires de la mer en profondeur constante ou decroissante, *Ann. Ponts Chausses, 114,* 25-87, 1944.

Moore, R. D., L. M. Dorman, C.-Y. Huang, and D. L. Berliner, An ocean bottom microprocessor-based seismometer, *Mar. Geophys. Res., 4,* 451-477, 1981.

Priestley, M. B., *Spectral Analysis and Time series*, Academic Press, Orlando, Fla., 1981.

Phillips, O. M., *The Dynamics of the Upper Ocean, 2nd. edition*, Cambridge University Press, Cambridge, U.K., 1980.

Purdy, G. M. and A. M. Dziewonski (eds.), Proceedings of a Workshop on Broad-band Downhole Seismometers in the Deep Ocean, Woods Hole Oceanographic Institution, Woods Hole, Ma., 1988.

Rauch, D., Experimental and theoretical studies of seismic interface waves in coastal waters, in *Bottom-interacting Ocean Acoustics*, edited by W. A. Kuperman and F. B. Jensen, vol. 5, pp. 307-327, Plenum Press, New York, N.Y., 1980.

Riedesel, M. A. and T. H. Jordan, Display and assessment of moment tensors, *Bull. Seismol. Soc. Am., 79,* 85-100, 1989.

Sauter, A. W., L. M. Dorman, and A. E. Schreiner, A study of sea floor structure using ocean bottom shots, in *Ocean seismo-acoustics, low frequency underwater acoustics*, edited by T. Akal and J. M. Berkson, vol. 16, Plenum Press, New York, N.Y., 1986.

Sauter, A. W., Studies of the upper oceanic sea floor using ocean bottom seismometers, PhD. thesis, 100 pp., University of California, San Diego, La Jolla, Ca., 1987.

Schmidt, H. and W. A. Kuperman, Estimation of surface noise source level from low-frequency seismo-acoustic ambient noise measurements, *J. Acoust. Soc. Am., 84,* 2153-2162, 1988.

Schmidt, R. O., Multiple emitter location and signal parameter estimation, *IEEE Trans. Antennas Propagat., AP-34,* 276-280, 1986.

Schneider, W. A., P. J. Farrell, and R. E. Brannian, Collection and analysis of Pacific Ocean-bottom seismic data, *Geophysics, 29,* 745-771, 1964.

Slepian, D. and H. O. Pollack, Prolate spheroidal wave functions, Fourier analysis and uncertainty-I, *Bell Syst. Tech. J., 40,* 43-64, 1961.

Slepian, D., Prolate spheroidal wave functions, Fourier analysis and uncertainty-IV: The discrete case, *Bell Syst. Tech. J., 57,* 1371-1429, 1978.

Spiess, F. N. and P. Lonsdale, Deep Tow rise crest exploration techniques, *Marine Technology Soc. J., 16,* 67-74, 1982.

Spudich, P. K. and J. A. Orcutt, Petrology and porosity of an oceanic crustal site: results from wave modeling of seismic refraction data, *J. Geophys. Res., 85,* 1407-1433, 1980.

Thomson, D. J., Spectrum estimation and harmonic analysis, *Proc. IEEE, 70,* 1055-1096, 1982.

Tuthill, J. D., B. T. R. Lewis, and J. D. Garmany, Stoneley waves, Lopez Island noise and deep sea noise from 1 to 5 Hz, *Mar. Geophys. Res., 5,* 95-108, 1981.

Tyler, G. L., C. C. Teague, R. H. Stewart, A. M. Peterson, W. H. Munk, and J. W. Joy, *Deep Sea Res., 21,* 989-1026, 1974.

Webb, S. C., Coherent pressure fluctuations observed at two sites on the deep sea floor, *Geophys. Res. Lett., 13,* 141-144, 1986.

Webb, S. C. and C. S. Cox, Observations and modeling of seafloor microseisms, *J. Geophys. Res., 91,* 7343-7358, 1986.

Welch, P. D., The use of the fast Fourier transform for the estimation of power spectra: A method based on time averaging over short, modified periodograms, *IEEE Trans. Audio Electro-acoust., AU-15,* 70-73, 1967.

Wiechert, E., Verhandlungen der Zweiten Internationalen Seimologischen Konferenz,, in *Gerlands. Beitr. Geophys.,* pp. 41-43, 1904.

Woodhouse, J. H., Efficient and stable methods for performing seismic calculations in stratified media, in *Proceedings of the International School of Physics Enrico Fermi Course,* vol. 78, pp. 127-151, North Holland, Amsterdam, Netherlands, 1980.

Yeats, R. S., B. U. Haq, J. A. Baron, D. Bukry, J. K. Crouch, C. Denham, A. C. Douglas, V. I. Grechin, M. Leiner, A. R. Neim, S. Pal, K. A. Pisciotto, R. Z. Poore, T. Shibata, and R. Wolfart, Site 469: Base of the Patton Escarpment, in *Init. Repts. DSDP,* vol. 63, U.S. Govt. Printing Office, Washington, D.C., 1981.

LIST OF RECORDED WINDOWS

The stars in each position indicate whether there is usable data for the given window for each component of each instrument. An empty circle indicates that there is data for that event but that the record start time is significantly different from the programmed time. Note that instruments 1, 2, 4, 8, 12, 13, and 14 were programmed to record at six hour intervals except during the shooting phase which lasted from 0200 to 0600 on day 113, during which time they recorded every 15 minutes. Instruments 5 and 6 were programmed to record at 15 minute intervals until 0600 on day 114 and every 3 hours thereafter.

record	day	time (CUT)	V 1 2 4 5 6 8 12 13 14	P 1 2 4 5 6 8 12 13 14	H1 1 2 4 5 6 8 12 13 14	H2 1 2 4 5 6 8 12 13 14
1	112	00:01	* *	** * *	** *	** **
2	112	00:16	**	**	**	**
3	112	00:31	**	**	**	**
4	112	00:46	**	**	**	**
5	112	01:01	**	**	**	**
6	112	01:16	**	**	**	**
7	112	01:31	**	**	**	**
8	112	01:46	**	**	**	**
9	112	02:01	**	**	**	**
10	112	02:16	**	**	**	**
11	112	02:31	**	**	**	**
12	112	02:46	**	**	**	**
13	112	03:01	**	**	**	**
14	112	03:16	**	**	**	**
15	112	03:31	**	**	**	**
16	112	03:46	**	**	**	**
17	112	04:01	**	**	**	**
18	112	04:16	**	**	**	**
19	112	04:31	**	**	**	**
20	112	04:46	**	**	**	**
21	112	05:01	**	**	**	**
22	112	05:16	**	**	**	**
23	112	05:31	**	**	**	**
24	112	05:46	**	**	**	**
25	112	06:01	********	********	********	* *****

record	day	time (CUT)	V	P	H1	H2
			1 2 4 5 6 8 12 13 14	1 2 4 5 6 8 12 13 14	1 2 4 5 6 8 12 13 14	1 2 4 5 6 8 12 13 14
26	112	06:16	**	**	**	**
27	112	06:31	**	**	**	**
28	112	06:46	**	**	**	**
29	112	07:01	**	**	**	**
30	112	07:16	**	**	**	**
31	112	07:31	**	**	**	**
32	112	07:46	**	**	**	**
33	112	08:01	**	**	**	**
34	112	08:16	**	**	**	**
35	112	08:31	**	**	**	**
36	112	08:46	**	**	**	**
37	112	09:01	**	**	**	**
38	112	09:16	**	**	**	**
39	112	09:31	**	**	**	**
40	112	09:46	**	**	**	**
41	112	10:01	**	**	**	**
42	112	10:16	**	**	**	**
43	112	10:31	**	**	**	**
44	112	10:46	**	**	**	**
45	112	11:01	**	**	**	**
46	112	11:16	**	**	**	**
47	112	11:31	**	**	**	**
48	112	11:46	**	**	**	**
49	112	12:01	********	*******	********	********
50	112	12:16	**	**	**	**
51	112	12:31	**	**	**	**
52	112	12:46	**	**	**	**
53	112	13:01	**	**	**	**
54	112	13:16	**	**	**	**
55	112	13:31	**	**	**	**
56	112	13:46	**	**	**	**
57	112	14:01	**	**	**	**
58	112	14:16	**	**	**	**
59	112	14:31	**	**	**	**
60	112	14:46	**	**	**	**
61	112	15:01	**	**	**	**
62	112	15:16	**	**	**	**
63	112	15:31	**	**	**	**
64	112	15:46	**	**	**	**
65	112	16:01	**	**	**	**
66	112	16:16	**	**	**	**
67	112	16:31	**	**	**	**
68	112	16:46	**	**	**	**
69	112	17:01	**	**	**	**
70	112	17:16	**	**	**	**
71	112	17:31	**	**	**	**
72	112	17:46	**	**	**	**
73	112	18:01	********	********	********	* ******
74	112	18:16	**	**	**	**
75	112	18:31	**	**	**	**

record	day	time (CUT)	V 1 2 4 5 6 8 12 13 14	P 1 2 4 5 6 8 12 13 14	H1 1 2 4 5 6 8 12 13 14	H2 1 2 4 5 6 8 12 13 14
76	112	18:46	**	**	**	**
77	112	19:01	**	**	**	**
78	112	19:16	**	**	**	**
79	112	19:31	**	**	**	**
80	112	19:46	**	**	**	**
81	112	20:01	**	**	**	**
82	112	20:16	o*	o*	o*	o*
83	112	20:31	**	**	**	**
84	112	20:46	**	**	**	**
85	112	21:01	**	**	**	**
86	112	21:16	**	**	**	**
87	112	21:31	**	**	**	**
88	112	21:46	**	**	**	**
89	112	22:01	**	**	**	**
90	112	22:16	**	**	**	**
91	112	22:31	**	**	**	**
92	112	22:46	**	**	**	**
93	112	23:01	**	**	**	**
94	112	23:16	*	**	**	**
95	112	23:31	**	**	**	**
96	112	23:46	*	**	**	**
97	113	00:01	*** ****	********	********	* ******
98	113	00:16		**	**	**
99	113	00:31		**	**	**
100	113	00:46		**	**	**
101	113	01:01		**	**	**
102	113	01:16		**	**	**
103	113	01:31		**	**	**
104	113	01:46		**	**	**
105	113	02:01	*********	*********	*********	*********
106	113	02:16	*********	*********	*********	*********
107	113	02:31	*********	*********	*********	*********
108	113	02:46	*********	*********	*********	*********
109	113	03:01	*********	*********	*********	*********
110	113	03:16	*********	*********	*********	*********
111	113	03:31	*********	*********	*********	*********
112	113	03:46	*********	*********	*********	*********
113	113	04:01	*********	*********	*********	*********
114	113	04:16	*********	*********	*********	*********
115	113	04:31	*********	*********	*********	*********
116	113	04:46	*********	*********	*********	*********
117	113	05:01	*********	*********	*********	*********
118	113	05:16	*********	*********	*********	*********
119	113	05:31	*********	*********	*********	*********
120	113	05:46	*********	*********	*********	*********
121	113	06:01	**** * **	****** **	*********	** *** **
122	113	06:16	**	**	**	**
123	113	06:31	**	**	**	**
124	113	06:46	**	**	**	**
125	113	07:01	**	**	**	**

record	day	time (CUT)	V 1 2 4 5 6 8 12 13 14	P 1 2 4 5 6 8 12 13 14	H1 1 2 4 5 6 8 12 13 14	H2 1 2 4 5 6 8 12 13 14
126	113	07:16	**	**	**	**
127	113	07:31	**	**	**	**
128	113	07:46	**	**	**	**
129	113	08:01	**	**	**	**
130	113	08:16	**	**	**	**
131	113	08:31	**	**	**	**
132	113	08:46	**	**	**	**
133	113	09:01	**	**	**	**
134	113	09:16	**	**	**	**
135	113	09:31	**	**	**	**
136	113	09:46	**	**	**	**
137	113	10:01	**	**	**	**
138	113	10:16	**	**	**	**
139	113	10:31	**	**	**	**
140	113	10:46	**	**	**	**
141	113	11:01	**	**	**	**
142	113	11:16	**	**	**	**
143	113	11:31	**	**	**	**
144	113	11:46	**	**	**	**
145	113	12:01	** ******	** ******	** ******	********
146	113	12:16	**	**	**	**
147	113	12:31	**	**	**	**
148	113	12:46	**	**	**	**
149	113	13:01	**	**	**	**
150	113	13:16	**	**	**	**
151	113	13:31	**	**	**	**
152	113	13:46	**	**	**	**
153	113	14:01	**	**	**	**
154	113	14:16	**	**	**	**
155	113	14:31	**	**	**	**
156	113	14:46	**	**	**	**
157	113	15:01	**	**	**	**
158	113	15:16	**	**	**	**
159	113	15:31	*	**	**	**
160	113	15:46	**	**	**	**
161	113	16:01	**	**	**	**
162	113	16:16	**	**	**	**
163	113	16:31	**	**	**	**
164	113	16:46	**	**	**	**
165	113	17:01	**	**	**	**
166	113	17:16	**	**	**	**
167	113	17:31	**	**	**	**
168	113	17:46	**	**	**	**
169	113	18:01	*********	*********	*********	*********
170	113	18:16	**	**	**	**
171	113	18:31	**	**	**	**
172	113	18:46	**	**	**	**
173	113	19:01	**	**	**	**
174	113	19:16	**	**	**	**
175	113	19:31	**	**	**	**

record	day	time (CUT)	V	P	H1	H2
			1 2 4 5 6 8 12 13 14	1 2 4 5 6 8 12 13 14	1 2 4 5 6 8 12 13 14	1 2 4 5 6 8 12 13 14
176	113	19:46	**	**	**	**
177	113	20:01	**	**	**	**
178	113	20:16	**	**	**	**
179	113	20:31	**	**	**	**
180	113	20:46	**	**	**	**
181	113	21:01	**	**	**	**
182	113	21:16	**	**	**	**
183	113	21:31	**	**	**	**
184	113	21:46	**	**	**	**
185	113	22:01	**	**	**	**
186	113	22:16	**	**	**	**
187	113	22:31	**	**	**	**
188	113	22:46	**	**	**	**
189	113	23:01	**	*	**	**
190	113	23:16	**	**	**	**
191	113	23:31	**	**	**	**
192	113	23:46	**	**	**	**
193	114	00:01	*********	*********	**********	*********
194	114	00:16	**	**	**	**
195	114	00:31	**	**	**	**
196	114	00:46	**	**	**	**
197	114	01:01	**	**	**	**
198	114	01:16	**	**	**	**
199	114	01:31	**	**	**	**
200	114	01:46	**	**	**	**
201	114	02:01	**	**	**	**
202	114	02:16	**	**	**	**
203	114	02:31	**	**	**	**
204	114	02:46	**	*	**	**
205	114	03:01	**	*	**	**
206	114	03:16	**	*	**	**
207	114	03:31	**	*	**	**
208	114	03:46	**	*	**	**
209	114	04:01	**	*	**	**
210	114	04:16	**	*	**	**
211	114	04:31	**	*	**	**
212	114	04:46	**	*	**	**
213	114	05:01	**	*	**	**
214	114	05:16	**	*	**	**
215	114	05:31	**	*	**	**
216	114	05:46	*	*	**	**
217	114	06:01	****** **	*** *****	****** **	****** **
218	114	09:01	**	*	**	**
219	114	12:01	** *****	** *****	** ******	** ******
220	114	15:01	*	*	**	**
221	114	18:01	** **o*o*	** *o*o*	** **o*o*	** **o*o*
222	114	21:01	**	*	**	**
223	115	00:01	** *** **	** ** **	** ******	** *** **
224	115	03:01	**	*	**	*
225	115	06:01	** *****	** *****	** o*****	** o*****

record	day	time (CUT)	V 1 2 4 5 6 8 12 13 14	P 1 2 4 5 6 8 12 13 14	H1 1 2 4 5 6 8 12 13 14	H2 1 2 4 5 6 8 12 13 14
226	115	09:01	**	*	**	**
227	115	12:01	** ******	** *****	** ******	** ******
228	115	15:01	**	*	**	**
229	115	18:01	** *****	** *****	** ******	** ******
230	115	21:01	**	*	**	**
231	116	00:01	*o *** **	*o ** **	*o *** **	*o *** **
232	116	03:01	**	*	**	**
233	116	06:01	*****o***	** o***	**** o***	**** o***
234	116	09:01	**	*	**	**
235	116	12:01	**o******	**o *****	**o******	**o******
236	116	15:01	**	*	**	**
237	116	18:01	*** *****	*** *****	*********	*********
238	116	21:01	**	*	**	**
239	117	00:01	******* *	*** *****	*********	*********
240	117	03:01	**	*	**	**
241	117	06:01	**o** ***	**o * ***	**o** ***	**o** ***
242	117	09:01	**	*	**	**
243	117	12:01	*********	*** *****	*********	*********
244	117	15:01	**	*	**	**
245	117	18:01	*********	*** *****	*** *****	*** *****
246	117	21:01	*	*	o*	o*
247	118	00:01	*** ** **	*** ** **	****** **	*** ** **
248	118	03:01	**	*	**	*
249	118	06:01	**o******	**o ** **	**o*** **	**o*** **
250	118	09:01	**	*	**	**
251	118	12:01	*o**** **	*o* ** **	*o**** **	*o**** **
252	118	15:01	**	*	**	**
253	118	18:01	**o*** **	**o ** **	**o*** **	**o*** **
254	118	21:01	**	*	**	**
255	119	00:01	********o	*** ****	********o	********o
256	119	03:01	**	*	**	**
257	119	06:01	o********	o** *** *	o****** *	o****** *
258	119	09:01	**	*	**	**
259	119	12:01	****** **	*** ** **	*********	****** **
260	119	15:01	**	*	**	**
261	119	18:01	o***** **	o** ** **	o********	o***** **
262	119	21:01	**	*	**	**
263	120	00:01	*********	*** *****	*********	*********
264	120	03:01	**	*	**	**
265	120	06:01	****** **	*** ** **	*** ** **	*** ** **
266	120	09:01	**	*	**	**
267	120	12:01	*********	*** *****	*********	*********
268	120	15:01	**	*	**	**
269	120	18:01	********o	*** ****o	********o	********o
270	120	21:01	o*	*	o*	**
271	121	00:01	*****o***	*** *o***	*****o***	*****o***
272	121	03:01	**	*	**	**
273	121	06:01	*********	*** *****	*********	*********
274	121	09:01	*o	o	o	*o
275	121	12:01	*********	*** *****	*********	*********

record	day	time (CUT)	V	P	H1	H2
			1 2 4 5 6 8 12 13 14	1 2 4 5 6 8 12 13 14	1 2 4 5 6 8 12 13 14	1 2 4 5 6 8 12 13 14
276	121	15:01	**	*	**	**
277	121	18:01	****** **	*** *****	*********	*********
278	121	21:01	**	*	**	**
279	122	00:01	*********	*** *****	*********	*********
280	122	03:01	**	*	**	**
281	122	06:01	*********	*** ** **	*********	*********
282	122	09:01	**	*	*	**
283	122	12:01	****o****	*** o****	****o****	****o****
284	122	15:01	**	*	*	**
285	122	18:01	*o**o****	*o* o****	*o** ****	*o**o****
286	122	21:01	**	*	*	**
287	123	00:01	****** **	*** *****	*********	****** **
288	123	03:01	**	*	**	**
289	123	06:01	****** **	*** ** **	****** **	****** **
290	123	09:01	**	*	**	**
291	123	12:01	o********	o** *****	o********	o********
292	123	15:01	**	*	**	**
293	123	18:01	*****o**o	*** *o *o	*****o**o	*****o**o
294	123	21:01	o		o	*o
295	124	00:01	********o	*** ****o	********o	********o
296	124	03:01	**	*	**	**
297	124	06:01	*o**** **	*o* ** **	*o**** **	*o**** **
298	124	09:01	**	*	**	**
299	124	12:01	*********	*** *****	*********	*********
300	124	15:01	**	*	**	**
301	124	18:01	****** **	*** *****	*********	*********
302	124	21:01	**	*	**	**
303	125	00:01	*********	*** *****	*********	*********
304	125	03:01	**	*	**	**
305	125	06:01	*********	*** *****	*********	*********
306	125	09:01	**	*	**	**
307	125	12:01	*******o*	*** ***o*	*******o*	*******o*
308	125	15:01	**	*	**	**
309	125	18:01	*********	*** *****	*********	*********
310	125	21:01	**	*	**	**
311	126	00:01	*o**** **	*o* *****	*o**** **	*o*******
312	126	03:01	**	*	**	**
313	126	06:01	*****o **	*** *o **	*****o **	*****o **
314	126	09:01	**	*	*	**
315	126	12:01	*****o***	*** *o***	*****o***	*****o***
316	126	15:01	*	*	**	**
317	126	18:01	*********	*** *****	*********	*********
318	126	21:01	*	*	**	**
319	127	00:01	**** ****	*** *****	*********	*********
320	127	03:01	*	*	**	**
321	127	06:01	*** * **	*** ** **	***o** **	***o** **
322	127	09:01	*	*	**	**
323	127	12:01	*** * **	*** ** **	****** **	****** **
324	127	15:01	*	*	o*	o*
325	127	18:01	**** ****	*** *** *	*********	******* *

record	day	time (CUT)	V	P	H1	H2
			1 2 4 5 6 8 12 13 14	1 2 4 5 6 8 12 13 14	1 2 4 5 6 8 12 13 14	1 2 4 5 6 8 12 13 14
326	127	21:01	*	*	**	**
327	128	00:01	**** * **	*** ** **	****** **	****** **
328	128	03:01	*		*	*
329	128	06:01	**o* * **	** * **	**o* ****	**o* * **
330	128	09:01	*		*	*
331	128	12:01	**** * **	*** ****	**** ****	**** ****
332	128	15:01	*		*	*
333	128	18:01	**** ****	*** ****	** * ****	*** * **
334	128	21:01	*		*	*
335	129	00:01	**** * *o	*** * *o	**** * *o	**** * *o
336	129	03:01	*		*	*
337	129	06:01	**** * **	*** * **	**** * **	**** * **
338	129	09:01	*		*	*
339	129	12:01	**** * **	** * **	** * * **	** * * **
340	129	15:01	*		*	*
341	129	18:01	**** ****	*** ** *	**** ****	*** ****
342	129	21:01	*			
343	130	00:01	**** * oo	*** **oo	**** * o	**** * o
344	130	03:01	*		*	*
345	130	06:01	**** ***o	*** *o	**** *o	*** *o
346	130	09:01	*		*	*
347	130	12:01	**** ****	*** ****	**** ****	**** ****
348	130	15:01	*		*	*
349	130	18:01	**** ****	*** ****	**** ****	**** ****
350	130	21:01	*			*
351	131	00:01	**** * **	*** * **	*** ****	*** * **
352	131	03:01	*			
353	131	06:01	**** * **	*** * **	*** ***	*** * **
354	131	09:01	*			*
355	131	12:01	*o*o * o*	*o* * *	*o* * o	*o*o * o*
356	131	15:01	*			*
357	131	18:01	**** o **	*** o***	** o***	*** o *
358	131	21:01	*			
359	132	00:01	**** o **	*** o **	*** o **	*** o **
360	132	03:01	*			
361	132	06:01	*o * * **	*o * **	*o * *	*o * **
362	132	09:01	*			
363	132	12:01	**** * **	*** * **	*** * **	*** * **
364	132	15:01	*			
365	132	18:01	**** * **	*** **	*** **	*** **
366	132	21:01	*			*
367	133	00:01	**** * **	*** * *	*** * **	**** * **
368	133	03:01	*			
369	133	06:01	**** * **	*** * *	*** * **	*** * **
370	133	09:01	*			
371	133	12:01	**** * o*	*** * *	*** * o*	**** * o*
372	133	15:01	*			*
373	133	18:01	**** * **	*** * *	*** * **	**** * **
374	133	21:01	*			
375	134	00:01	**** * **	*** * *	*** * **	*** * **

record	day	time (CUT)	V (1 2 4 5 6 8 12 13 14)	P (1 2 4 5 6 8 12 13 14)	H1 (1 2 4 5 6 8 12 13 14)	H2 (1 2 4 5 6 8 12 13 14)
376	134	03:01	*			
377	134	06:01	**** ****	** ***	** ****	** ****
378	134	09:01	o			
379	134	12:01	**** * **	** * *	*** * **	*** * **
380	134	15:01	*			
381	134	18:01	*o** * **	*o* * *	*o* * **	*o* * *
382	134	21:01	*			
383	135	00:01	**** * **	*** * *	*** * *	*** * **
384	135	03:01	*			
385	135	06:01	*** * **	*** * *	*** * **	*** * **
386	135	09:01				
387	135	12:01	*** * **	*** * *	*** * **	** * **
388	135	15:01				
389	135	18:01	*o* * o*	*o *	*o * o*	*o * o*
390	135	21:01				
391	136	00:01	o** * **	o* * *	o* * **	o** * **
392	136	03:01				
393	136	06:01	*o* ****	*o ***	*o ****	*o ****
394	136	09:01				
395	136	12:01	** * **	** * *	** * **	** * **
396	136	15:01				
397	136	18:01	** ****	** ***	** ****	** ****
398	136	21:01				
399	137	00:01	** * **	** * *	** ****	** * **
400	137	03:01				
401	137	06:01	** * **	** * *	** * **	** * **
402	137	09:01				
403	137	12:01	** * **	** * *	** *	* * *
404	137	15:01				
405	137	18:01	** * **	** *	** * *	** * *
406	137	21:01				
407	138	00:01	** * **	** * *	** * **	** * **
408	138	03:01				
409	138	06:01	** * **	** * *	** * **	** * **
410	138	09:01				
411	138	12:01	** * **	** **	** ** *	** * **
412	138	15:01				
413	138	18:01	** * *	**	** *	** *
414	138	21:01				
415	139	00:01	** * *	** *	** * *	** * *
416	139	03:01				
417	139	06:01	** ** *	** **	** ** *	** ** *
418	139	09:01				
419	139	12:01	** * o	** *	** * o	** * o
420	139	15:01				
421	139	18:01	** * *	** *	** * *	** * *
422	139	21:01				
423	140	00:01	** ** *	** *	** * *	** * *
424	140	03:01				
425	140	06:01	** * *	** *	** * *	** * *

record	day	time (CUT)	V 1 2 4 5 6 8 12 13 14	P 1 2 4 5 6 8 12 13 14	H1 1 2 4 5 6 8 12 13 14	H2 1 2 4 5 6 8 12 13 14
426	140	09:01				
427	140	12:01	*o　　*　　*	*o　　*	*o　　*　　*	*o　　**　*
428	140	15:01				
429	140	18:01	**　　*　　*	**　　*	**　　*	**　　*　　*
430	140	21:01				
431	141	00:01	*o　　*　　*	*o　　*	*o　　**　*	*o　　*　　*
432	141	03:01				
433	141	06:01	o*　　*　　*	o*　　**	o*　　**　*	o*　　**　*
434	141	09:01				
435	141	12:01	**　　**　*	**　　**	**　　**	**　　**　*
436	141	15:01				
437	141	18:01	**　　*	**　　*	**　　*	**　　*
438	141	21:01				
439	142	00:01	**　　o	**　　o*	**　　o*	**　　o*
440	142	03:01				
441	142	06:01	**　　**	**　　**	**　　**	**　　**
442	142	09:01				
443	142	12:01	o*　　**	o*　　**	o*　　**	o*　　**
444	142	15:01				
445	142	18:01	**　　*	**　　*	**　　*	**　　*
446	142	21:01				
447	143	00:01	**　　**	**　　**	**　　**	**　　**
448	143	03:01				
449	143	06:01	**　　**	**　　**	*　　*	**　　**
450	143	09:01				
451	143	12:01	**	**	*	**

ONR/MPL GENERAL DISTRIBUTION LIST

Chief of Naval Research
Department of the Navy
Arlington, Virginia 22217-S000
  Code 12, 122(2), 12S
  112l, 112, 1122,
  1123, 112S, 112S OA,
  1125 GG, 23

ONRDET
Stennis Space Center
Bay St. Louis, Mississippi 39529-5004
  Code 125

Commander
Naval Sea Systems Command
Washington, D. C. 20362
  Code 63DB, 933A

Commanding Officer
Naval Ocean Research and
  Development Activity
Stennis Space Center
Bay. St. Louis, Mississippi 39529-5004
  Code 100, 110, 300, 330,
  200, 220, 240, 2S0, 270,
  320, 360, 3S0

Commander
U.S. Naval Oceanographic Office
NSTL Station
Bay St. Louis, Mississippi 39S22-5004
  Atten: Bill Jobst

Assistant Secretary of the Navy
(Research Engineering & Systems)
Department of the Navy
Washington, D. C. 203S0

Defense Advanced Res. Proj. Agency
TTO - Tactical Technology Office
1400 Wilson Boulevard
Arlington, Virginia 22209-2308
  Atten: John N. Entzminger

National Oceanic & Atmospheric
  Administration
Ocean Engineering Office
6001 Executive Boulevard
Rockville, Maryland 208S2

Commander
Space and Naval Warfare
  Systems Command
Washington, D. C. 20360-S100
  Code PMW-180T, PMW-180-S

Commander
Naval Ship Res. & Dev. Center
Bethesda, Maryland 20084

Executive Secretary
Naval Studies Board
National Academy of Sciences
2101 Constitution Avenue, N.W.
Washington, D.C. 20418

Director
Strategic Systems Proj. Ofc.
Department of the Navy
Washington, D. C. 20361
  Code NSP-20

Commander
Naval Ocean Systems Center
San Diego, California 921S2
  Code 00, 01, 16, 94,
  S4, S41, 60S, 71, 72, 701

Commander
Submarine Development Group ONE
139 Sylvester Road
San Diego, California 92106

Commanding Officer
Civil Engineering Laboratory
Naval Construction Battalion Center
Port Hueneme, California 93043
  Code L40, L42

Commanding Officer
Naval Underwater Systems Center
Newport, Rhode Island 20844
  Atten: E.L. Sullivan

Officer in Charge
Naval Underwater Systems Center
New London Laboratory
New London, Connecticut 06320
  Code 900, 90S, 910, 930, 960

Director of Research
U.S. Naval Research Laboratory
Washington, D. C. 2037S
  Code 2620, 2627, S000, S100, S800

Officer in Charge
Naval Surface Warfare Center
10901 New Hampshire Avenue
White Oak Laboratory Detachment
Silver Spring, Maryland 20903-S000
  Attn: E232 Tech Library

Commanding Officer
Naval Coastal Systems Laboratory
Panama City, Florida 32401

STOIAC
Battelle Columbus Laboratories
505 King Avenue
Columbus, Ohio 43201

Commander
Naval Air Systems Command
Washington, D. C. 20361
  Code 370

Commanding Officer
U.S. Naval Air Development Center
Attention: Bruce Steinberg
Warminster, Pennsylvania 18974

Director
Defense Documentation Center
(TIMA), Cameron Station
S010 Duke Street
Alexandria, Virginia 22314

Institute for Defense Analyses
180t North Beaugard Street
Arlington, Virginia 22311

Superintendent
U.S. Naval Postgraduate School
Monterey, California 93940

Chief Scientist
Navy Underwater Sound Reference Div.
U.S. Naval Research Laboratory
P.O. Box 8337
Orlando, Florida 32806

Supreme Allied Commander
U.S. Atlantic Fleet
ASW Research Center, APO
New York, New York 09019
  Via: ONR 100 M, CNO OP092D1,
  Secretariat of Military,
  Information Control, Committee

Director
Institute of Marine Science
University of Alaska
Fairbanks, Alaska 99701

Director
Applied Physics Laboratory
Johns Hopkins University
Johns Hopkins Road
Laurel, Maryland 20810
  Atten: J. R. Austin

Director
College of Engineering
Department of Ocean Engineering
Florida Atlantic University
Boca Raton, Florida 33431

Director
Marine Research Laboratories
c/o Marine Studies Center
University of Wisconsin
Madison, Wisconsin 53706

Director
Applied Research Laboratory
Pennsylvania State University
P.O. Box 30
State College, Pennsylvania 16802

Director
Applied Physics Laboratory
University of Washington
1013 NE 40th Street
Seattle, Washington 9819S

Director
The Univ. of Texas at Austin
Applied Research Laboratory
P.O. Box 8029
Austin, Texas 78712

Director
Lamont-Doherty Geological Observatory
Torrey Cliff
Palisades, New York 10964

Director
Woods Hole Oceanographic Institution
Woods Hole, Massachusetts 02543

Director
Inst. of Ocean Science Engineering
Catholic University of America
Washington, D.C. 20017

National Science Foundation
Ocean Sciences Division
Washington, D. C. 20550

Office of Naval Research
Resident Representative
c/o Univ. of California, San Diego
Mail Code Q023
La Jolla, California 92093

University of California, San Diego
Marine Physical Laboratory
Branch Office
La Jolla, California 92093